UNIVERSIDADE
DE SANTIAGO
DE COMPOSTELA

CENTRO INTERNACIONAL DE ESTUDOS
DE DOUTORAMENTO E AVANZADOS
DA USC (CIEDUS)

Tese de Doutoramento

ANALYSIS OF ATMOSPHERIC PLANETARY BOUNDARY LAYER - TERRAIN INTERACTIONS.

WIND INDUSTRY IMPLICATIONS.

Miguel Ángel Prósper Fernández

ESCOLA DE DOUTORAMENTO INTERNACIONAL

PROGRAMA DE DOUTORAMENTO Enerxías Renovables e Sustentabilidade Enerxética

SANTIAGO DE COMPOSTELA

ANO 2018


USC
UNIVERSIDADE
DE SANTIAGO
DE COMPOSTELA

DECLARACIÓN DO AUTOR DA TESE

Analysis of Atmospheric Planetary Boundary Layer - Terrain Interactions. Wind Industry Implications.

D. Miguel Ángel Prósper Fernández

Presento a miña tese, seguindo o procedemento axeitado ao Regulamento, e declaro que:

1) A tese abarca os resultados da elaboración do meu traballo.
2) De selo caso, na tese faise referencia ás colaboracións que tivo este traballo.
3) A tese é a versión definitiva presentada para a súa defensa e coincide coa versión enviada en formato electrónico.
4) Confirmo que a tese non incorre en ningún tipo de plaxio doutros autores nin de traballos presentados por min para a obtención doutros títulos.

En Santiago de Compostela, a de de 20..

Asdo Miguel Ángel
Prósper Fernández


USC
UNIVERSIDADE
DE SANTIAGO
DE COMPOSTELA

AUTORIZACIÓN DO DIRECTOR / TITOR DA TESE

Analysis of Atmospheric Planetary Boundary Layer - Terrain Interactions. Wind Industry Implications.

D. Gonzalo Miguez-Macho

INFORMA:

Que a presente tese, correspóndese co traballo realizado por D. Miguel Ángel Prósper Fernández baixo a miña dirección, e autorizo a súa presentación, considerando que reúne os requisitos esixidos no Regulamento de Estudos de Doutoramento da USC, e que como director desta non incorre nas causas de abstención establecidas na Lei 40/2015.

En Santiago de Compostela, a de de 20..

Asdo Gonzalo
Miguez-Macho


USC
UNIVERSIDADE
DE SANTIAGO
DE COMPOSTELA

A la estanquera de Rúa Nova


USC
UNIVERSIDADE
DE SANTIAGO
DE COMPOSTELA

Contents

Acknowledgments

Comenzar a escribir esto es muy fácil, solo tengo que pensar cuál ha sido mi apoyo más importante durante estos años. Por ello, en primer lugar me gustaría dedicar esta tesis doctoral a mi familia, empezando por mi madre, porque gracias a ella estoy escribiendo estas palabras. A mi hermano con quien he tenido la suerte de convivir estos años de tesis. A mi abuela, a mis tíos y primos, porque entre todos formamos un maravilloso núcleo. También a mi abuelo, constante ejemplo a seguir en mi día a día, estoy seguro de que disfrutaría bastante con esto.

Continuar ya no lo es tanto, no me gusta simplificar en unas pocas palabras el agradecimiento a nivel profesional y personal que tengo a la gente que me rodea porque me quedo muy corto con respecto a lo que pienso. De todas formas también lo considero necesario dadas las circunstancias. Dicho esto, me gustaría dedicarle este trabajo a mi director de tesis, Gonzalo Miguez, que me ha dado está valiosa oportunidad que tanto le agradezco. Siempre me ha demostrado muy buenos valores en su papel de jefe, además ha sido un lujo poder contar con la opinión de un experto cuando es necesaria.

Quiero también dar las gracias la gente del GFNL con la que he compartido tantas cosas estos años. Por literal cercanía, empezar por Carlos, que comenzó siendo mi profesor, continuó como compañero y ahora tengo la suerte de considerarlo un amigo. A Sabela, que aparte de ser de mis mejores amigas, ha sido también un lujo de compañera con la que he disfrutado durante todo este tiempo. A Dani otra persona brillante con la que he convivido día a día, su talento en el trabajo solo es superado por el enorme compañerismo que demuestra a diario. A Damián, otro gran amigo que me llevo del grupo con el que he pasado muy buenos momentos dentro y fuera del despacho, da gusto ver a alguien disfrutar tanto con lo que hace. Al Alférez de fragata/Director/Doctor Eiras, menudo personaje, sobran las palabras. Al resto de la gente del grupo más allá del 029, Dario, Mariamo, Irma, Alberto, David y también a los nuevos fichajes Sara y Martín, les deseo lo mejor. Por supuesto, al resto de profesores del grupo, Vicente y Alberto. También a Breo y a Swen con los que he compartido despacho y a los que, a pesar de ya no están por la facultad, les guardo un aprecio especial. Me siento muy afortunado de toda la experiencia vivida en este grupo, he aprendido y madurado mucho aquí, y me llevo unos cuantos buenos amigos, no puedo pedir más.

También hay varias personas con las que he colaborado fuera del GFNL que se merecen mi más sincero agradecimiento. Empezando por Felipe, un gran profesional que confió en lo que hacíamos aquí desde mi primera etapa en el grupo y con el que he tenido la suerte de colaborar en varias ocasiones. A Nacho y a Fran, contactos del mundo empresarial que también respetaron y apostaron por nuestro trabajo de investigación, muchas gracias por vuestro voto de confianza. A Ian, que disfruta tanto como yo con lo que hacemos y con el que también he colaborado. A Platón y a George, de la Universidad de Atenas, me siento orgulloso y satisfecho del trabajo hecho juntos. Tengo que darle también muchas gracias al Meteorological Model Team de Goldwind y muy especialmente a Liu Zhao y Xu Dong, por la colaboración en este último año y por la experiencia única que he vivido gracias a ellos.

Cuando me enfrento a la difícil tarea de escribir estos agradecimientos no puedo dejar de pensar ni un segundo en otras personas con las que, más allá del ámbito familiar y laboral, he compartido tanto y me lo he pasado tan bien durante todos estos años. Estos son principalmente: Maki, Nacho, Dan, Sabela (otra vez), Higinio, Kiko, Xabi, Laura y algún que otro figura que anda por ahí, con cada uno de ellos comparto historias para escribir capítulos enteros. Da puro gusto ver como vamos evolucionando juntos, estoy muy contento de que estéis ahí.

List of Figures


USC
UNIVERSIDADE
DE SANTIAGO
DE COMPOSTELA

List of Tables

Summary

The development of wind energy has a direct effect on the reduction of carbon dioxide emissions from the energy sector. This industry is one of the largest anthropogenic contributors to the global problem of climate change. For this reason, and because it is the most expanded renewable energy source in the world, there is a clear need to optimize wind energy exploitation. Numerical modeling is a tool that forms part of the present and future of this sector; because it is able to reproduce the effect of wind farms on the atmosphere and to obtain its short-term production prediction. Besides, meteorological models allow us to improve wind resource analysis methods for any region of the planet.

The present thesis aims to achieve a detailed quantification and understanding of the main interactions between atmospheric planet boundary layer and terrain, focusing on the behavior of wind flows at different scales. In addition, we intend to improve the tools, within numerical modeling, for the analysis of such mechanisms, contributing in this manner to the optimization of the use of wind as a resource.

The primary tool used in this thesis is the WRF (Weather Research and Forecasting) model. It is a meso and microscale numerical prediction system designed for both atmospheric research and operational forecasting. In most parts of the research, high-resolution simulations are performed with the WRF model. This provides accurate information of near-surface wind fields and turbulent processes in a wide range of atmospheric stability conditions and areas of the planet, both in flat and complex terrain.


USC
UNIVERSIDADE
DE SANTIAGO
DE COMPOSTELA

Resumo

O desenvolvemento da enerxía eólica ten un efecto directo na reducción das emisións de dióxido de carbono procedentes do sector enerxético. Dita industria é o maior contribuinte antropoxénico ó problema mundial do cambio climático. Por isto, e por ser a enerxía renovable máis expandida a nivel global, existe una clara necesidade de optimizar a explotación eólica. A modelización numérica é unha ferramenta que forma parte do presente e do futuro deste sector, porque é capaz de reproducir o efecto dos parques na atmosfera e de obtener a súa predicción de producción a corto prazo. Ademais disto, os modelos meteorolóxicos permítennos mellorar os métodos de análise do recurso eólico en calquera rexión do planeta.

A presente tese busca lograr unha detallada cuantificación e entendemento das principais interaccións entre a capa límite da atmosfera e o terreo, centrándose no comportamento dos fluxos de vento a diferentes escalas. A maiores disto, preténdese mellorar os instrumentos, dentro da modelización numérica, encargados de analizar ditos mecanismos. Desta forma, poderase contribuir á optimización do aproveitamento deste recurso eólico.

A principal ferramenta empregada nesta tese é o modelo WRF (Weather Reseach and Forecasting). Trátase dun sistema de predicción numérica a meso e microescala deseñado tanto para a investigación atmosférica como para predicción operativa. Na maioría das partes da investigación realizaranse simulacións a alta resolución con dito modelo. Deste modo obterase información precisa sobre campos de vento cercanos á superficie e procesos turbulentos nunha ampla gama de condicións de estabilidade atmosférica e zonas do planeta, tanto en rexións chairas como en terreo complexo.


USC
UNIVERSIDADE
DE SANTIAGO
DE COMPOSTELA

Resumen

El desarrollo de la energía eólica tiene un efecto directo en la reducción de las emisiones de dióxido de carbono procedentes del sector energético. Dicha industria es uno de los mayores contribuyentes antropogénicos al problema mundial del cambio climático. Por ello, y por ser la energía renovable más expandida a nivel global, existe una clara necesidad de optimizar la explotación eólica. La modelización numérica es una herramienta que forma parte del presente y del futuro de este sector, porque es capaz de reproducir el efecto de los parques eólicos en la atmósfera y de obtener su predicción de producción a corto plazo. Además de esto, los modelos meteorológicos nos permiten mejorar los métodos de análisis de recurso eólico cualquier región del planeta.

La presente tesis busca lograr una detallada cuantificación y entendimiento de las principales interacciones entre la capa límite de la atmósfera y la topografía, centrándose en el comportamiento de los flujos de viento a diferentes escalas. A mayores de esto, se pretende mejorar los instrumentos, dentro de la modelización numérica, encargados de analizar dichos mecanismos, contribuyendo de esta forma a la optimización del aprovechamiento del recurso eólico.

La principal herramienta empleada en esta tesis es el modelo WRF (Weather Reseach and Forecasting). Se trata de un sistema de predicción numérica a meso y microescala diseñado tanto para la investigación atmosférica como para predicción operativa. En la mayoría de las partes de la investigación se realizarán simulaciones a alta resolución con dicho modelo. De este modo se obtendrá información precisa sobre campos de viento cercanos a la superficie y procesos turbulentos en una amplia gama de condiciones de estabilidad atmosférica y zonas del planeta, tanto en regiones llanas como en terreno complejo.


USC
UNIVERSIDADE
DE SANTIAGO
DE COMPOSTELA

Chapter 1

Introduction

Wind energy is the currently most developed and reliable renewable resource in the world. It is one of the main tools that humanity possesses to confront the emerging energy crisis and climate change. Its worldwide growth is a reality and a necessity, a requirement demanding a continuous optimization in each step of the production process. An essential part of this work is based on studying the physical interactions between the lower part of the atmosphere and the terrain. A better knowledge of the wind fluxes in the planetary boundary layer will help to improve exploitation plans and the daily management within the wind energy sector, increasing the efficiency of this valuable power source.

Wind energy outline

Each kWh produced with wind energy, from the biggest wind turbine in the North Sea to a smallest one in a farming business, means one thing, 450 grams of C02 emissions saved compared with the same kWh from natural gas production or 856 grams if the kWh is produced by coal generation [1, 2]. The climate change that is currently affecting the world is probably one of the main challenges that humanity has had to face in all its history. The increase in carbon dioxide levels in the air has a direct effect on global temperature and sea level rise. According to the Intergovernmental Panel on Climate Change (IPCC) [3] and the United Nations Climate Change (UNFCCC) [4], if the temperature increase fulfills the predictions expected for the next 50 years, the effects on humans, the natural systems and the planet could be catastrophic. Many of the greenhouse effects that produce this temperature rise are due to non-renewable sources of energy production. That is the primary reason why wind energy needs to further expand; it is necessary to change the direction of the global energy production system to a more sustainable scenario for the planet.

The wind is nothing more than the set of air currents that, at different scales, are formed driven by air pressure differences in different regions. It has accompanied Earth since the atmosphere exists, and its exploitation is anything but a novelty in human history. Wind energy has been used since ancient times to move boats or make the blades of windmills spin either to grind cereals or to pump water. In the summer of 1887 Charles F. Brush, one of the founders of the American Electric Company, built the first wind turbine for electricity production. With a diameter of 17 meters and a power of 12 kW it served to feed the battery of a private laboratory, in his house basement, for 20 years [5]. With this breakthrough, he also made his mansion the first home in Cleveland to have electricity (`http://www.lafavre.us/brush/mansion`).

Despite Brush's ingenuity, it has taken almost a century from this milestone of electricity generation to see this natural resource playing an important role in the field of energy production.

It was during the first oil crisis, in the 1970s, and the movements against nuclear energy in Europe in the 80's, when interest arose in obtaining energy from virtually inexhaustible natural sources. Since then, a process of standardization of facilities and safety methods has resulted in continuous performance improvements in the wind energy generation sector. These improvements have happened alongside exponential growth in turbine power and the number of wind farms all over the world. The first large-scale wind energy installation was constructed in California, with over 16,000 machines, from 20 to 350 kW (a total of 1.7 GW), installed between 1981 and 1990 [6]. Despite this US achievement, it is in Europe where wind farm installations increased more through the 80s and the 90s, a growth induced by the higher cost of electricity and the large wind resources. After 1990 most market activity is established in Europe, bringing, during the next twenty years, wind energy to the forefront of the global energy market. Figure 1.1 reflects the magnitude of the expansion of this resource during the last decade and a half, showing the global power wind energy capacity installed from 2001 to 2017.

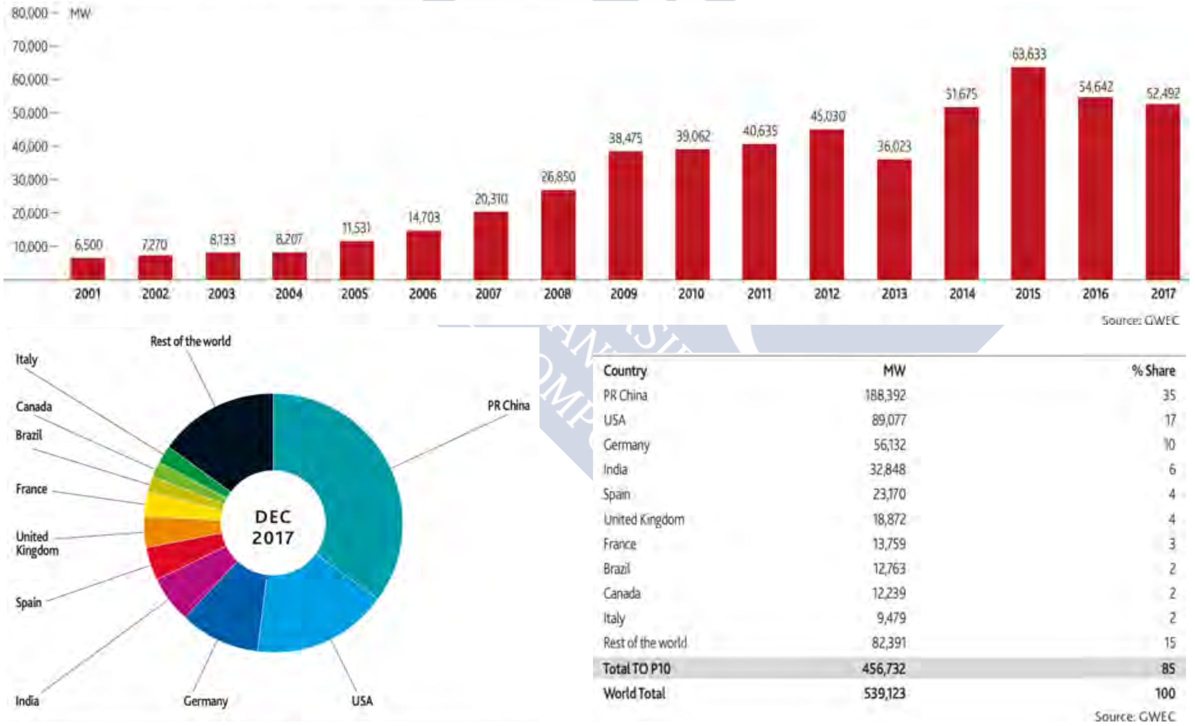

Country	MW	% Share
PR China	188,392	35
USA	89,077	17
Germany	56,132	10
India	32,848	6
Spain	23,170	4
United Kingdom	18,872	4
France	13,759	3
Brazil	12,763	2
Canada	12,239	2
Italy	9,479	2
Rest of the world	82,391	15
Total TO P10	**456,732**	**85**
World Total	**539,123**	**100**

Source: GWEC

Figure 1.1: (a) Global wind energy capacity installed from 2001 to 2017. (b) Top 10 cumulative wind capacity until December 2017. Source: Global Wind Energy Council

Currently, Europe maintains itself as one of the major players, alongside with China and the US (Figure 1.1b). This continent, with 168.7 GW of total wind power capacity installed by the end of 2017, has covered 10.4% of its electricity consumption needs with wind turbine energy [8, 9]. That same year, up to 55.2% of all the newly installed generators in Europe were of wind energy (Figure 2.2), demonstrating the clear commitment of the continent to this renewable source. In Spain, wind energy represents one of the primary power sources. Despite the halt in wind farm development since 2014, Spain is still the fifth country in terms of installed wind power, behind only China, USA, Germany, and India (Figure 1.1b). There are currently 23170 MW of installed wind power [8, 9, 10] in 1077 farms, which cover the electric demand of about 10 million homes [8, 10] The main wind farm clusters in the country are located in the north, in northern Galicia and Castile-Leon.

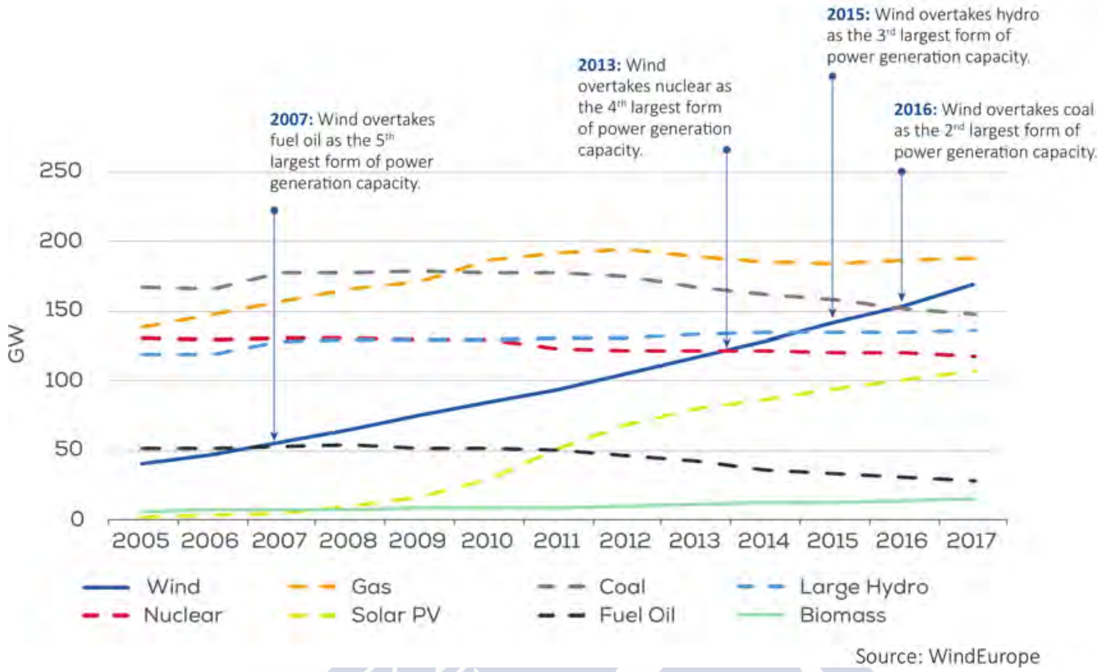

Source: WindEurope

Figure 1.2: Total power generation capacity in European Union 2005-2017. Source: WindEurope.

The market forecast predicts a continuation of this tendency for the coming years [11, 12], establishing wind energy as one of the main characters in the worldwide energy mix. Part of this success comes from offshore wind farms; this technology has been used to install 4.3 GW of new potential in 2017. Most of these farms (84%) are located in the waters off the coast of eleven European countries and the rest of them mainly in China and the US [11]. An exponential evolution in offshore production is expected in the next couple of years in Europe, when several installations, which are about to be completed, will be connected, leaving a total of 25 GW operational in 2020. Going a step forward in the prediction and taking into account the projections in Europe, US and Asia, the forecasts point at 120 GW of installed capacity by 2030 at sea, with 10 GW of installation rate per year achieved [13].

Apart from the big onshore and offshore installations commented before, there are other wind energy technologies currently exploited or in a mature process of development. One example of the former are the small and medium wind turbines (Figure 1.3a) used in a wide range of business and agricultural holdings [14]. These turbines, with proper installation and management, can provide a clean energy alternative and an economic benefit for many companies. Within the wind machines technology field, there are also new promising technologies, as the bladeless wind generators (Figure

1.3b), which use the resonant vibration of its vertical bladeless cylinder to generate electricity [15]. The design of these turbines makes them a desirable option, due to the low cost associated with installation and maintenance. Another new concept of wind energy is airborne wind turbines (`https://www.greentechmedia.com/articles/read/a-beginners-guide-to-the-airborne-wind-turbine-market#gs.DtWE1kQ`). These machines are able to produce electricity with the rotor supported in the air without a tower using big kites (`https://www.skysails.info/en/power/technology/`), benefiting from the stronger and steady flow of higher altitudes.

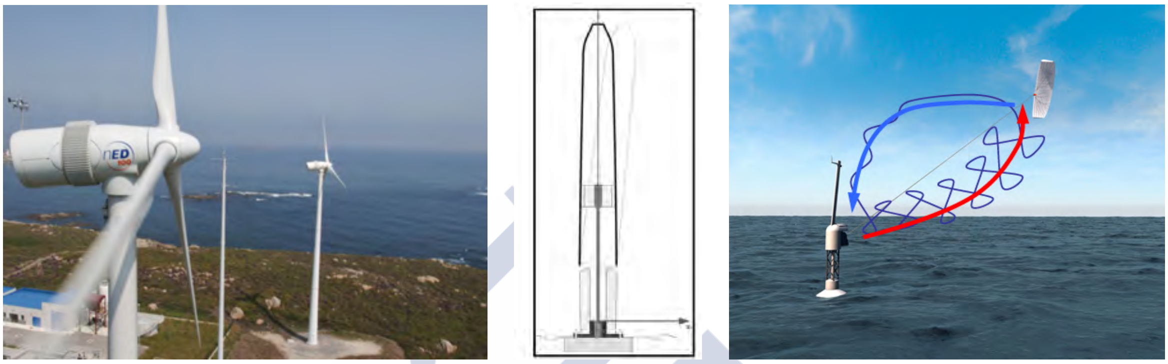

Figure 1.3: (a) Ned100 wind turbines (100 kW) [16] in Galician installation (Source: Norvento S.L.U.). (b) Vortex bladeless generator basic sketch (Source: Vortex Bladeless S.L.). (c) Kite airborne wind generator (Source: SkySails Power).

Wind energy - Numerical modeling

The current situation summarized above puts wind energy as one of the principal performers in the worldwide energy mix, and a good alternative to global warming. With this scenario, the improvement of the wind energy exploitation seems necessary, from new strategies in a future wind farm projection and optimization of wind farm designs to the better daily management of the installations. Taking into account that the single source of this energy is wind, it becomes clear that the study of the atmospheric boundary layer fluid dynamics goes hand in hand with every step of the wind energy exploitation. Specifically, it is essential to have a precise knowledge of air flow structure, understand its behavior in layers close to the surface, and to be able to deliver skillful local short-term forecasts to optimize wind farm construction and exploitation.

A good qualitative way to visualize the behavior of the wind is through its power spectrum [17]. The wind energy spectrum regarding the timescale of events (Figure 1.4) has maximum values representing different phenomena magnitudes [18]. This curve includes long-term events (climatic scale, blue line), medium term events (synoptic scale, red line) and short time events (microscale, green line). The wind industry interest covers a wide range of this spectrum, from climatic events, as for example, El Niño effect [19] over a high wind resource region, to microscale events such as a turbulent flow resulting from surface heating [20]. All these climatic and meteorological situations have a direct impact on the production and service life of wind turbines. Depending on the stage of a wind farm installation planning and lifetime, different parts of the events represented by the spectrum are more or less noteworthy.

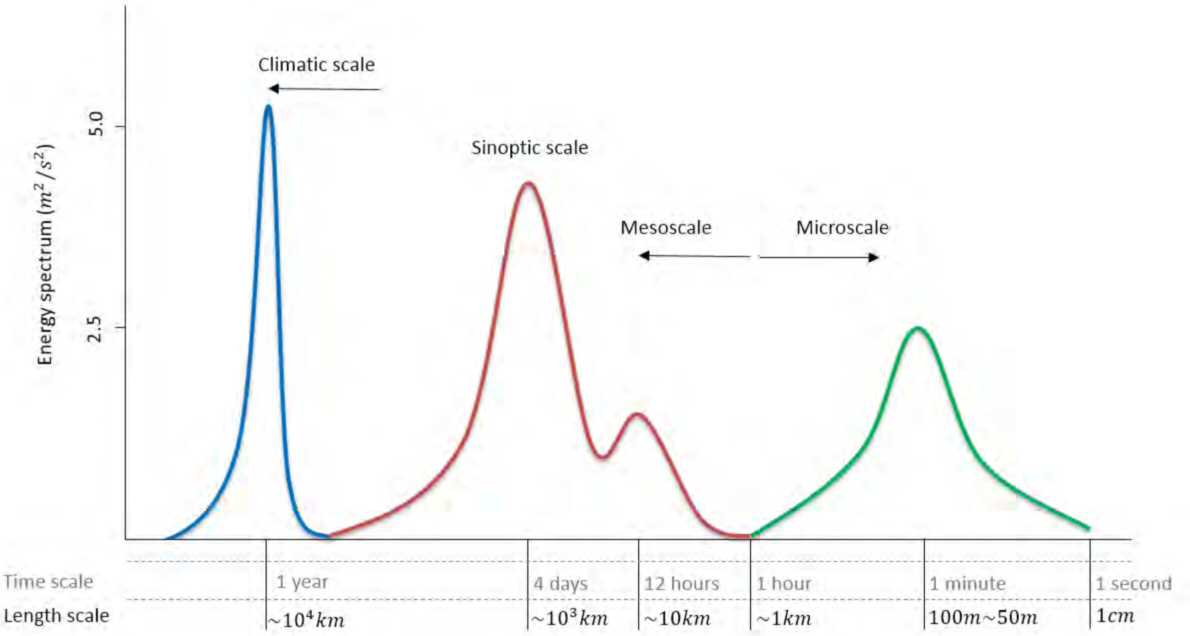

Figure 1.4: Energy spectrum of wind speed in the near-surface layer. The blue line corresponds to climatic scales, the red one to synoptic and mesoscales, and the green one to turbulent or microscale events.

Consequently, numerical modeling tools are directly related with the scale of the phenomena object of study. In the next paragraphs, we are going to follow the general phases of a wind farm siting and operation project (`https://www.awea.org/wind-101/siting-a-project`), from a meteorological perspective, pointing out the role that the numerical model plays in each of them.

The first logical step of the wind farm siting project, focusing on the atmospheric research field, is the search for areas with the proper resource within the region of interest. Currently, the study of wind resource all over the world with atmospheric numerical modeling (NWP) is very developed. It is not difficult to find high-quality wind resource databases from many parts of the planet. An example of this in the U.S. can be seen in the NREL Wind Prospector (`https://maps.nrel.gov/wind-prospector/`). This geospatial wind resource map at high resolution provides a composite of the best available data at the time from different long-term forecasts for all the country [21] (`https://www.nrel.gov/gis/wind.html`). Another recent similar tool is The Global Wind Atlas (GWA) (`https://globalwindatlas.info/`), which is a web-based application developed to help to find potential high-wind areas for wind power generation virtually anywhere in the world and perform preliminary calculations. GWA uses a WRF downscaling process beginning in large-scale wind climate data (70 km) and finishing in between meso and microscale wind climate data (1 km)(`https://globalwindatlas.info/about/method`)

The planning to install a new wind farm is regulated in every aspect by the legislation of the competent authority in the country [22]. In Spain, for example, many of these procedures are included in the Real Decreto 413/2014 of 6 June [23], and the autonomic normative of each community [24]. Focusing on the technical-meteorological aspects, when the location of the future installation is determined, and the legal permits are acquired, the wind company initiates a more accurate study of the region of interest. There is a previous observational data collection phase using meteorological stations with different heights designed explicitly for this purpose. However, it is more and more frequent for the installation companies to also use the capabilities of meteorological modeling. The exponential increase of computer power in HPC systems allows the development and faster use of these numerical tools. In this specific field, this means more runs with higher resolution and in a shorter time period. The results from these studies provide valuable information about local phenomenology in the analyzed area due to the good representation of the planetary boundary layer behavior from numerical modeling at high resolution. In the next figure, we can see a visual example of the capabilities of NWP within this field. It represents the annual mean wind speed field obtained from WRF model simulations in a densely exploited cluster region in Mexico (Chapter 5).

Figure 1.5 depicts the annual mean wind speed at hub height obtained from high-resolution daily simulations over the area of interest. The image shows a noticeable mean resource difference between the two meteorological stations. These two stations are around 20 km from each other over flat terrain several kilometers away from the mountains. However, MET1 register a mean value close to 10 m/s and MET2 only reaches 4 m/s. It is easy to imagine the possible incorrect assumptions that could be made in a wind farm siting project if we just take into account the data from MET1 or only from MET2. Numerical meteorological modeling provides us with valuable information about all the area of interest, not only a few points; this is highly profitable if we take into account the large size that a wind farm can have. The conjunction of quality observational data and a high-resolution forecast with NWP, both for the same representative period, is the best-combined tool that wind resource analysts can have at their disposal.

After the data collection analysis and the meteorological study of the area of interest, is when the wind farm can be definitively designed. Computational Fluid Dynamics (CFD) models are the current most extended tool for this purpose, due to their capacity for simulating accurate air flow fields, considering in detail the main microscale processes affecting the wind [25]. They can run over complex terrain using orography values from LiDAR data [26], and they also include specific turbine schemes to simulate wake effects on wind farm areas. In the design process, it is fundamental to take into account the wake that each turbine produces because it has a direct impact on the farm's production and also affects the lifetime of the rest of the machines.

When the wind farm is finally installed (Figure 1.6), the use of high-resolution meteorological modeling acquires more prominence. Local short-term forecasts can provide valuable information in an operational wind farm, as wind speed and direction predictions enable a better use of the resource. On the one hand, for electric grid operators, which distribute a vast amount of eolic energy that should be efficiently incorporated into the electrical grid for distribution, the prevention of ramp events effects [27] is fundamental. These extreme short-term situations produce important increases or drops in power production, which can have a major impact on the grid [28]. On the other hand, high-resolution meteorological modeling is able to provide an accurate wind energy production forecast for one and even two days ahead [29]. It can also protect the wind farm from extreme wind events which are potentially dangerous for the turbines and have a negative effect on productivity [30]. These reasons make

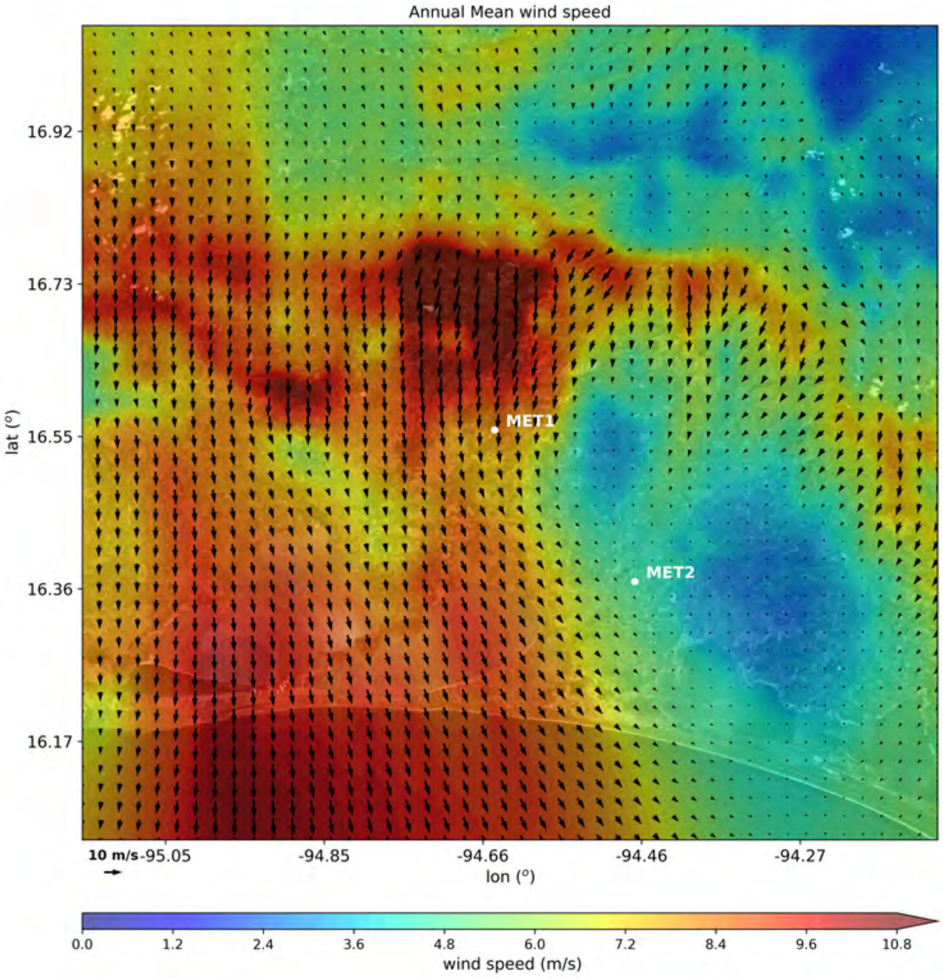

Figure 1.5: Annual mean wind speed (70 meters height) from WRF 1 km resolution simulations in a wind area in Mexico (Chapter 5). The observational data used is obtained from the meteorological stations plotted in white.

local short-term forecasting of great utility in the daily management of the installation.

Numerical weather models can also be part of different applications in the very near future forecasting (nowcasting). Going a step forward, the combination of NWP and MOS (Model Output Statistics) is an effective technique for very short-term wind predictions [31]. MOS models are capable of minimizing NWP errors induced by sub-grid phenomena and local effects in a short time horizon. In this way, we can, for example, predict the optimal yaw orientation of the turbines a few hours ahead, obtaining higher performance and lower stress.

Figure 1.6: Operative wind farm in a complex terrain area over Serra do Xistral, Galicia (Spain).

WRF model - Wind energy applications

In this thesis we deal with many of the issues described above, using the WRF model as a primary tool. This software is a mesoscale and microscale numerical prediction system designed for both atmospheric research and operational forecasting needs. This regional model uses global model inputs to define its boundary and initial conditions. It has been developed by the National Center for Atmospheric Research's (NCAR), the National Oceanic and Atmospheric Administration's (NOAA) and the National Centers for Environmental Prediction (NCEP) in collaboration with other state agencies and universities [32].

In general terms, WRF code V3 includes: WRF Software Framework (WSF), Advanced Research WRF (ARW) dynamic solver, the WRF Preprocessing System (WPS), WRF Data Assimilation (WRF-DA), numerous physics packages contributed by WRF partners and the research community and several graphics programs and conversion programs for other graphics tools [33]. The ARW solver is the key component of the modeling system, which has an equation set fully compressible, Eulerian and non-hydrostatic with a run-time hydrostatic option.

This NWP model uses terrain-following, hydrostatic-pressure vertical coordinates with the top of the model being a constant pressure surface. The time integration scheme in the model uses the third-order Runge-Kutta scheme, and the spatial discretization employs 2nd to 6th order schemes. The model supports both idealized and real-data applications with various lateral boundary condition options. The model also supports one-way, two-way and moving nest options. It can run on single-processor or shared- and distributed-memory computers (`http://www2.mmm.ucar.edu/wrf/users/model.html`).

The WRF model includes parameterizations for atmospheric processes that occur at scales unresolved by the model grid spacing. These schemes can be divided into five main groups:

1. Microphysics: Resolve the formation of meteors: steam, clouds, rain, ice, etc.
2. Cumulus convection: Resolve vertical moisture flows at scales smaller than those of the domain. Formation of cumulus and rains.
3. Planetary Boundary Layer: Solves the flows due to turbulence in the whole column of the atmospheric boundary layer.

4. Surface: Calculate the humidity and heat flow at the surface level. It takes into account: the humidity of the soil, vegetation, accumulated snow, urban areas, etc.
5. Radiation: Thermal flows derived from the radiation of the Sun. Shortwave and long wave.

To achieve high resolution with this model, it is necessary to use a nested configuration approach where successive child grids with increasing resolution are set within coarser parent domains. The corresponding parent provides boundary conditions for the nested grid along the simulation time. With this procedure, it is possible to perform high-resolution simulations starting from coarse global simulation data. In Figure 1.7 we show an example of a nesting domain configuration for the simulations performed in the study presented in Chapter 5. This capability is precious in wind energy applications because it allows us to reach the precision desired in any part of the world using global model data (many of them publicly available) and a nesting domain configuration

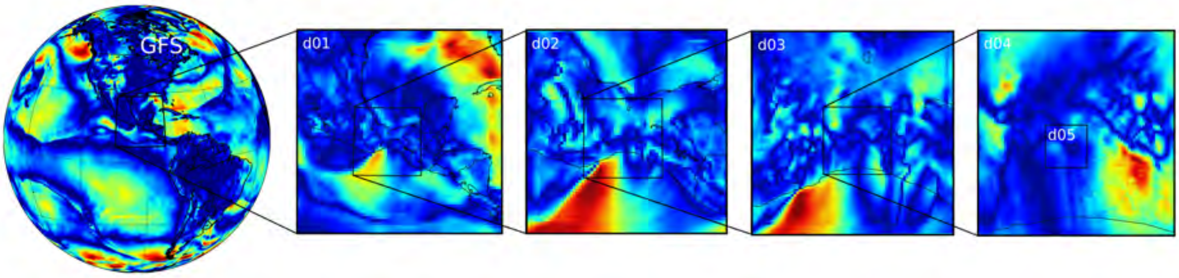

Figure 1.7: Wind field representations over domain nesting configuration for an area studied in Mexico (Chapter 5).

The following figure shows a flowchart of the general WRF simulation process used in the studies presented in this thesis.

The first step in a WRF simulation is the WRF Preprocessing System (WPS) (Figure 1.8, blue part), which consists of three programs that provide the input data to the WRF real program to run the simulation. *Geogrid* defines the simulation domains and interpolates various terrestrial data sets to the model grids. Ungrib unpacks GRIB (GRIB1 and GRIB2) meteorological data (e.g. GFS, ERA5, ERA-Interim...) and packs it into an intermediate file format. Finally, *metgrid* horizontally interpolates the meteorological data onto your model domain, creating an output which is used as input to WRF.

With the WPS complete, the next step is the *real.exe*, which creates initial and boundary condition files for real-data cases. After this, the data are ready to start the WRF running with *wrf.exe*. This is the main component; it performs the time integration controlled by the run-time selected *namelist* options. WRF outputs are formed by non-post-processed variables (e.g., T variation per level, decomposed wind components. . .), so they need to be post-processed (Figure 1.8, orange part) to extract the information of interest, such as a wind field at hub height, or a wind speed series at a specific point.

As commented above, the WRF model has many physical packages that can be used to resolve many different phenomena, such as those of atmospheric chemistry (WRF-Chem) or fire-related processes (WRF-Fire). In our case, we want to focus on the wind energy

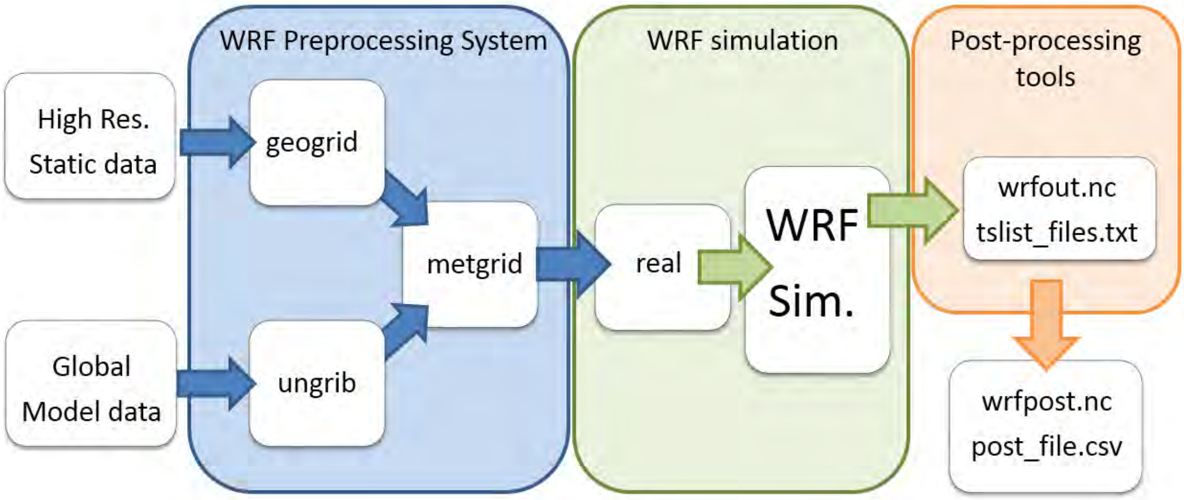

Figure 1.8: General WRF simulation process flowchart followed in the studies presented

field. We are interested in the planetary boundary layer- terrain interactions. That is why we need high-resolution horizontal and vertical simulations; we want to resolve the wind and temperature variations in the boundary layer accurately. Moreover, the WRF model also includes a wind farm parameterization [34] able to simulate the wake effects of a turbine on the close environment and to calculate its production according to a power curve, standard coefficients, and dimensions. This parameterization represents wind turbines as momentum sinks, transferring kinetic energy into turbulent kinetic energy and electricity [35].

The quality of the results obtained from high-resolution WRF simulations depends to a large extent on the representation that the model makes of large-scale eddies within the planetary boundary layer (PBL) and of how it treats subgrid-scale processes (SGS) [36]. By multiple nesting, as in Figure 1.7, it is possible to solve phenomenology on a turbulent scale and include the mesoscale effect in the domain of higher resolution. To be able to put this concept into practice, in many cases, it is necessary to reach very high levels of resolution ($\leq$100m) by LES (Large Eddy Simulations). LES is an approach to directly solve the equations of motion within the atmospheric boundary layer by filtering the Navier-Stokes equations and directly solving the large turbulent eddies [37]. This type of simulation can be an accurate tool providing information about turbulent processes in a wide range of atmospheric stability situations, both in flat regions as well as complex terrain.

Motivation and thesis outline

In this thesis we aim to achieve a detailed quantification and understanding of the main interactions between the atmospheric planet boundary layer and terrain, focusing on the behavior of wind flows at different scales. In this way we intend to improve the tools, within numerical modeling, for the analysis of such mechanisms, contributing to the optimization of the use of the wind resource. For this purpose, we use the WRF (Weather Research and Forecasting) model as a primary tool. In most parts of the investigation, we configure it with high-resolution, reaching even the microscale through LES (Large Eddy Simulations). In this manner, we intend to provide accurate information of wind fields and different turbulent processes in a wide range of atmospheric stability conditions and areas of the planet, both in flat and complex terrain.

In the first part of the manuscript, composed of the first two chapters, we present a broad study about wind resource forecasting for an onshore wind farm. The first chapter focuses on the case of wind production forecast and validation for a real onshore wind farm using high horizontal and vertical resolution WRF model simulations. The wind farm is located in Galicia, in the northwest of Spain, in a complex terrain region with high wind resource. Utilizing the Fitch scheme, specific for wind farms, a period of one year is simulated with a daily operational forecasting set-up. In the second chapter, we go a step forward in the short term forecasting issue combining the WRF prediction from the first study with a post-process statistical tool (Kalman Bayesian filter). With this technique, we reach the nowcasting temporal scale, with critical applications in the wind industry.

The second part, presented in chapter three, is centered on the wake effect of the wind farms on their environment. We introduce the Annual Wake concept, which is the mean annual wind resource loss in the area due to the wind farm's wake. We test this tool over the same wind farm from the first part and another one in China.

The third part approaches the extreme wind study issue. Specifically, it is focused on investigating different mountain wave phenomena resulting from complex interaction between large-scale meteorological conditions and local orographic forcings in a wind farm cluster in Mexico. Finally, in the fourth and last part, in chapter five, we analyze the microscale turbulent phenomenology in a wind farm area in southern China using WRF-LES simulations.


USC
UNIVERSIDADE
DE SANTIAGO
DE COMPOSTELA

Chapter 2

Wind resource forecasting

Introduction

There is a clear need to improve the exploitation of wind resource, given that the amount of eolic energy produced is rapidly increasing and it should be efficiently incorporated into the electrical grid for distribution. For this purpose, it is essential to have a clear knowledge of air flow structure, understanding its behavior in layers close to the surface, and to be able to deliver skillful local short-term forecasts in order to optimize wind farm construction and exploitation. Short-term wind power forecasting presents many challenges. In most cases, onshore farms are affected by microscale events that are especially complicated to predict because they have a turbulent phenomenology, with continuous wind direction and wind intensity changes in short periods of time. In recent years, due to the global push in wind power and the exponential increase in computing capacity, there has been an important development in short-term wind and wind power forecasting methods.

The current state of the art of numerical modeling allows for improved wind farm characterization methods and for a more accurate and reliable study of their interaction with the atmosphere. Current methods of Computational Fluid Dynamics (CFD) are capable of simulating accurate air flow fields, considering in detail the main microscale processes affecting the wind, like buoyancy or turbulence diffusion effects [25]. They can run over complex terrain using orography height values from LiDAR data [26]. However, these models do not readily incorporate time-varying lateral boundary data from observations or analysis and, furthermore, thermal effects on turbulence and the wind flow are generally considered constant and hence, are not realistic, as those can vary substantially throughout the day. The current state of the art of meteorological numerical modeling allows for improved wind farm characterization methods and for a more accurate and reliable study of their interaction with the atmosphere. Mesoscale models such as WRF (Weather Research and Forecasting)[32] are able to perform simulations with a horizontal resolution of less than one hundred meters, Large Eddy Simulations (LES)[38] aiming at predicting and characterizing turbulent phenomena that affect wind farms and have direct impacts on energy production. In addition, wind farm output is also strongly affected by wake effects from the turbines themselves. There are several current studies with WRF LES simulating wind turbine wakes with high accuracy [39, 40, 41]. Notwithstanding, LES simulations still represent an excessive computational burden, and are not yet a viable tool for short term wind power operational forecasting. In studies combining statistical and numerical models, generally lower resolution simulations are used, such as Zhao et al. [42] with 3 km or Li et al. [43] with 6 km of horizontal resolution in the inner most domain. Che et al. [44] and Che and Xiao [45] developed a wind forecast system employing 0.5 km resolution WRF simulations with a Kalman filter. In regards to specific tools for numerical model predictions, WRF versions 3.3 or later include a wind farm parameterization [46] (WRF-WF hereafter) able to simulate the wake effects of a turbine on the close environment and to calculate its production according to a power curve, standard coefficients and dimensions.

It is nevertheless difficult to find studies using WRF specifically for wind farms and directly comparing results with observations. Due to the lack of data, many investigations in this field examine the hypothetical impact of different farm configurations at several scales. For example AC Fitch [34, 35] and Vanderwende and Lundquist [47] study the theoretical impact of wind farms in regions of the U.S. Midwest on the close surroundings. For larger scales, the wake parameterization has been used in studies of the broader impact of wind farms on the global climate [48, 49, 50]. There are many studies focused on wake effect understanding using WRF-WF, as Santoni et al. [51], which couple a WRF simulation with WRF-WF and a WRF-LES in an installation in Texas. In this same U.S. state, Xia et al. [52] use WRF-WF in a one-month period simulation to analyze the effect of a large turbine cluster on the nearby near surface temperature. Kumar et al. [53] use the Fitch scheme to predict wind profiles and turbulent intensity in two wind farm locations in India and Scotland. There are several publications using WRF for the offshore farm of Horns Rev in Denmark. Jiménez PA et al. [54, 55] perform high-resolution simulations (333 m) to estimate the total farm power deficit due to the wake effects of the turbines. O Eriksson et al. have contrasted the wake parameterization with LES simulations using an actuator disk method in Rev Horns [56] and another farm in Sweden [57]. Another wake effect parameterization, explicit wake effect parametrization (EWP) designed by Volker P et al. has been compared to WRF-WF on this same farm [58]. More recently, in 2018, S. C. Pryor et al. have also assessed the differences between WRF-WF and EWP for several purposes [59, 60], with short-term simulations in the U.S. Central Plains area.

Our main goal in this work is to use WRF at high resolution as a wind power forecasting tool for an actual on-shore farm, the Coruxeiras wind farm, for a whole year. We test the effectiveness of WRF in calculating the energy production of this farm in complex terrain, in real time. The availability of high quality in situ real data (at the nacelle of each turbine in the farm) allows us to perform an in detail validation of the simulations, in terms of power prediction and of the impact of the wakes from the turbines. In addition, we compare high-resolution with low-resolution simulations for different temporal scales to assess the potential of the method and the high resolution configuration. To the best of our knowledge, this is the first time that a thorough evaluation for such a long period of time and such detail has been performed. The article is organized as follows: In section II the methodology is explained in detail, in section III, the main results obtained are shown and finally in section IV the conclusions reached are discussed.

Methodology

Wind farm characteristics

Coruxeiras wind farm is located in Serra do Xistral mountains in Galicia, in northwest Spain (Figure 2.1a). The climate in the region is temperate maritime. Galicia lies within the main North Atlantic storm track most of the year and winds are predominantly from the west-southwest. In summer, when the subtropical Azores high moves poleward, the region is only marginally affected by baroclinic storms within the westerlies, and northeasterly winds dominate. Because of the position of Serra do Xistral at the very northwest corner of the land mass of the Iberian Peninsula, the predominant southwest/northeast flows are accelerated and there is a very high potential for wind energy. Numerous wind farms exist in the area, which is one of the most productive in Europe [61, 62].

Norvento company is the developer and current operator of Coruxerias wind farm, installed in 2006. It is composed of 31 turbines ECOTECNIA74 [63] with 1.670 MW of nominal power (Figure 2.2). The hub height is 60 m and the rotor diameter is 74 m. They are located along a mountain crest of around 800 m elevation above sea level, one of the tallest in the area, and separated by a mean distance of 300 m. The orography in the farm's surroundings is rather complex, with elevations reaching almost 1000 m descending rapidly to sea level in deep river valleys leading to the coast, which is in close proximity (Figure 2.1b and 2.1c).

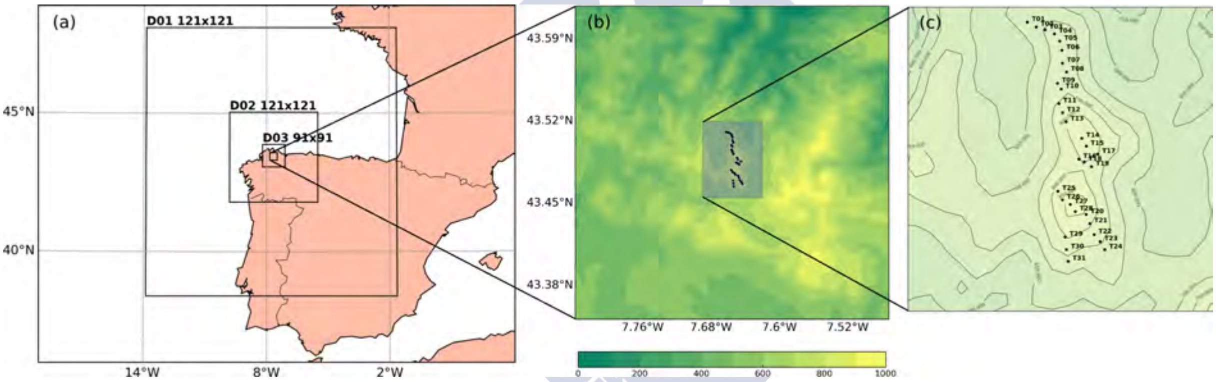

Figure 2.1: (a) WRF nested grid configuration, with the number of points for each domain indicated. (b) D04 is expanded showing topography. Coruxeiras wind farm is located in the central area of D04, on top of a hill (c).

WRF configuration

We use the Advanced Research WRF (ARW) model version 3.6 [32] (WRFV3.6) to perform the simulations. Based on a fully compressible and non-hydrostatic dynamic core [33], WRFV3.6 is a limited-area mesoscale model, with a terrain-following hydrostatic-pressure vertical coordinate, designed for operational forecasting, as well as research.

The domain's configuration meets the requirements recommended by Warner [64], including a parent (D01) and three nested grids (D02, D03 and D04) (Figure 2.1a) one-way interacting. D01 is centered at 43.29 N and 7.75 W (Figure 2.1c) with 121x121 grid points of 9 km of horizontal resolution. The horizontal resolutions of D02, D03 and D04 are 3 km

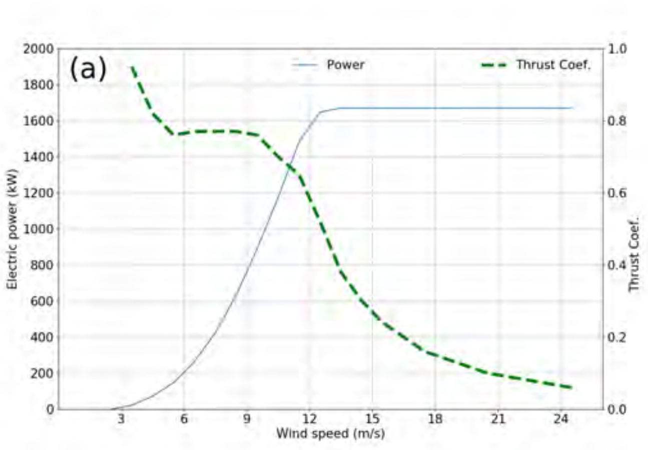

IEC-1400-1 category	II - A
Nominal power	1670 kW
Blades	3 blades at windward
Speed range	3 m/s - 25 m/s
Power control system	Variable speed with one pitch per blade
Rotor diameter / height	74 m / 60 m
Rotor power density	2.57 m2/kW

Figure 2.2: (a) ECOTECNIA 74 wind power curve (density=1.112kg/m3, height=975m, temperature=9C). The blue line represents power and the green, thrust coefficient. (b) Summary table with the main wind turbine characteristics.

(121x121 grid points), 1 km (91x91 grid points) and 333 m (91x91 grid points) respectively. The highest resolution domain has a size of 30.3 x 30.3 km, which allows for an adequate simulation of the local meteorological effects occurring around the wind farm. The 333 m resolution of this inner-most domain is used in similar studies, as Jiménez PA et al. [55] or Eriksson et al. [57] and it is very close to the average distance between wind turbines (around 300m). Thus, practically each wind turbine in the simulations is represented by a different grid point, (31 turbines=28 grid points). Land use information for D04 is obtained from the Corine (Coordination of Information on the Environment) database [65] with a resolution of 250 m, and terrain elevation from the ASTER Global Digital Elevation Map (GDEM) from USGS (United States Geological Survey) [66] with a resolution of 30 m. In the other domains, terrain and land use data are from the WRF global standard data base, both at 30" resolution. The outer three domains have 34 vertical level grids, whereas the D04 inner-most grid has 67 vertical levels, 7 of which lie within the first 200 m above ground, at about 14, 41, 70, 99, 127, 156 and 184 m height. In this way, it is possible to achieve a more accurate simulation of wind and temperature variations in the surface layer. A low height first level, 14 m in this case, is also important because it improves the calculation of land surface fluxes [67].

With regard to physics options, the simulations utilize the rapid radiative transfer model longwave [68] and Dudhia shortwave radiation schemes [69]. Microphysical processes are resolved with the WRF model single-moment six-class scheme [70] and land-surface fluxes with the unified Noah model [71]. The Mellor–Yamada level 2.5 (MYNN 2.5) model [72] is used for the planetary boundary-layer (PBL) turbulence. Convection is parameterized in the first domain only, with the Kain-Fritsch scheme [73].

In order to obtain wind power production and to estimate the effects of wind turbines, the Fitch scheme is used (WF-S hereafter). WF-S represents wind turbines as momentum sinks, transferring kinetic energy into turbulent kinetic energy and electricity [34]. The MYNN 2.5 level scheme calculates the mixing resulting from the vertical wind shear induced by the momentum sink. MYNN also takes into account the effects of buoyancy and the effects of stability on the turbulent length scale. The initial 6 h of each run are excluded from the forecast data series used in the analysis of the results, thus, only outputs after this spin-up time are considered [33].

Experiments

To analyse the effects and behaviour of WF-S, two types of experiments are performed and results compared, one obtaining a daily wind power forecast using WF-S (WF) and another with the WF-S disabled (PO). In the latter case, wind power production of each wind turbine is calculated from forecasted wind speed at hub height through a polynomial adjustment to the manufacturer‘s wind power curve (Figure 2.2a). The period chosen for study is one full year (2015/02/01–2016/02/01), broken into 365 daily simulations. For each daily simulation, in both configurations the model is run for 54 hours (6 h spin up + 24 h + 24 h). The results of the highest resolution grid (D04) are extracted for the first 24 hours for both experiments (WF-HI-1D and PO-HI-1D) and a primary analysis is performed. The results of the second 24 hours are separately analyzed and compared, (WF-HI-2D and PO-HI-2D), aiming at assessing the skill of these simulations in forecasting wind speed and wind power with a longer lead time. More extended forecasts are of great interest for the design of an operational forecast system, given the temporal constraints to which the energy producer is bound when providing wind power forecasts to the electric system operator. In order to evaluate the impact of horizontal resolution, results from the D03 domain (1 km horizontal resolution), for both experiments and for the two lead times considered for the high resolution grid, (WF-LO-1D, WF-LO-2D, PO-LO-1D and PO-LO-2D) are also extracted for analysis. Thus, two general cases with and without wake parameterization, and four variants within each case are tested. Table 2.1 summarizes the considered configurations.

Initial and boundary conditions

One year (2015/02/01–2016/02/01) GFS forecast data from the National Centers for Environmental Prediction (NCEP) are used as initial and boundary conditions for the WRF model, with a 3-h update interval. The horizontal resolution of this dataset for all variables is 0.25 x 0.25 deg, with 32 levels ranging from 1000 to 10 hPa. As mentioned above, for each day of the chosen period, 54 hour long simulations are performed, starting at 18:00 UTC the previous day from GFS forecast data with 18h lead time. Using GFS forecast data from the previous day run the forecast tool is placed in a real-world scenario. This database is publicly available, even for commercial purposes, promptly after generation, which is a major advantage in terms of financial cost and efficiency of the forecasting procedure in a real life situation (https://rda.ucar.edu/datasets/ds084.1/#!description). We note that WF-HI-1D initial and boundary conditions come from PO-LO-1D and not from WF-LO-1D, which would have provided perturbed initial and boundary conditions because of the activated WF-S in WF-LO-1D. In this manner WF-HI-1D and PO-HI-1D are directly comparable, one with WF-S activated and the other with it deactivated.

	Name	Wind Farm Param.	Resolution	Simulation Hours (+6)
CASE 1.1	**WF-HI-1D**	**Fitch**	**333 m**	**24 h**
CASE 1.2	WF-HI-2D	Fitch	333 m	48 h
CASE 1.3	WF-LO-1D	Fitch	1 km	24 h
CASE 1.4	**WF-LO-2D**	**Fitch**	**1 km**	**48 h**
CASE 2.1	PO-HI-1D	No Param	333 m	24 h
CASE 2.2	PO-HI-2D	No Param	333 m	48 h
CASE 2.3	PO-LO-1D	No Param	1 km	24 h
CASE 2.4	PO-LO-2D	No Param	1 km	48 h

Table 2.1: Two main configurations, CASE 1 and 2 (with and without wake parameterization), with their variants. The identifier names represent the case characteristics, for example, WF-HI-1D: **WF** (Wind farm parameterization), **HI** (high resolution, 333 m) and **1D** (24 hour lead time) or PO-LO-2D: **PO** (polynomial adjust), **LO** (low resolution, 1 km) and **2D** (24 hour lead time).

Observations and error measures

The observational data used in this work is provided by Norvento S.L.U. (`https://www.norvento.com/`), collected from anemometers located on top of each nacelle. One year mean hourly wind data for each turbine is available, computed, in turn, from ten minute averaged data. Nacelle wind observations are more representative of conditions at the turbine than measurements obtained from a weather tower a distance away [45]. We perform quality control on the raw observational data before using it for validation, filtering out discontinuities such as automatic starts after stops or a preventive maintenance.

Different errors measures are calculated to evaluate the forecasting skills of the simulated data. With regard to the wind speed forecast, one of the most frequently used errors in this study is the mean absolute error (MAE). MAE (Equation 1) is a useful tool in forecasting because it is a simple calculation providing clear information about deviations from the observed value. The mean error (Equation 2) is also computed. It gives an idea about the overall sub or overestimation of the forecast. This is an important issue in this field because of the sensitivity of wind power production to slight differences in the wind intercepted by the turbine. With respect to wind energy production, the normalized mean absolute error (NMAE) (Equation 3) and NME (Equation 4) are used. These are similar errors as wind speed MAE and ME, respectively, but for power output and on a percentage scale where, 100 per cent would represent the wind power maximum production.

$$MAE = \frac{1}{n}\sum_{i=1}^{n}|f_i - ob_i| \tag{2.1}$$

$$ME = \frac{1}{n}\sum_{i=1}^{n}(f_i - ob_i) \tag{2.2}$$

$$NMAE = \frac{\frac{1}{n}\sum_{i=1}^{n}|f_i - ob_i|}{NP} \tag{2.3}$$

$$NME = \frac{\frac{1}{n}\sum_{i=1}^{n}(f_i - ob_i)}{NP} \tag{2.4}$$

In these equations, i represents point in time, n is the total number of such points, and f and ob are the predicted and observed values, respectively. For MAE and ME, f and ob are wind speeds, while for NMAE and NME they are power output, which the model calculates making use of the production curves for each turbine. NP in these cases stands for nominal power.

Results and discussion

As explained in the previous section, there are two main model configurations used to simulate a long period of time, broken down in 54 hours long forecasts. These experiments result in a large amount of data, which we use to verify and evaluate the capacity of the forecasting tool under diverse conditions. For this purpose, this section is divided in three parts. In 3.1 the main general results obtained from the different experiments are discussed. Subsection 3.2 is focused on the dependence of results on wind direction, in particular wake representation. Finally, in 3.3, the mean overall wind farm impact on the close surroundings is estimated.

General results

Several error measures are displayed in this section at different temporal scales in order to provide a general view of the forecasting skill of the different experiments. First, annual mean results are shown in Figure 2.3 in terms of (a,b) wind speed MAE and (c,d) wind power NMAE for each turbine and experiment. These are grouped into high (a, c) and low-resolution simulations (b, d), and each panel shows separate curves for first and second day forecasts, with and without wake parameterization.

For the shorter lead-time range experiments WF-HI-1D and PO-H1-1D, practically all turbines have values below 2.00 m/s for wind speed MAE and 16% for wind power NMAE. There are no significant differences in error behaviour among turbines. Mean total wind farm NMAE and MAE show very close values for both cases, with subtle lower biases for the experiment without wake parameterization PO-HI-1D (14.37 % and 1.86 m/s) than for the simulation with it, WF-HI-1D (14.75% and 1.87 m/s). For second day forecast, results are very similar in terms of the spatial distribution of errors, but values are higher than for the first 24h, with NMAE and MAEs of 16.36% and 2.13 m/s for WF-HI-2D and 15.93 % and 2.09 m/s for PO-HI-2D, respectively. Even though there is a degradation of the forecast performance with increasing lead-time, it is not very significant for second day versus first day results, and

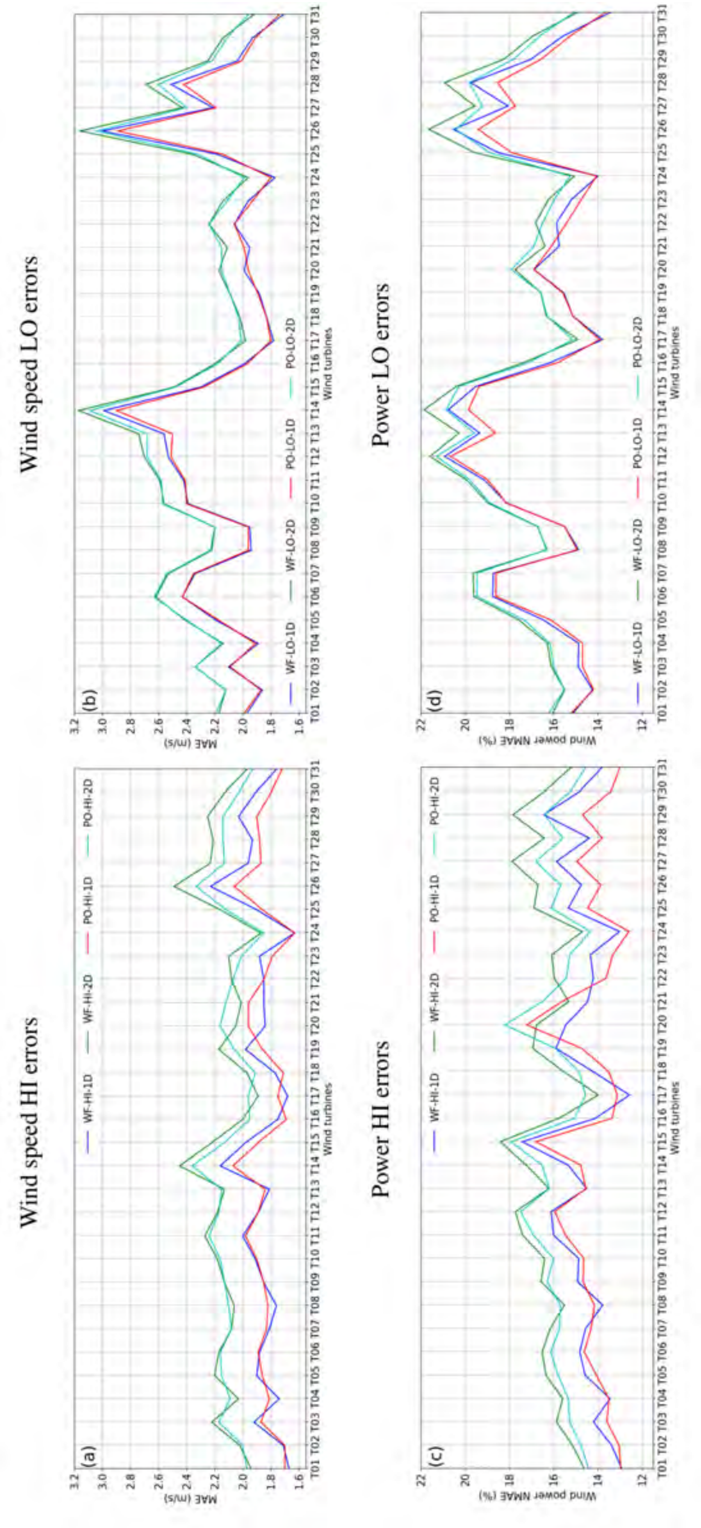

Figure 2.3: (a,b) Annual wind speed MAE and (c,d) wind power NMAE for all wind turbines. Results for the two configurations with and without wind farm parameterization (WF and PO) and with the two different lead times (24 and 48h) are presented. High (a,c) and low (b,d) resolution simulation data are shown separately.

in both cases, errors are relatively small. The impact of a coarser resolution is however much larger (Figure 2.3b and Figure 2.3d), with a pronounced increase errors in some sections of the farm. This variability in forecast skill is likely due to a misrepresentation of the topographic features of the area at lower resolution, which affects some groups of turbines more than others.

The seasonal cycle of errors averaged for all turbines is shown in Figure 2.4, again separately for high and low resolution experiments. Observed monthly mean wind speeds are also shown for reference.

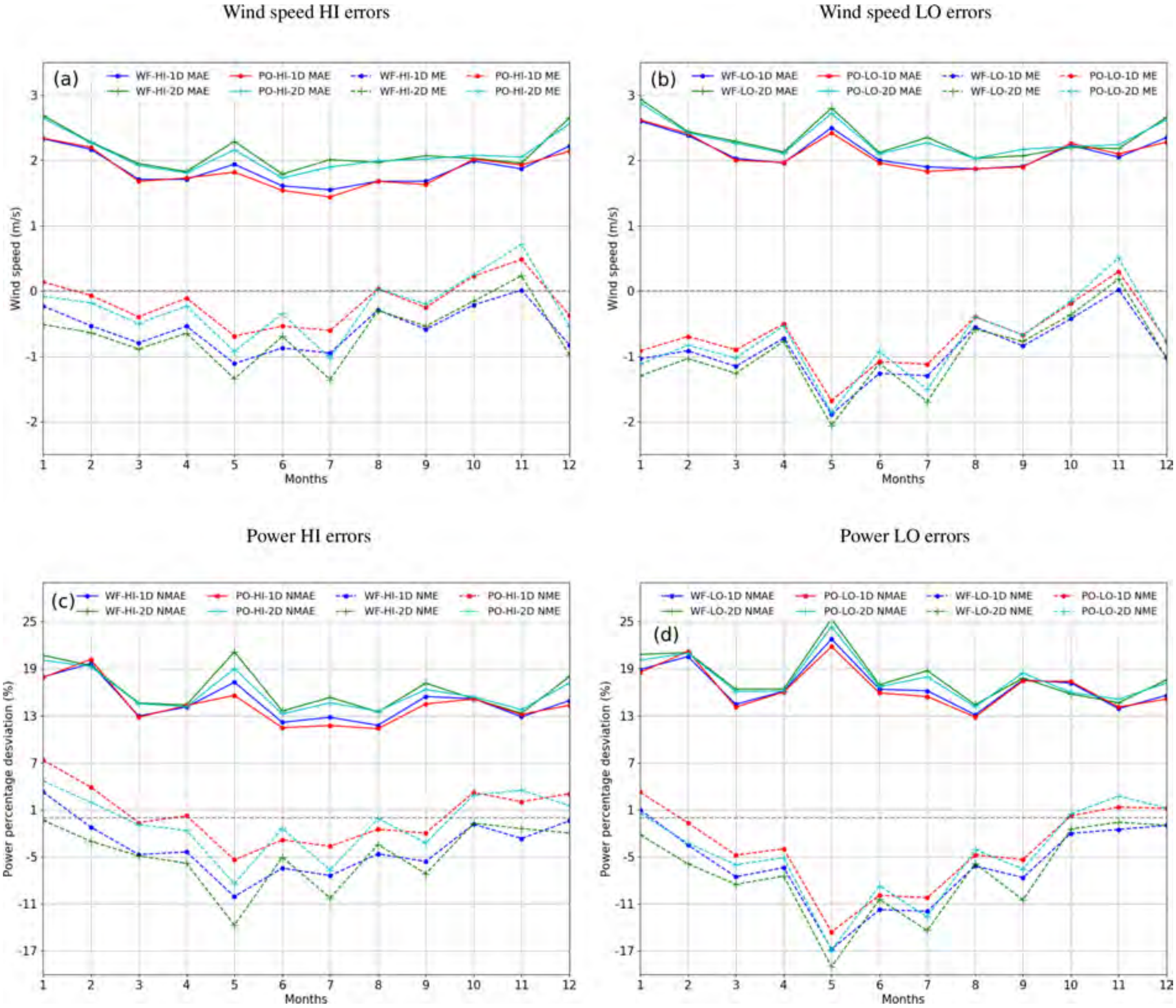

Figure 2.4: (a,b) Monthly wind speed MAE and ME and (c,d) wind power NMAE and NME. Results for the two configurations with and without wind farm parameterization (WF and PO) and with the two different lead times (24 and 48h) are presented. High (a,c) and low (b,d) resolution simulation data are shown separately.

Mean Monthly WS / Mean annual WS											
Jan	Feb	Mar	Apr	May	Jun	Jul	Aug	Sep	Oct	Nov	Dec
1.4	1.16	0.97	0.85	1.07	0.77	0.8	0.76	0.83	1.02	0.88	1.48

Table 2.2: Observed mean monthly wind speed normalized with observed mean annual wind speed.

MAEs are relatively constant throughout the year, with values around 2m/s for all experiments, slightly larger in winter months, when mean wind speeds are higher, and lower in summer months. In general low resolution and second day forecast have worse skill than high resolution and first day forecasts, but performance degradation is not very significant in either case, except for the month of May. For each pair of experiments with (WF) and without (PO) wake parameterization, the latter has a slightly better skill for most months. MEs show a more marked seasonal cycle. They are mostly negative throughout the year, which indicate wind speed underestimations, and these are worse in late spring and early summer than in fall and winter months. NMAEs, with values between 13 and 25 %, and NMEs have qualitatively similar behaviors to MAEs and MEs, respectively.

We examine next errors on a finer timescale. Figure 2.5 displays the mean hourly wind speed MAE, ME and NMAE for the 48h forecast periods of simulation covering the whole year. The observed mean wind speed variations in a day are also shown for reference (Figure 2.5d).

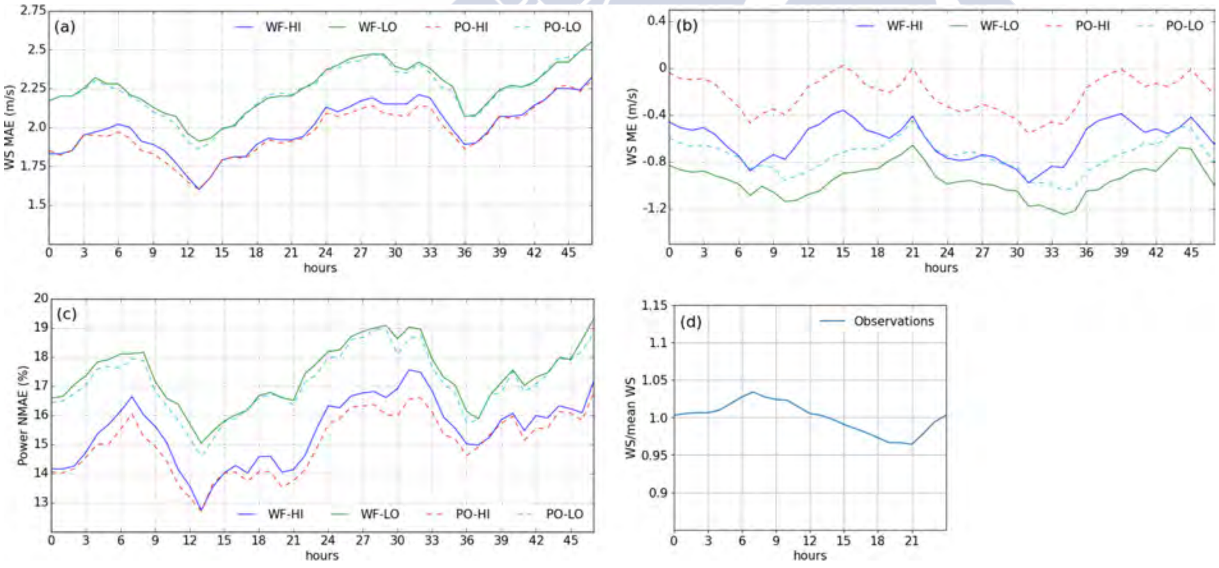

Figure 2.5: (a) Annual wind speed MAE, hourly for the entire simulation period (48 hours). Each line represents 1D (0 to 24h) and 2D (24 to 48h) cases, WF-HI (blue), WF-LO (green); PO-HI (red) and PO-LO (cyan). (b) same as (a) but for wind speed ME.(c) same as (a) but for wind power NMAE. (d) Observed annual mean hourly wind speed normalized with observed mean annual wind speed.

Errors in all cases show a noticeable daily cycle, with values of the MAE around noon clearly lower than during the night. For example, the MAE in WF-HI, already starts at 1.8 at 00UTC, then rise to 2.02 m/s at 06:00 UTC, to decrease to 1.60 m/s at 13:00 UTC , around midday in the area, which is in a GMT+1 time zone (GMT+2 in daylight saving time). Errors grow again in the afternoon and repeat a similar cycle for the later 24h in the forecast, with higher values due to the increasing lead time. There is a close correspondence between the diurnal cycle of MAE and that of NMAE. Minima and maxima values occur at the similar times of the day, with the lowest NMAE of 12.73 % in WF-HI, recorded at 13:00 UTC, the fist 24h of forecast. MAEs and NMAEs follow only loosely the daily cycle of wind speed (Figure 2.5d), and it is likely that there are other factors related to the representation of turbulence fluxes explaining the lower absolute errors at noon. MEs (Figure 2.5b) are negative at all times and for all experiments, indicating an underestimation of wind speeds. In the low resolution experiments, this negative bias shows a daily cycle closely following that of wind (Fig. 5d), with maximum and minimum errors corresponding to maximum and minimum wind velocity, at around sunrise and sunset, respectively. For high resolution experiments, the ME is largest at around 6 UTC, same as for MAEs and NMAEs, and decrease in general in the central hours of the day, but later than the time of minimum MAE and NMAE, which is around noon.

Some of the persistent negatives MEs are likely due to an overrepresentation of turbulence in these simulations. With the high resolution used, at least part of the turbulent processes are dynamically resolved, in addition to being parametrized by the PBL scheme, leading to a ’double counting’ that increases mixing and slows down the flow. The general behaviour of errors throughout the day is likely the result of a better performance of the PBL parameterization during daytime hours, when there is more turbulence and better mixing, than during the night. The lower wind speed underestimation at the central hours of the day corresponds to a lower overestimation of the turbulence. In contrast, throughout the night the temperature vertical profiles can be more difficult to represent by the model due to their more stratified nature, and therefore, turbulent fluxes worse estimated. The daily cycle in wind speed forecast skill that we observe has been described previously in several studies [74].

Aside from the commented diurnal pattern, wind speed MAE and wind power NMAE grow gradually with forecast length. Power NMAE at 13 hours of day 1 is 12.73 % and at 13 hours of day 2 increases to 15.02 %. This degradation of skill, albeit small, is important to an operative forecast system, where each one per cent of error would suppose a problem to the electric system operator and an economic loss for the energy producer. With regard to the effect of spatial resolution, there is a clearly gap between HI and LO cases throughout the day. For example, in terms of wind speed MAE, WF-LO has always around 0.25 m/s higher values than WF-HI.

The location of the turbines in the wind farm clustering in three areas (Figure 2.2c) allows naturally for a separate analysis for each section (Table 2.3) As shown in Figure 2.3a there are no significant differences in wind speed MAE among turbines, therefore it is possible to consider any of these areas as representative of the wind farm.

To illustrate the day-to-day results of the WRF forecasting tool in terms of wind speed at hub height, we show next comparisons between WF-HI-1D, PO-HI-1D and observations for the central area of the farm for the entire months of December and June. These months have the highest and lowest MAE for WF-HI-1D (Figure 2.6), respectively. Mean monthly wind power NMAE and wind speed MAE for the area and the total wind farm are also presented aside.

Notwithstanding some occasional large errors, in general, the predicted WF-HI-1D wind

Area	Wind turbines	WS MAE (m/s)
North	T01 to T10	1.81
Center	T11 to T19	1.89
South	T20 to T31	1.90

Table 2.3: The three wind farm areas with their wind speed annual MAE.

coincides well with the observations, consistently and not just in the mean sense. PO-HI-1D forecast results are always very close to those of WF-HI-1D, in agreement with the similarity in all error measures between the two configurations shown in Figure 2.3. Lower MAE values in June and also in the rest of the summer (Figure 2.4) are likely due to lower wind resource during this season (Table 2.2). Wind speeds are significantly higher during winter, especially in December, which means that in winter months there are more situations where wind turbines are working at nominal power and therefore, even when wind speed MAEs are higher, wind power forecast errors remain quite similar during the whole year.

An overall summary of the different error measures computed for the two configurations with and without wake effects, at high and low resolution and for first and second day forecasts is shown in Table 2.4.

CASE	POWER NMAE (%)	MAE WS (m/s)	ME WS (m/s)	RMSE WS (m/s)
WF-HI-1D	**14.75**	**1.87**	**-0.58**	**2.46**
WF-HI-2D	16.36	2.13	-0.66	2.81
WF-LO-1D	16.89	2.15	-0.93	2.82
WF-LO-2D	17.99	2.34	-0.98	3.10
PO-HI-1D	**14.37**	**1.86**	**-0.18**	**2.43**
PO-HI-2D	15.93	2.09	-0.26	2.79
PO-LO-1D	16.66	2.14	-0.72	2.79
PO-LO-2D	17.77	2.33	-0.78	3.08

Table 2.4: Annual wind power NMAE and annual wind speed MAE, ME and RMSE calculated for all experiments. The lowest values among each configuration (WF and PO) are bold.

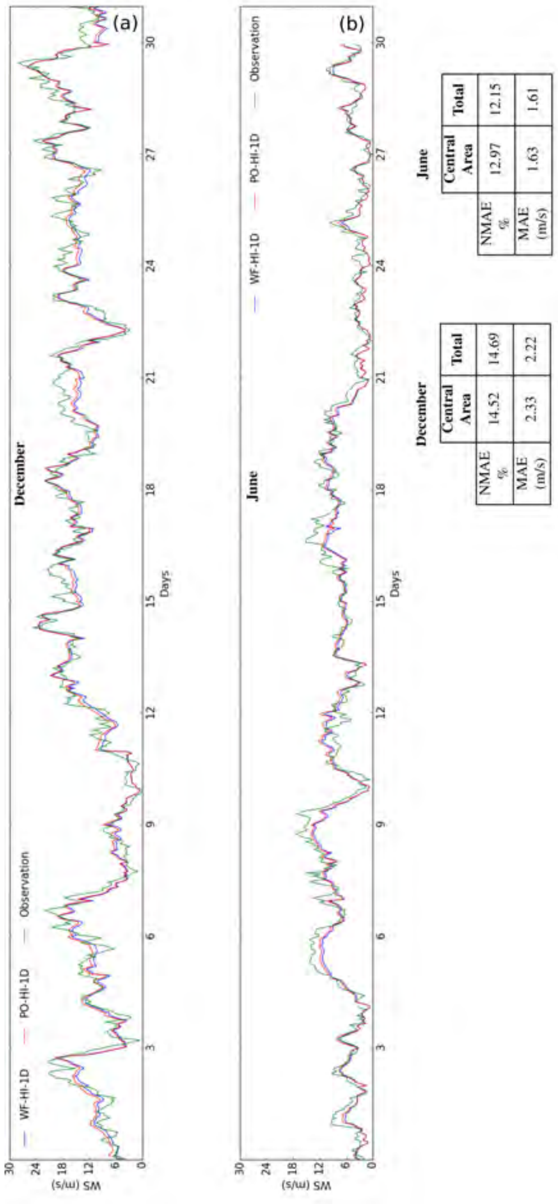

December

	Central Area	Total
NMAE %	14.52	14.69
MAE (m/s)	2.33	2.22

June

	Central Area	Total
NMAE %	12.97	12.15
MAE (m/s)	1.63	1.61

Figure 2.6: (a) December and (b) June mean wind speed (m/s) at hub height in the central area of the farm for the WF-HI-1D (blue) and PO-HI-1D (red) experiments and observations (green). Tables at right display monthly wind power NMAE and wind speed MAE for the area and for the total wind farm for WF-HI-1D.

As discussed earlier in this section, low resolution (LO) and second day (2D) experiment errors are always higher than for high resolution (HI) and first day (1D) cases, respectively. With regard to the differences between simulations with (WF) or without wake effects (PO), errors are very similar, but in general, there is always a slightly better skill for the control (PO) experiments. Only MEs are significantly different for both configurations, with clearly more negative values for WF cases, which indicate a more pronounced underestimation of wind speeds. This suggests that the turbulent enhancement downwind of the turbines might be overestimated by the wake parameterization, leading to more mixing and moment loss in the simulated flow.

In a wind power forecast, the wind situations corresponding with the wind turbine power ramp, which is the ascending part of the wind curve before the nominal power (Figure 2.1a, between 5 and 13 m/s), have the biggest effect in forecast skill. Table 2.5 shows the same errors as in Table 2.4 but for observed power ramp winds only.

CASE	POWER	MAE	ME	RMSE
	NMAE (%)	WS (m/s)	WS (m/s)	WS (m/s)
WF-HI-1D	**19.79**	**1.94**	**-0.67**	**2.51**
WF-HI-2D	21.38	2.19	-0.71	2.87
WF-LO-1D	22.64	2.28	-1.00	2.93
WF-LO-2D	23.43	2.46	-1.02	3.19
PO-HI-1D	**18.76**	**1.87**	**-0.13**	**2.41**
PO-HI-2D	20.53	2.13	-0.18	2.79
PO-LO-1D	21.96	2.24	-0.70	2.87
PO-LO-2D	22.76	2.42	-0.72	3.14

Table 2.5: Annual wind power NMAE and annual wind speed MAE, ME and RMSE for all experiments for power ramp winds only. The lowest values among each configuration (WF and PO) are bold.

In general, results for power ramp winds are qualitatively similar to those for all wind speeds. Error values are however higher, indicating skill degradation. The increase in absolute value is around 5% for the NMAE and 0.1 m/s for the wind speed MAE, for all cases. The only improvement registered in comparison with the total data is in the wind speed ME for PO cases. The mean errors in Table 2.4 for HI-1D cases are lower than others from similar studies in complex terrain [44, 53, 75] and they are also slightly below other operative forecasting with WRF as [74].

Results by wind direction

In the previous section we concluded that results in WF-HI-1D and PO-HI-1D experiments are quite similar in general for the considered wind farm. The main function of the WF-S is to simulate the wake produced by the wind turbines, and the effects of these wakes on the neighbouring wind turbines depend to a large extent on the incoming wind direction. Figure 2.7 shows the annual wind roses of the three wind farm areas obtained from observational data.

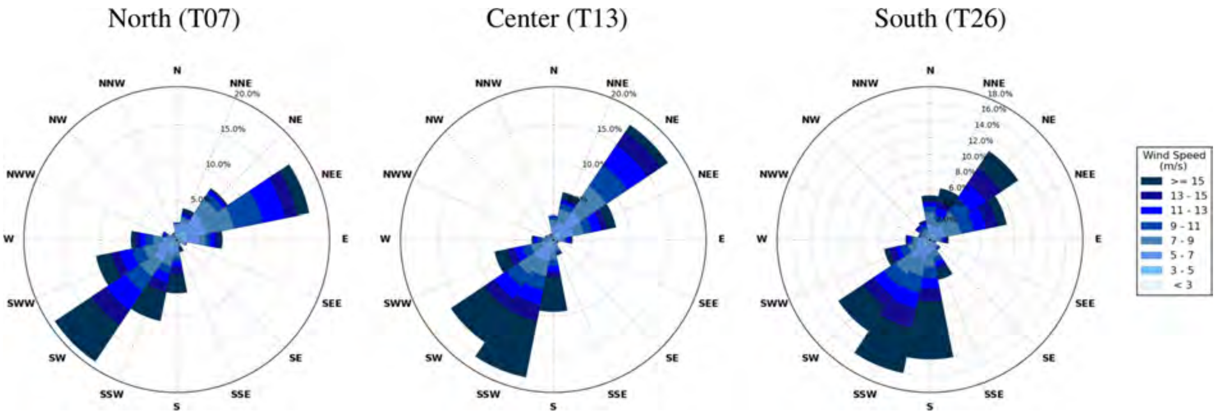

Figure 2.7: Annual wind roses from observational data at hub height at turbines in the (a) north, (b) center and (c) south sections of the farm.

DIR (%)	N	NE	E	SE	S	SW	W	NW
North	6.95	18.66	15.82	2.92	12.45	27.43	12.11	3.66
Center	8.84	25.27	6.83	2.78	18.23	27.20	7.25	3.60
South	10.21	20.89	6.69	4.33	23.38	22.34	6.67	5.49

Table 2.6: Wind direction percentages in T07, T13 and T26.

The wind direction registered is the same as the prevailing wind directions in Galicia (southwest-northeast). The perpendicular orientation of the farm (Figure 2.2b and Figure 2.2c) with respect to this axis of main wind directions explains why there are similar results between WF and PO cases. The wind farm orientation is optimal for its location and the wakes produced by the wind turbines do not have a significant effect on the wind farm itself. For this reason, in order to better study WF-S performance in these simulations, we analyze results relative to wind direction. The charts in Figure 2.8 show wind power NMAE as a function of direction for all experiment pairs with and without wake parameterization.

Considering the impact of wakes reduces errors for north, northwest and southeast winds and most notably in the high resolution first day forecast (WF-HI-1D). Some small degradations of skill are obtained for south-westerly winds. Northerly winds, for which there is a clear positive impact of the wake parameterizaton, represent only between 7 and 10 % of cases, according to the roses in Figure 2.7, thus they contribute to a small improvement in overall skill scores. The slight negative contribution in the much more frequent southwest wind direction offsets these benefits. In spite of not being among the most frequent wind directions, the situations where WF-S is useful still encompass a large amount of data, since a 1 % of wind data is equivalent to around 90 hours.

The dependence of the impact of the wake parameterization with wind direction is more evident when the three sectors of the farm are analyzed separately. Figure 2.9 displays charts similar to those in Figure 2.8, but for each area of the farm individually and only for high-resolution, first day cases (HI-1D). In the northern sector, wakes from the rest of the farm

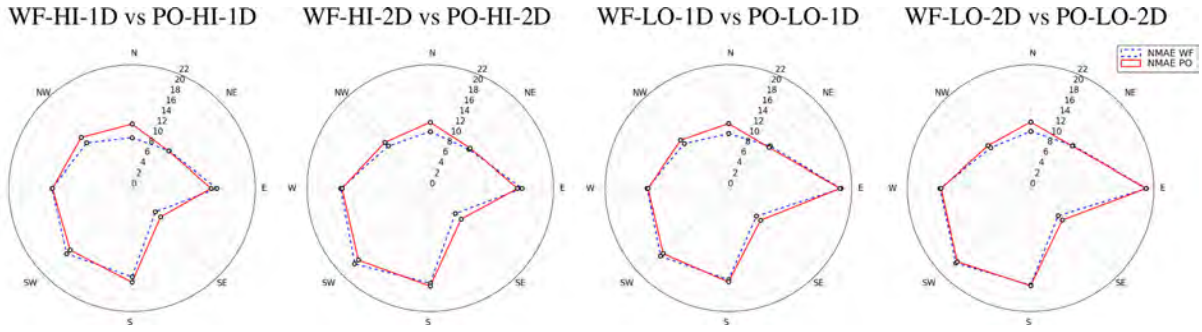

Figure 2.8: Directional radar charts .comparing NMAE by direction, for the different pairs of experiments with (WF) and without (PO) wake parameterization: (a) HI-1D, (b) HI-2D, (c) LO-1D and (d) LO-2D cases.

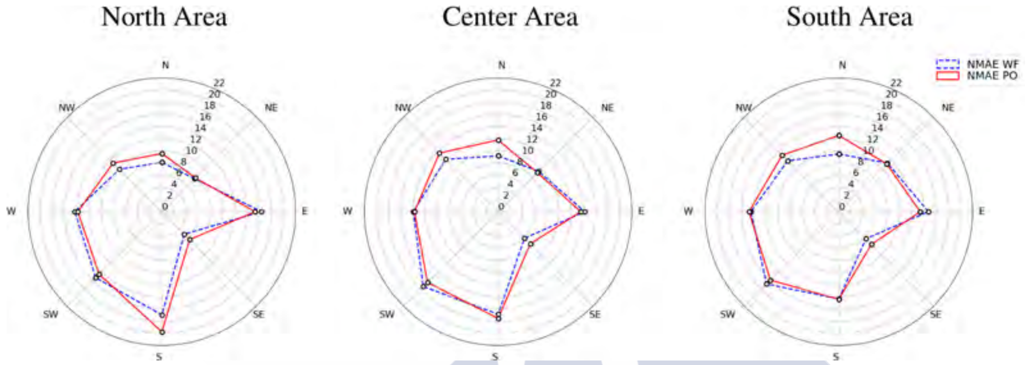

Figure 2.9: Directional radar charts as in Figure 8, but separately for each wind farm area ((a) north, (b) center, (c) south) and for HI-1D cases only.

have an impact with southerly winds, which is when the WF-S scheme proves most useful, reducing errors significantly. For the central and southern sectors, on the contrary, it is with northerly winds that the turbines are mostly affected by wakes, and again in these situations the wake parameterization has a clear positive impact in skill scores. The southern area of the farm is at higher elevation than the rest, thus the central sector is not so affected by wakes with southerly winds.

Figure 2.10a displays the wake produced by the wind farm with Northerly flow, which is the wind direction turning this wake onto to the farm itself. In contrast, Figure 2.10b depicts a southwesterly wind wake, which is, as commented above, the most common situation. Wakes are represented by the difference in wind velocity between the experiments with (WF-HI-1D) and without wake parameterization (PO-HI-1D) at hub height. In addition, time series of hourly mean wind speed for the selected two day periods are shown for observations, WF-HI-1D and PO-HI-1D simulations for turbines T03 and T29 (the third from the north and south ends of the farm, respectively).

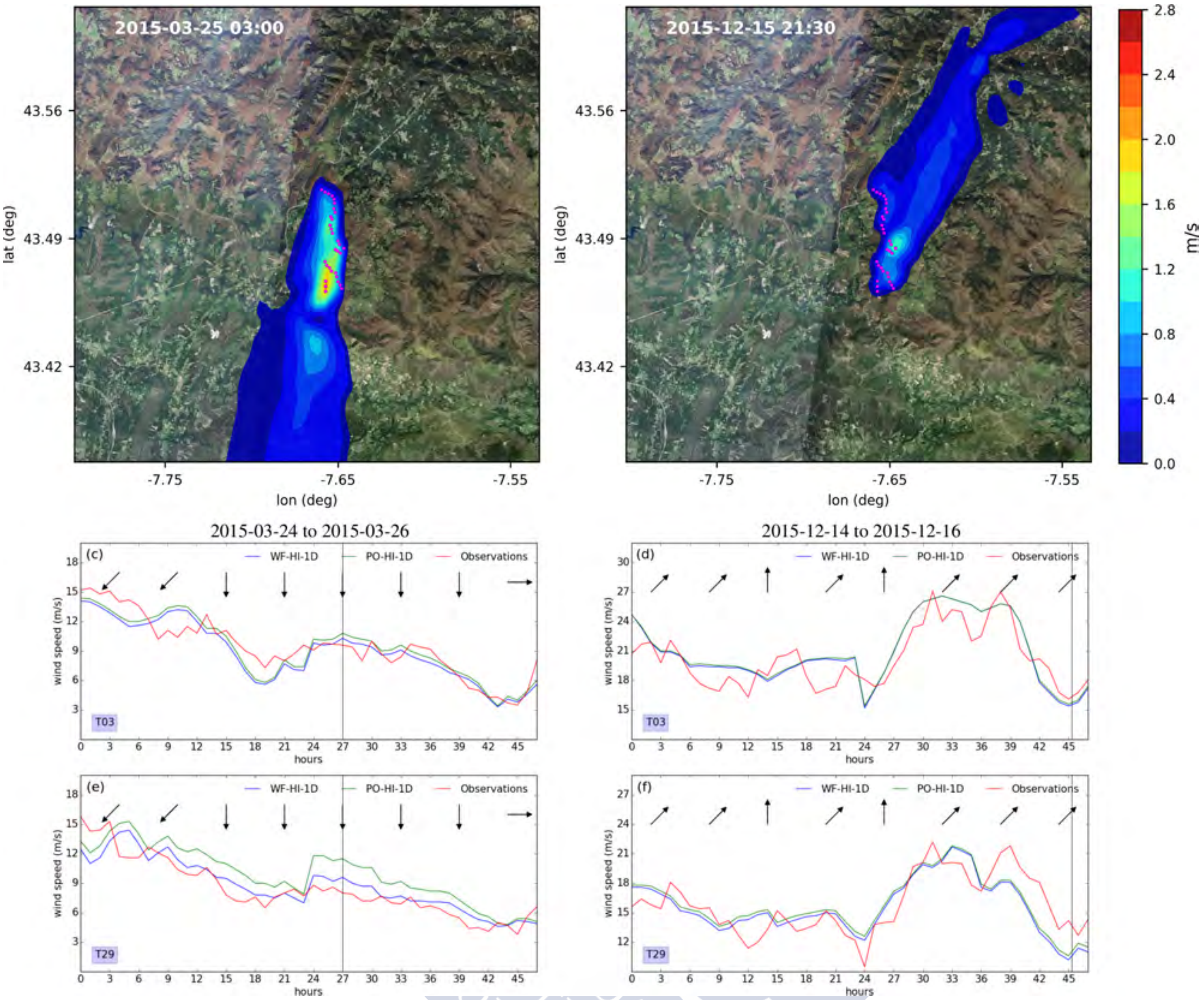

Figure 2.10: (a) Wind farm wake produced by a northerly wind, represented by wind speed losses. Two-day wind speed time series for two different wind turbines, (c) T03 (in the northern area) and (e) T29 (in the southern area). Arrows in each panel indicate wind direction and a vertical black line marks the time frame represented in (a) above. Curves display forecasted wind speed in WF-HI-1D (blue) and PO-HI-1D (red) experiments compared with observations (green). Panels b, d and f are similar to a, c, e, respectively, but for a case corresponding to a southwesterly wind period.

Wakes in both cases extend for several kilometers, and they are more intense for northerly flows, when the perturbation from all turbines overlaps. They interact with the orography and produce non-homogenous areas of resource loss. Precisely, in the northerly wind case (Fig 10a), after moving across a valley and a terrain elevation, the wake reaches the simulation domain boundary, which implies a 15 km-long area of wind speed losses between 0.5 and 2.5 m/s. In contrast, the southwesterly wind wake shown in Figure 2.10b evidences that the total disturbance created in the most common situation for the area, produces a barely noticeable wind loss in the considered farm. This is due to the aforementioned optimal orientation of the turbines, and explains the similar results obtained between WF and PO experiments in the mean annual sense.

The time series in Figure 2.10 for turbines at both ends of the farm indicate that, for the case of a northerly wind wake, the simulation with wake parameterization (WF-HI-1D) is indeed clearly closer to observations at the south end of the farm, where the perturbation effect is mostly felt. Results for PO-HI-1D depart from the observed value much more than for other situations, and the difference between WF and PO experiments is around 2 m/s, which is quite significant. In all other cases, when the wake is not directly impacting the turbines, the differences between WF and PO simulations are minimal, and both experiments follow observations reasonably well. In summary, WF cases always achieve better results than PO in situations where the wakes clearly affect the wind farm itself, thus suggesting that the WF-S scheme provides a good estimation of wake effects in these simulations

Summary and conclusions

In the present study we evaluated the WRF model at high resolution as a wind energy forecasting tool for a real wind farm over complex terrain. In particular, we assessed the representation of wake effects with the WF-S scheme on this particular wind farm as well as on its nearby surroundings. For this purpose, 48h simulations encompassing one year, with two configurations with and without wake parameterization and at different spatial scales and lead times, have been performed and validated with real data. Our results show that wind speed annual mean absolute errors in 333 m resolution experiments considering wake effects are small, of only 1.87 m/s (1.94 m/s for power ramp winds only). These errors present a seasonal cycle, peaking in winter with values of 2.33 m/s in January and decreasing in summer with a minimum value of 1.55 m/s in July. The cycle follows that of wind speed in the region. Moreover, forecast skill scores show also a diurnal cycle, with bigger absolute errors in night-time hours (peak of 2.02 m/s at 6 UTC) than during the day (low of 1.6m/s at 13 UTC), perhaps related to both the daily cycle of wind speed and turbulence intensity. It is possible that at the high resolution used, the model overestimates turbulence, and hence moment loss, since some large turbulent eddies are starting to be resolved in addition to be parameterized. With regard to normalized mean absolute errors for power output, the behaviour of the results is qualitatively very similar to that of mean absolute errors for wind speed. Annual mean values for NMAE are of 14.75 % (19.75 % for power ramp winds only), and oscillate between 19 % inFebruary and and 12 % in August, and between 16.63% at 6:30 UTC (night) and 12.73% at 13 UTC (daytime).

Second day forecasts present some skill degradation and similar trends as first day products. Wind speed mean absolute errors increase from 1.87 m/s the first day to 2.13 m/s on the second, and normalized mean absolute errors for power output raise to 16.36 % from 13.75 % the first 24h. These variations are relatively small, which suggest that the WRF modelling tool results with a 48 h lead time are still very valuable for a real application in the industry. Lowering resolution from 333 m to 1 km has very similar effects to increasing forecast lead time by 24h, Skill scores for the first day in low resolution experiments are almost identical to those of second day forecasts at high resolution, and they further degrade as simulation time progresses. The impact of resolution is important for this farm, given the complexity of the terrain of the area, which is much better resolved at 333m than at 1km grid space. Forecasts with and without considering wake effects have nearly the same mean errors. The spatial distribution of the turbines is optimal for the location, since they are oriented perpendicular to the prevailing wind directions in the southwest-northeast axis, hence minimizing wake impacts. Notwithstanding, forecast skill scores are clearly better when wakes are accounted for in the cases where the farm is directly impacted by its own disturbance, which occurs mostly with northerly flows. However, these represent a small fraction of situations in the area, and the total reduction in errors is therefore not very relevant.


USC
UNIVERSIDADE
DE SANTIAGO
DE COMPOSTELA

Chapter 3

Wind nowcasting

Introduction

Considering the scenarios metioned in the introduction, an improvement of wind energy exploitation seems necessary, employing new strategies in future wind farm projections and better daily management of current installations. The latter is where high-resolution meteorological modeling becomes increasingly prominent. Local short-term forecasts can supply valuable information in an operational wind farm, as wind speed and direction predictions can lead to a better running of the installation [76, 29], as we have seen in previous chapter, or even provide alert for any extreme weather situation such as a downslope windstorm [77] or a severe frost [78].

The Weather Research and Forecasting (WRF) meso and microscale model has been used extensively during the last few years in the wind energy field for a variety of applications [79, 80, 47]. It includes a wind turbine parameterization [35] enabling the study of the wake effect from wind turbines [54, 29]. However, numerical weather model prediction (NWP) simulations by themselves, present some limitations regarding subgrid scale phenomena forecasting. Onshore farms can be affected by local climatology and microscale events with significant wind direction and intensity changes in short periods of time. It is well known that such variations cannot be well reproduced by NWP simulations with resolution lower than that of the small-scale events commented above. To address this problem, WRF Large Eddy Simulations (LES) have been shown to be a useful modeling technique within this field. Their high resolution ($<$100m) allows obtaining a good characterization of the turbulent intensity and an accurate representation of the wind fields [81, 36, 82]. Despite these capabilities, the computational demands of this modeling methodology and its numerical instability over complex terrain [36, 83] make it unfeasible for operational forecasting at the present time.

The combination of NWP and statistical post-processes, like MOS (Model Output Statistics) or dynamically adjustable filters, can be an effective technique to minimize errors induced by sub-grid phenomena and local effects. In this direction, several strategies have been developed. Kariniotakis and Pinson [84], Kariniotakis et al. [85] proposed a neural network approach while Vanem [86], Giebel [87], Resconi [88] and others introduce methodologies based on heavy statistical models. Another method adopted for the reduction of systematic biases that numerical weather prediction models face, is Kalman filtering based algorithms (Resconi [88], S et al. [89], Galanis et al. [90, 91], Crochet [92], Galanis and Anadranistakis [93], Kalnay [94], Kalman and Bucy [95], Kalman [96]). Stathopoulos et al. [97] used the combination of an ETA-coordinate weather prediction model (running at a resolution of 0.05 degrees) and a Kalman Filtering postprocess for wind power prediction. This showed an improved performance and favorable results. Hua et al. [98] use 3km x 3km WRF model simulations and a Kalman Filter to obtain more skillful wind speed forecasts. Che et al. [44], Che and Xiao [45] developed a similar forecasting system employing 0.5 km resolution WRF simulations with a Kalman filter for a wind farm in Japan. Despite the overall good performance, in many cases, such filters only reduce the systematic mean bias [99], especially in wind speed, due to the nature and variability of the parameter. A proposed solution for this drawback is described analytically in Galanis et al. [31]. The suggested optimization technique is emerging from the conjunction of a non-linear Kalman filter and a Bayesian model (K-B model). This new hybrid model led to promising results eliminating systematic biases in the model outputs and reducing the variability of the remaining white noise.

In this study, we develop and validate a combined system of WRF high-resolution simulations and the aforementioned K-B filter. The main novelty proposed is the application of the hybrid filter to the two-dimensional field of horizontal wind speed components instead of the 1-dimensional filter in Galanis et al. [31]. In this way, an improved prediction of wind speed and direction is produced for a very dense wind farm cluster located in Galicia (NW Spain). A period of one year, broken into 365 daily integrations, is simulated with the WRF atmospheric model at high resolution (333 m), and results post-processed with the K-B filter.

The obtained integrated system is validated for different short-term forecast periods employing in-situ data from meteorological stations on the top of the wind turbines provided by the farm's operator. In addition, the new wind direction nowcasting tool is applied to the wind energy field as a backup for the current yaw orientation systems, which are based on SCADA data obtained from each wind turbine [100]. These sensors are sometimes affected by short temporal errors due to technical problems or severe meteorological situations. Apart from the wind farm operational issue, this kind of tool can be used by electric grid operators to prevent ramp event effects. These extreme short-term situations produce significant increases or drops in the power production [28], delivering a major impact on the grid.

The chapter is structured as follows: In Section 2 the methodology is explained in detail, with particular attention to the WRF model configuration and the K-B filter description. Section 3 discusses the results obtained for wind speed and wind direction nowcasting as well as applications on wind energy forecasting. Finally, in Section 4 conclusions are presented.

Methodology and data

Wind farm location and WRF configuration

The wind farm studied is Coruxeiras (Chapter 1), located in Serra do Xistral mountains in Galicia, in northwest Spain (Figure 3.1a). The prevailing winds in this area are in the southwest/northeast direction (Figure 3.1c). In winter, frequent passing by cyclones along the North Atlantic storm track often produce strong southwest flows, whereas in summer, the poleward displacement of the subtropical Azores high, results in winds with a northeast component. Southeast/northeast flows are further accelerated due to the packing of the isobars by interaction with the high terrain of the northwestern Iberian Peninsula; hence the position of Serra do Xistral, exposed to the ocean in both prevailing directions, results in a very high wind energy potential. As commented before, this area is one of the most productive in Europe

[62, 61]. The developer and current operator of Coruxerias wind farm is Norvento S.L.U. company. It was installed in 2006 and is composed of 31 turbines with 60 m hub height and 74 m rotor diameter. They are separated by a mean distance of 300 m and placed along smooth hill tops of around 800 m elevation above sea level, (Figure 3.1b).

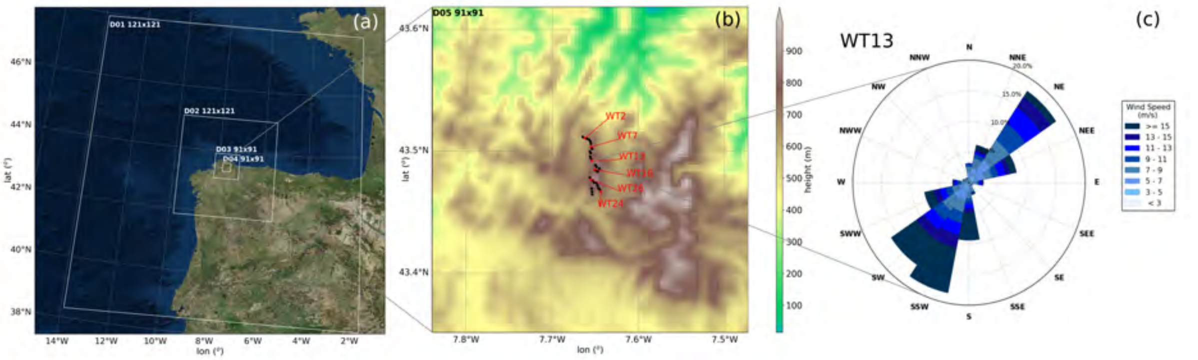

Figure 3.1: (a) WRF nested grid configuration, with the number of points for each domain indicated. (b) D04 is expanded showing its topography. Coruxeiras wind farm is located in the central area of D04, on top of a hill. Observational data for the study is obtained from meteorological stations at the hub of the wind turbines plotted in red. (c) Annual wind rose from observational data at hub height from a wind turbine in the center of the farm (WT13).

For the atmospheric simulations, we use the Advanced Research WRF (ARW) model version 3.6 [101] (WRFV3.6). The configuration of simulations is the same as in Chapter 1. Figure 3.1a shows the domain's configuration where D01 is centered at 43.29 N and 7.75 W (Figure 3.1a) with 121x121 grid points of 9 km of horizontal resolution. The horizontal resolutions of D02, D03, and D04 are 3 km (121x121 grid points), 1 km (91x91 grid points) and 333 m (91x91 grid points) respectively. As demonstrated in Chapter 1, the high horizontal resolution used over this complex terrain increases the accuracy of the wind forecast. The innermost domain has 67 vertical levels, 7 of which lie within the first 200 m above ground, at about 14, 41, 70, 99, 127, 156 and 184 m, a distribution that better captures wind and temperature variations in the surface layer [67] and improves the performance of the wind turbine parameterization [35]. Terrain elevation data is obtained from the ASTER Global Digital Elevation Map (GDEM) from USGS (United States Geological Survey) [66] with a resolution of 30 m, and land use information from the Corine (Coordination of Information on the Environment) database [65] with 250 m resolution.

A thorough validation of this model configuration for Coruxeiras wind farm and more information about the model physics options can be found in previous chapter. In Table 3.1, we present the main physics parameterizations used.

Microphysics	Single-moment six-class scheme [70]
Cumulus Parameterization	Kain-Fritsch scheme [73] *disabled in d04 and d05
Long wave radiation physics	RRTM Longwave model [68]
Short wave radiation physics	Dudhia shortwave radiation schemes [69]
Planet boundary layer	Mellor–Yamada Nakanishi Niino Level 2.5 [72]
Surface layer option	Revised MM5 Monin-Obukhov scheme [102]
Land-surface physics	Noah land-surface model [71]
Wind Turbine Parameterization	Fitch, A. C. 2012 [35]

Table 3.1: The principal physical schemes used in the atmospheric model

Hybrid Kalman Bayesian filter

In this subsection, the statistical optimization postprocess adopted is presented. Beginning with the polynomial Kalman filtering local adaptation model, the main goal is the estimation of the atmospheric model bias y_t as a function of the model output m_t.

$$y_t = x_{0,t} + x_{1,t} \cdot m_t + v_t \tag{3.1}$$

where $x_{1,t}$ are the parameters to be estimated and v_t is the Gaussian nonsystematic error.

The above equation can be expressed as $y_t = H_t \cdot x_t + v_t$ where $x_t = \begin{bmatrix} x_{0,t} & x_{1,t} \end{bmatrix}$ is the state vector and $H_t = \begin{bmatrix} 1 & m_t \end{bmatrix}$ the observation matrix. As a result, it can be written in a more analytical way as follows:

$$y_t = \begin{bmatrix} 1 & m_t \end{bmatrix} \cdot \begin{bmatrix} x_{0,t} \\ x_{1,t} \end{bmatrix} + v_t \tag{3.2}$$

Similarly, the evolution in time of x_t is described by the equation

$$x_t = x_{t-1} + w_t \tag{3.3}$$

where x_{t-1} is the parameter in t-1 and w_t is the Gaussian nonsystematic error.

In the present study, a linear approach is followed, since it was found to be sufficient both in terms of reliability and computer resource needs. The unknown variables must be estimated before the application of the filter; based on a training period. For this case, the training period was set to include the last 12 values of the sample for each forecast.

We note, however, that options such as the order of the equation used or the training period, are case sensitive and depend on local features and time period characteristics. More details on the Kalman filtering theory can be found in [94, 95, 96]. The filter has been tested successfully in wind speed and wind gust prediction Stathopoulos et al. [97], Louka et al. [99], Patlakas et al. [103], Galanis et al. [31] with results that ensure the reduction of the systematic errors induced by numerical weather models.

However, in most of the previous studies, the variation of the remaining nonsystematic part of the error is not reduced. For a further improvement of the Kalman filter output, we incorporate the following linear Bayesian model:

$$k_t = o_t + n_t \tag{3.4}$$

where, k_t represents the Kalman filtered output at time t (estimated by the Kalman filter as the model initial forecast corrected by y_t), o_t is the corresponding observation value, and n_t the remaining Gaussian nonsystematic white noise. For the application of the Bayesian model, an approach based on Normal distribution is utilized. Further details concerning Bayesian theory and models can be found in the studies of Box G. [104] and Bernardo and Smith [105], while the combination of the two approaches is fully described by Galanis et al. [31].

The new approach proposed in this work consists in the application of the K-B model for both wind speed and U-V components for different forecasting horizons, covering in this way both wind speed and direction with quite satisfactory results as presented in the following sections.

Observational data and nowcasting experiments

The observational data used in this work is provided by Norvento S.L.U., collected from anemometers located on top of each turbine's nacelle. Specifically, we use wind speed and wind direction (WS and WD hereafter) observations from six wind turbines, two in the north of the farm (WT2 and WT7), two in the center (WT13 and WT16) and two in the south (WT24 and WT26) (Figure 3.1b). In this way, the WRF K-B nowcasting tool is tested all over the wind farm, with each turbine differently affected by wake effects and local topography. One year of 10-minute wind data for each turbine is available. We note that a priori quality control on the raw observational data is performed, filtering out discontinuities such as automatic starts after stops or preventive maintenances.

The period chosen for the present study is one year (2015/02/01–2016/02/01), divided into 365 daily simulations. Each run starts at 18 UTC the day before the one considered, and the initial 6h are excluded from the forecast data series used in the analysis of the results, thus, only outputs after this spin-up time are taken into account.

By definition, nowcasting refers to short lead time weather forecasts. Some organizations like the U.S. National Weather Service stipulate that it pertains to lead times from zero to three hours. However, forecasts up to six hours are also considered nowcasts by different agencies [106]. To analyze the capabilities of our methodology, we evaluate the K-B filter with different nowcasting horizon periods, from 6 hours to 10 minutes (Table 3.2) for each one of the daily simulations. Results are compared with both observations and original non-post-processed WRF outputs.

Experiment	
RAW	WRF results without post-proccess
K-B 6h	K-B filter nowcasting used for 6 hours time horizon
K-B 1h	K-B filter nowcasting used for 1 hour time horizon
K-B 30min	K-B filter nowcasting used for 30 minutes time horizon
K-B 10min	K-B filter nowcasting used for 10 minutes time horizon

Table 3.2: Short explanation of the experiments tested in this study. The bold names on the left are the identifiers used hereafter for each case.

Results and discussion

The next section is divided into three parts; the first one analyzes the results obtained with the nowcasting wind speed postprocess at different time horizons, from 6 hours to 10min in advance. The analysis is developed for different temporal periods, from annual mean results to the performance of the experiments at individual simulation timesteps. The second subsection shows the results of the K-B filter used to measured wind direction correction, same as with wind speed, with different nowcasting horizons and mean errors for several periods. Finally, subsection 3.3 shows an example of the improvement that K-B 1h applied in wind direction could effect in the daily management of the studied wind farm.

Wind speed nowcasting

This subsection employs several error measures at different temporal scales to provide a general view of the skill of all the experiments. The next equations show the statistical measures used in different temporal scales throughout the chapter.

$$MAE = \frac{1}{n}\sum_{i=1}^{n}|f_i - ob_i| \qquad (3.5)$$

$$ME = \frac{1}{n}\sum_{i=1}^{n}(f_i - ob_i) \qquad (3.6)$$

$$RMSE = \sqrt{\frac{\sum_{i=1}^{n} (f_i - ob_i)^2}{n}} \qquad (3.7) \qquad\qquad \sigma = \sqrt{\frac{\sum_{i=1}^{n} |x_i - \overline{x}|^2}{n}} \qquad (3.8)$$

Equation (3.5) gives the Mean Absolute Error (MAE) between forecasts (f_i) and observations (ob_i), (3.6) the Mean Error (ME) estimating possible systematic biases, (3.7) the Root Mean Square Error (RMSE), where n is the sample size, and (3.8) the standard deviation (σ), where x_i is the value, x the mean value of a study period.

Annual mean results are firstly shown in Figure 3.2, and Table 3.2 for each wind turbine studied. Figure 3.2 displays a bar chart with the annual WS MAE and standard deviation for each turbine and experiment performed. Table 3.3 a and b present the annual WS ME and RMSE, again, for each turbine and experiment.

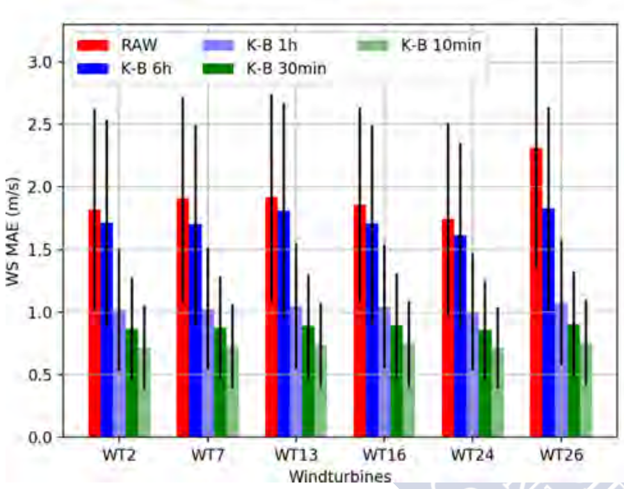

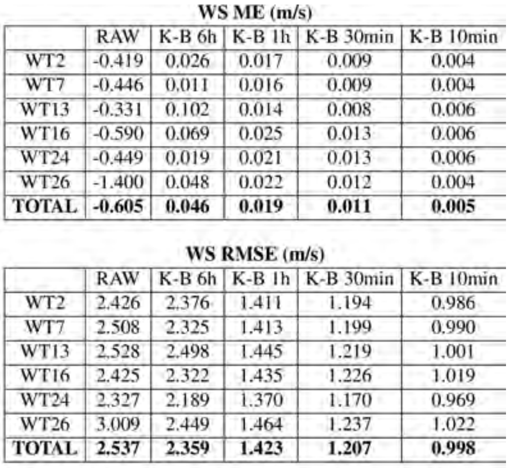

WS ME (m/s)

	RAW	K-B 6h	K-B 1h	K-B 30min	K-B 10min
WT2	-0.419	0.026	0.017	0.009	0.004
WT7	-0.446	0.011	0.016	0.009	0.004
WT13	-0.331	0.102	0.014	0.008	0.006
WT16	-0.590	0.069	0.025	0.013	0.006
WT24	-0.449	0.019	0.021	0.013	0.006
WT26	-1.400	0.048	0.022	0.012	0.004
TOTAL	**-0.605**	**0.046**	**0.019**	**0.011**	**0.005**

WS RMSE (m/s)

	RAW	K-B 6h	K-B 1h	K-B 30min	K-B 10min
WT2	2.426	2.376	1.411	1.194	0.986
WT7	2.508	2.325	1.413	1.199	0.990
WT13	2.528	2.498	1.445	1.219	1.001
WT16	2.425	2.322	1.435	1.226	1.019
WT24	2.327	2.189	1.370	1.170	0.969
WT26	3.009	2.449	1.464	1.237	1.022
TOTAL	**2.537**	**2.359**	**1.423**	**1.207**	**0.998**

Figure 3.2: Barchart with annual WS MAE for all experiments and wind turbines analyzed. For each case, the standard deviation (σ) is represented by a black line on the top of each bar.

Table 3.3: (a) WS ME for all experiments and wind turbines, (b) same as (a) for RMSE.

Overall, a similar improvement concerning WS MAE for all the wind turbines and cases is recorded. Raw WRF forecast MAEs are between 1.91 and 1.74 m/s, except for WT26, which has a RAW MAE of 2.31 m/s. All of these results, regardless of wind farm area, present a small reduction of the WS MAE (of around 10%) in the longest nowcast period, K-B 6h (blue). The accuracy of the K-B filter is significantly enhanced for shorter lead times, with K-B 1h (pale blue) reaching a WS MAE of around 1 m/s in all cases. The shorter nowcasting periods, K-B 30m (green) and K-B 10m (pale green) show further reduction of error, with values around 0.86 and 0.72 m/s respectively. The standard deviations plotted on top of each bar (σ) are also reduced for all turbines, in parallel with the shortening of the nowcasting periods. RAW cases have a mean of 0.82 m/s, and K-B 10 min present a mean value for all of the machines of 0.33 m/s.

The behavior of the WS ME is different as compared with MAE. All of the RAW WS MEs for the six wind turbines are negative, ranging from -0.33 m/s in WT13 to -1.40 in WT26.

Unlike in WS MAEs, there is a clear difference between RAW and K-B 6h MEs. In K-B 6h cases, the ME practically disappears, with a value of 0.046 m/s. In the rest of the experiments, the ME is reduced even more; reaching a total ME of 0.005 m/s for the K-B 10min case. WS RMSEs show a similar tendency to that of WS MAEs, with close mean values of the RAW and K-B 6h experiments (2.54 and 2.36 m/s respectively) and a definite improvement between the three shorter nowcasting periods (K-B 1h-30min-10min) and K-B 6h.

Figure 3.3 analyzes the relationship between the observed and simulated wind field in terms of module and direction. As also discussed previously, there are similar error values and patterns in all of the wind turbines, which allows us to group them by areas while maintaining the rigor of the validation. In Figure 3.3a-c-e the wind speed distribution is displayed for the observations and the RAW, K-B 1h and K-B 6h experiments, for the North, Center and South areas respectively. Radar charts in Figure 3.3b-d-e depict the WS MAE as a function of direction for all experiments and areas.

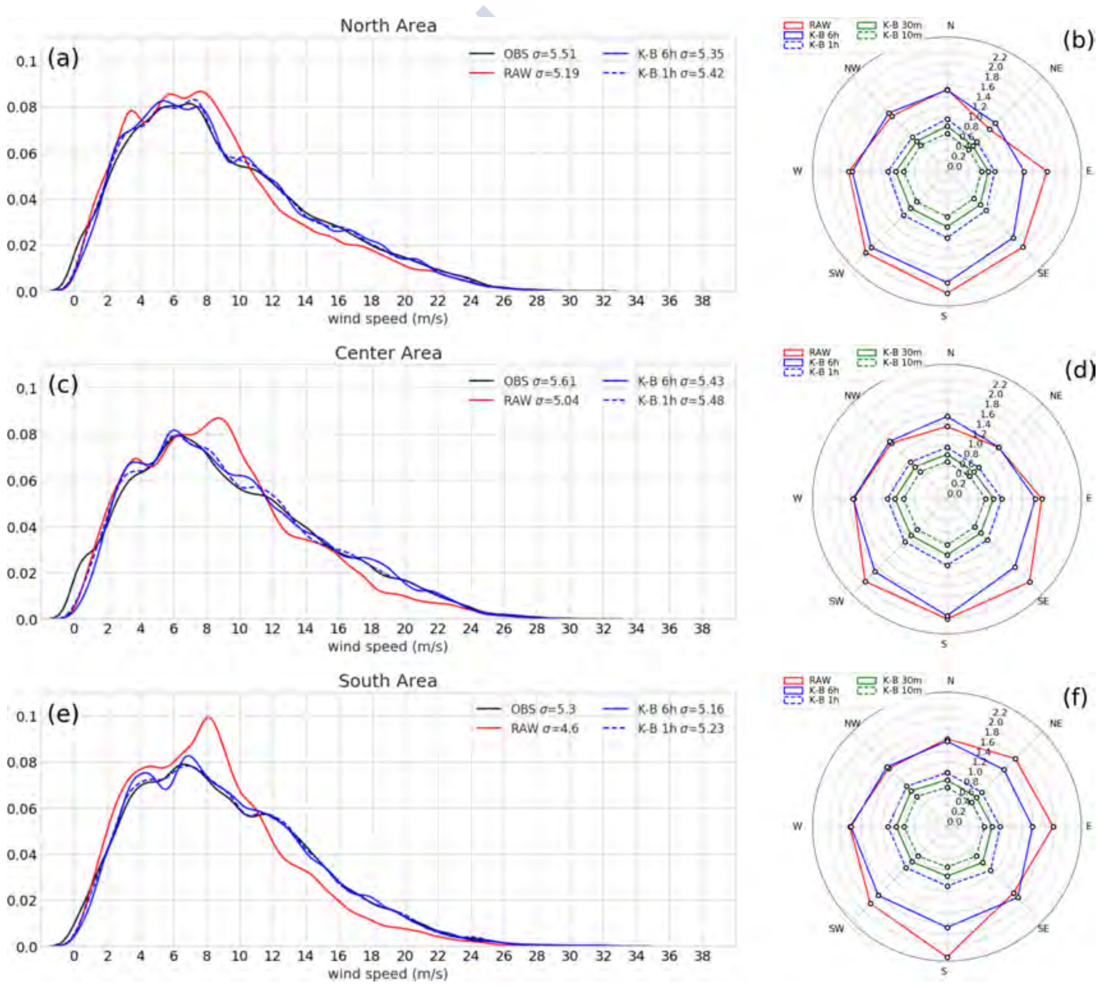

Figure 3.3: (a) Wind speed distribution plot for observations, RAW, K-B 6h and K-B 1h time experiments in the north area of the wind farm. The standard deviation of each distribution is indicated in the legend. (b) Radar charts comparing WS errors by observed wind direction in the north area. (c) Same as (a) for the center area. (d) Same as (b) for the center area. (e) Same as (a) for the south area. (f) Same as (b) for the southern area.

The distribution plots in Figure 3.3a-c-e show a significant improvement from the K-B filter in the three areas. K-B 6h mitigates the main wind speed deviations in all the range of the distributions. In the north area (Figure 3.3a) K-B filter cases correct a general overestimation from 6 to 10 m/s and an underestimation from 11 to 22 m/s. This behavior is repeated in the Central and South areas. K-B experiments (even K-B 6h) obtain an important amelioration of the entire distribution shape, which is in agreement with the low ME errors shown in Table 3.2a. This demonstrates the reliability of the K-B filter in different wind situations, correcting under- and over-estimations indistinctively, which is vital for wind energy applications. Charts in Figure 3.3b-d-f show the skill of the K-B tool depending on wind direction. In RAW cases, the three areas present variations, as the general orientation of each zone and their position relative to the rest of the farm change forecast performance. K-B 6h decreases mainly the higher directional errors as, for example, with southerly winds in the South area (Figure 3.3f). However, the K-B tool for 1h, 30 min, and 10 min tends to smooth out errors from all sources, improving results in all the prevailing wind directions. Apart from the low MAE values observed, the symmetry in the figures in the shorter K-B time ranges leads to the conclusion that the tool is robust, rectifying wind errors in any regime. It presents the same good accuracy correcting northeast flows, principally produced in summer, as it does with southwesterly situations, characteristic of winter months.

The seasonal cycle of errors averaged for all the turbines is shown in Figure 3.4, comparing wind speed monthly MAE from RAW results with the same calculation from K-B experiments. Observed monthly mean wind speeds are also shown for reference in the table below

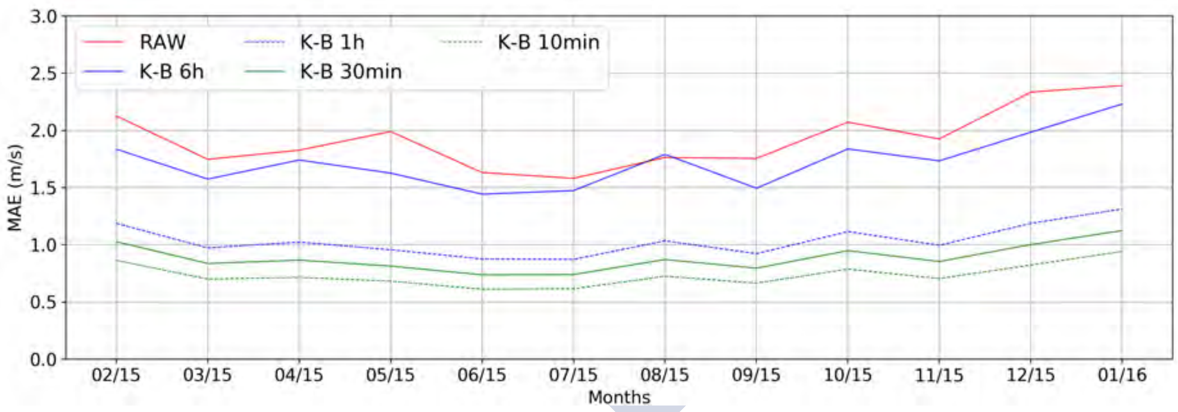

Figure 3.4: Monthly wind speed MAE for the wind turbines with K-B model (6h (blue), 1h (dotted blue), 30min (green), and 10min (dotted green)) and RAW (red).

Mean Monthly WS / Mean annual WS											
Jan	Feb	Mar	Apr	May	Jun	Jul	Aug	Sep	Oct	Nov	Dec
1.4	1.16	0.97	0.85	1.07	0.77	0.8	0.76	0.83	1.02	0.88	1.48

Table 3.4: Observed mean monthly wind speed normalized with observed mean annual wind speed.

RAW MAEs are relatively constant throughout the year, with values around 2m/s in all months. Slightly larger errors are observed in the winter period, when mean wind speeds are higher, and lower biases occur in summer months, when mean wind speeds are also lower. K-B 6h obtains the biggest improvements in the months when the RAW error is largest, such as December or February and minor improvements in the summertime. This tendency to better improve bigger RAW MAE is also reflected in previous comparisons such as for WT26 in Figure 3.2 or the south radar chart in Figure 3.3f. In K-B experiments for shorter lead times, the pattern shown in Figure 3.3 is repeated, with a significant error decrease relative to K-B 6h results and very similar outcomes in all K-B cases and months. The K-B 1h MAEs are all very close to 1 m/s, February registers the higher K-B 1h MAE, with 1.19 m/s and June the lowest, with 0.87 m/s. This equality among monthly errors is maintained in K-B 30m and 10m with mean values all year long around 0.88 and 0.73 m/s respectively.

After investigating the intra-annual behavior and monthly error patterns of the experiments, we examine their accuracy on a finer timescale. Figure 3.5 displays the mean hourly wind speed MAE during the simulated year for all the wind turbines analyzed in each experiment.

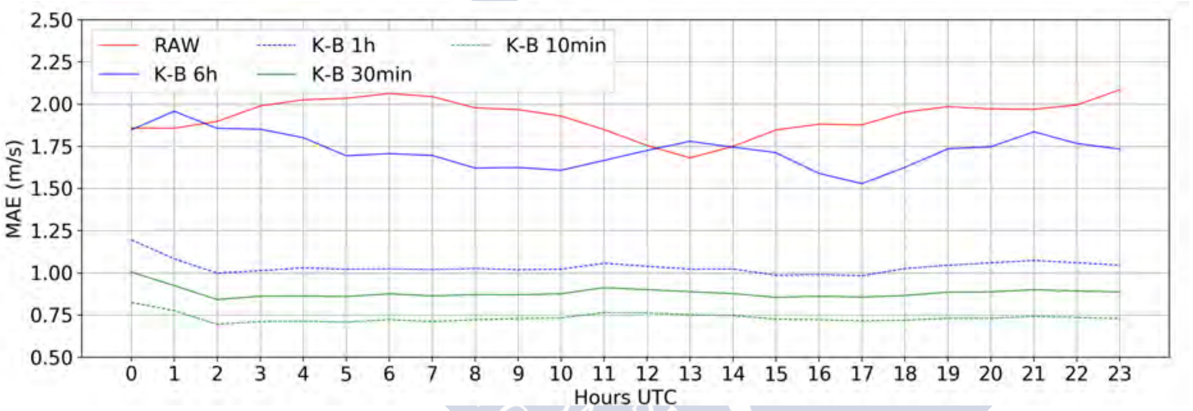

Figure 3.5: Wind speed MAE, hourly for the entire 24 h simulation period with RAW outputs (red) and K-B model cases: K-B 6h (blue), K-B 1h (dotted blue), K-B 30min (green) and K-B 10min (dotted green).

RAW error results present a daily cycle, with values of the MAE around noon lower than during the night. These differences among the hourly WS MAEs are, however, not very significant, and the lower absolute errors at noon seem to be related with the better representation of turbulent fluxes during that part of the day [29]. In contrast, K-B 6h errors do not follow a daily cycle, attaining values below 1.75 m/s mostly during daytime, but obtaining a worse result than RAW at 01 and 13 UTC. K-B 1h, 30 min, and 10 min present a very flat error pattern all day long. There are practically no differences among hourly results in these experiments. The situation is very similar to that in the monthly error plot (Figure 3.4); shorter term K-B cases represent a significant improvement with respect to K-B 6h and RAW, and there is homogeneity in the entire error series in K-B 1h, 30 min, and 10 min. The skill limit for the shorter term cases corresponds to a non-systematic part of the error, which is unavoidable for the filter

The general conclusion reached from the different time scale and wind regime comparisons presented above is that the K-B filter at short-term erases any source of error. It achieves lower errors in all conditions, regardless of the intensity and direction of the wind or the time of day or season of the year. This uniformity in the corrections toward the elimination of the ME (Table 3.1) from short-term K-B cases, highlights the utility of this optimization module for wind energy purposes.

To illustrate the day-to-day results of the K-B nowcasting tool regarding wind speed at hub height, we show next comparisons between RAW, K-B 1h, and observations for the Center area (WT13 and WT16 mean values) during the entire months of May and December. These months have the lowest and highest K-B 1h MAE in this area respectively.

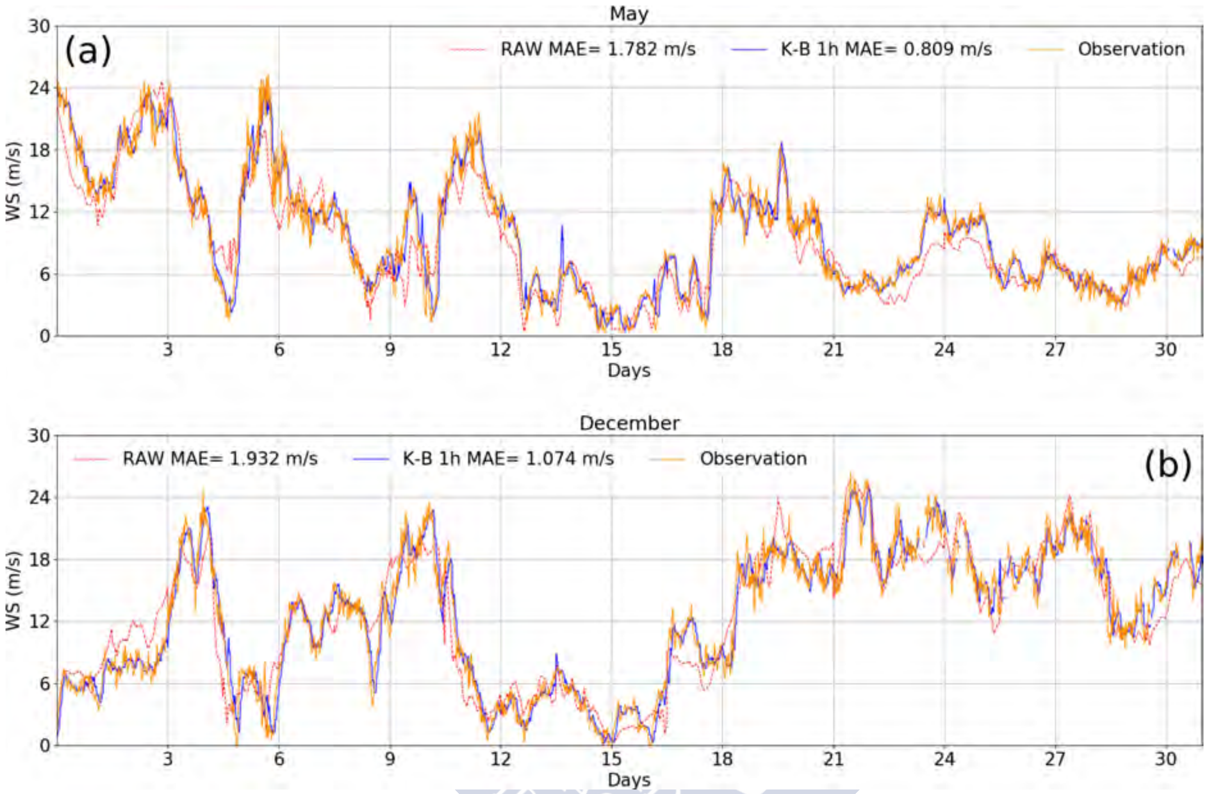

Figure 3.6: (a) Wind speed at hub height in the center area with observations (orange), RAW (dotted red), and K-B 1h (blue) in May. (b) Same as (a) in December. Wind speed MAE for each series is presented in the legend for both figures.

Disregarding some occasional large errors, the original WRF output (RAW) generally yields a good performance during the months shown, achieving MAEs below 2 m/s in both cases. Even considering these low RAW errors, which are extensive to all the yearly series, the K-B 1h results represent an important improvement nonetheless. This is clearly apparent in these December and May plots (Figure 3.6), when the procedure successfully corrects forecast error by a factor of around 50 %. The nowcasting tool is able to produce better results at different time ranges regardless of the origin of the error, eliminating the most substantial deviations in any situation. Overall, the K-B filter exhibits a useful short-term operational forecasting performance, offering a stable improvement of the original WRF outputs during the whole year and for all the wind turbines.

Wind direction nowcasting

Following the discussion on the capabilities of the K-B filter regarding WS (wind speed) nowcasting, we review the statistical tool predicting WD (wind direction) following a similar structure to section 3.1. To perform the WD nowcasting post-process we obtain the zonal and meridional wind components (U and V) from WS and WD observations, and we use them to correct, with the K-B filter, RAW U and V variables directly extracted from the model output. With the corrected U and V, we recalculate the post-processed WD. Using the same process as in the WS analysis, we test the WD nowcasting for different short-term forecast time periods (Table 3.2).

Figure 3.7 displays the annual WD MAE and standard deviation for each turbine and experiment.

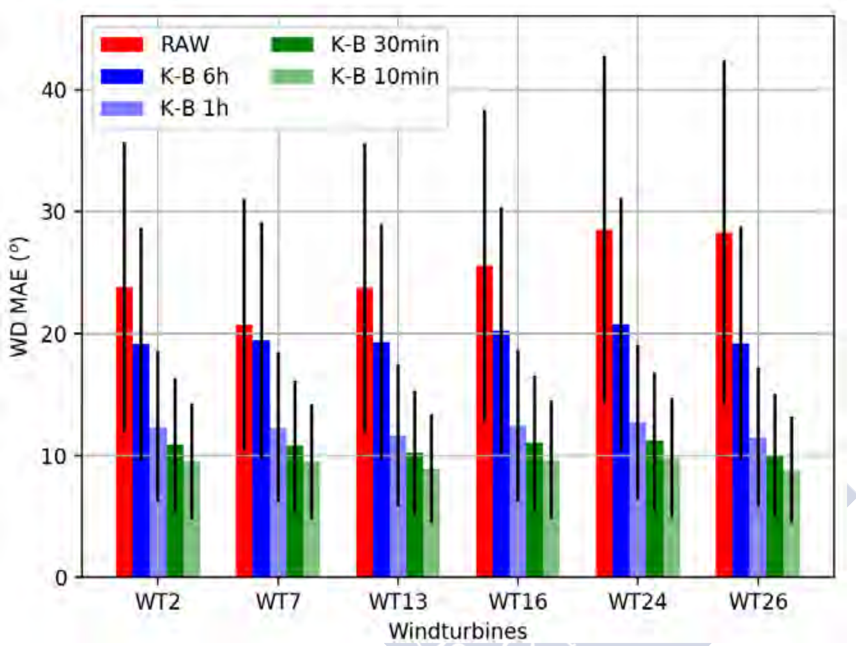

Figure 3.7: Barchart with annual WD MAE for all experiments and wind turbines analyzed. For each case, the standard deviation is represented by a black line () on the top of each bar.

The bar chart depicts in red the results of WD MAE for each RAW wind turbine. All of them are above 20°; WT7 with the lowest value, 20.69° and WT24 with the highest, 28.51°. The mean value of the MAEs for all the wind turbines in the RAW case is 25.10°. Comparing K-B 6h with the unfiltered WRF results, we can see an important amelioration in most of the wind turbines; all of them are now below or practically at 20° MAE, reducing the mean total K-B 6h MAE to 19.67°. This value translates into a 22% improvement with respect to RAW results, a correction impact that doubles that obtained in wind speed nowcasting for this same comparison (WS RAW v.s. K-B 6h). This difference can be attributed to the origin of the observational data used. In WS nowcasting we correct one output data series, with another single data series (observed wind speed). However, in WD nowcasting we use WS and WD data from sonic anemometers to obtain the U and V wind components and calculate the post-processed WD. We are thus introducing more sources of error in this last step that the K-B filter seems nevertheless capable of offsetting.

In the shorter lead times of wind direction nowcasting (K-B 1h, 30min, and 10min) the behavior presents a similarity to that of wind speed nowcasting (Figure 3.2). All the turbines attain analogous error values in each experiment, with a total mean WD MAE of 12.16°, 10.69° and 9.37° for K-B 1h, K-B 30min and K-B 10min respectively. Aside from these low errors, there is also a corresponding reduction of the standard deviation. The K-B filter at short-term nowcasting increases prediction accuracy significantly and eliminates more substantial punctual errors from the original WRF forecasting, which is quite important for the use of these kinds of combined nowcasting systems in wind farm applications. The reason lies in the fact that during daily operations of these installations, wind turbines are continually being orientated depending on wind direction, and potential errors in this manoeuvre lead to machine overstress and production decrease.

As in Section 3.1 for wind speed, the monthly errors for wind direction are shown in Figure 3.8a, and on a finer timescale, Figure 3.8b displays the mean hourly wind direction MAE, averaged for all the turbines in the farm. In both cases, RAW WRF outputs are compared with the results of the K-B experiments.

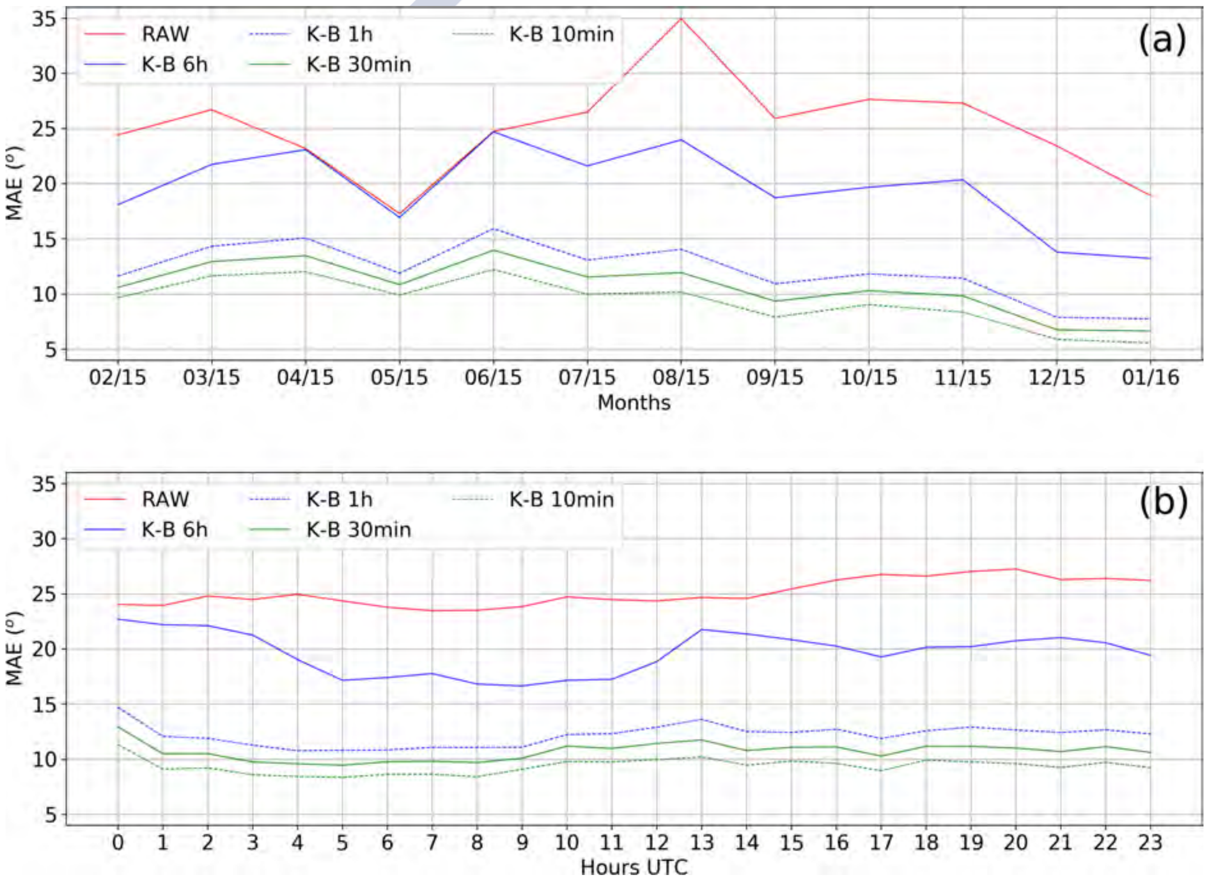

Figure 3.8: (a) Monthly wind direction MAE for the wind farm with K-B model experiments and RAW. (b) Wind speed MAE, hourly for the entire 24 h simulation period. In both cases the comparison is between RAW outputs (red) and K-B model cases: K-B 6h (blue), K-B 1h (dotted blue), K-B 30min (green) and K-B 10min (dotted green).

Monthly results in Figure 3.8a provide insights on the origin of the 22 % improvement in forecast skill of K-B 6h with respect to RAW, commented in Figure 3.7. From 02/15 to 03/15 and from 07/15 to 01/16 the effect of the K-B 6h is noticeable, with a decrease in errors of around 7.5° during those periods. Nevertheless, the scenario is entirely different in spring, when K-B 6h practically does not refine the original RAW result. This lack of improvement can be partially explained by the fact that, during spring months, the original WRF outputs register the lowest U and V errors of all the year, and, similarly to previous results, the K-B filter has more difficulties correcting RAW forecast results with low errors.

K-B 1h, 30min, and 10min follow the general tendency of the rest of the comparisons, presenting a substantial error decrease throughout the year. K-B 30min skill score is always below K-B 1h and the same for K-B 10 min with respect to K-B 30min, with all three time series showing a parallel behavior throughout the whole period. As opposed to the case of wind speed (Figure 3.4), winter months, particularly December and January, have the lowest errors of the series in all wind direction K-B results. For example, K-B 30min error is around 6.6° during these winter months, but over 12° in springtime. The lower WD MAE in winter months seems to be related with the higher mean wind speed registered during that part of the year (Table 3.3). This means that there are fewer periods of weak winds, which are associated with increased variability in wind direction, presenting, therefore, more difficulties for the K-B filter to handle.

Changing the timescale of the analysis, Figure 3.8b shows the evolution of the WD MAE throughout the day. The RAW series (red line) does not present significant hourly changes; all the values are close to 25° with a slight increase in the late hours of the day. K-B 6h differs from this homogeneity, displaying a slight daily cycle with more accurate predictions from 04 to 12 UTC, with a minimum MAE=16.64° at 09 UTC increasing to a maximum of 21.76° at 13 UTC. Same as in the daily analysis of wind speed (Figure 3.5), in the shortest nowcasting periods (1h, 30min, and 10min), the variability is practically eliminated. The K-B filter decreases errors and smooths out the series, with rather constant MAEs around 10° throughout the day. The comparisons at different time scales among all the cases confirm that the K-B filter yields a valuable improvement in wind direction prediction. The shortest term nowcasting cases, starting from K-B 1h, lead to a significant correction of WRF outputs independently of the meteorological situation of the moment.

To conclude this section, in Figure 3.9 we exemplify the capabilities of wind direction nowcasting with K-B filter. Specifically, a two-day WD MAE comparison is displayed for WT13 between RAW (red) and K-B 1h (blue). The arrows inside the circles show the instantaneous observed wind direction every four hours (black) and its respective RAW (red) and K-B 1h (blue) prediction

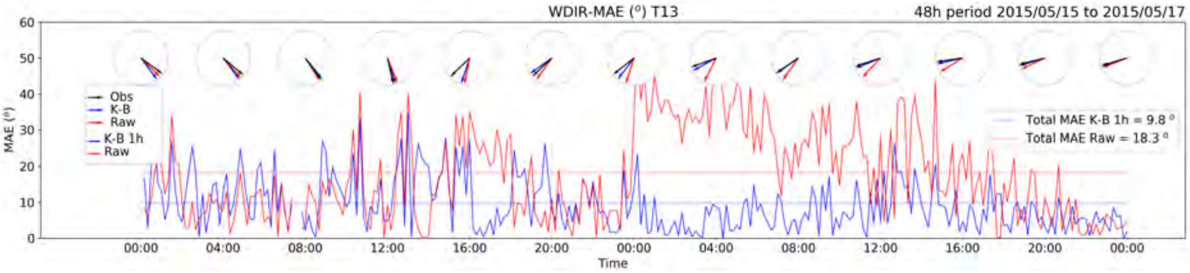

Figure 3.9: Wind direction MAE with K-B 1h filter and RAW in W13 during a 48h period. Wind direction arrows with observations, K-B 1h, and RAW are displayed on the top every four hours.

The two-day results presented, from 2015/05/15 to 2015/05/17, show different forecast skill patterns. In the first day, RAW and K-B 1h error series are close to each other in their first 12 hours. In the next hours, RAW maintains a more constant higher error (around 25°) for 3-4 hours, which K-B 1h drastically corrects. During the second day, this difference between the time series increases in magnitude; RAW predictions go over MAE = 30° for 12 hours, reaching up to 40° in different moments. Throughout all this time period the K-B correction sharply eliminates these big MAEs to values below 10°.

Given these results, we can affirm that K-B 1h provides a good skill improvement in all the situations where the original RAW forecast presents large errors. As in the case of wind speed nowcasting, the correction of big WRF wind direction biases is crucial for wind farm operation applications.

Application of the K-B filter for wind power forecasting

In this last section, we test the capabilities of K-B 1h wind direction nowcasting tool on a real scenario of Coruxeiras wind farm in the studied year, with special attention to critical issues in power prediction, such as wind ramps. For this purpose, we focus on the results corresponding to the wind turbine power ramp, which is the ascending part of the wind power curve before nominal power (Figure 3.10). Wind speeds within this curve (in this case from 4 to 13 m/s) have the most significant effect in the forecast skill of any nowcasting tool in the wind energy field. In Figure 3.10, we present the relation between the wind power curve of the wind farm's turbines (ECOTECNIA74 with 1.670 MW of nominal power [63]) and the WD MAE associated with each wind speed bin, both for RAW and K-B 1h cases. Table 3.5 displays the WD MAE in power ramp wind ranges for all the experiments and for each area of the wind farm. It also compares these results with persistence at 10min, 30min, and 1h. The persistence forecast is the assumption that the next timestep value in a prediction is going to be the same as the last measured value [107].

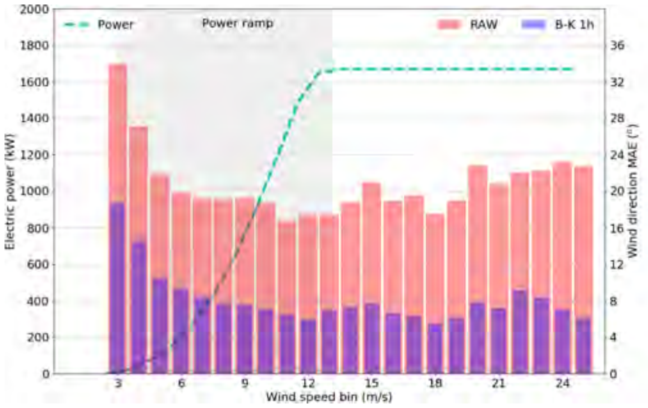

Figure 3.10: ECOTECNIA 74 wind power curve (density=1.112kg/m3, height=975m, temperature=9°C), cyan line. Each bar of the figure represents the WD MAE associated with WS bins with a bandwidth of 1m/s both for RAW (red) and K-B 1h (blue).

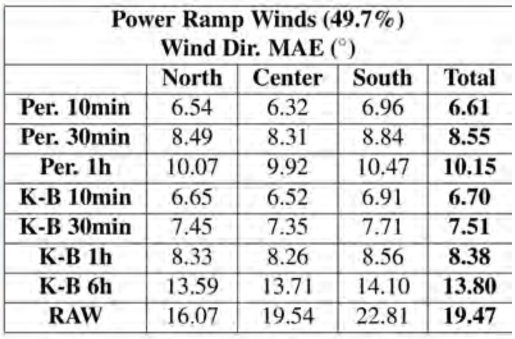

Power Ramp Winds (49.7%) Wind Dir. MAE (°)				
	North	**Center**	**South**	**Total**
Per. 10min	6.54	6.32	6.96	**6.61**
Per. 30min	8.49	8.31	8.84	**8.55**
Per. 1h	10.07	9.92	10.47	**10.15**
K-B 10min	6.65	6.52	6.91	**6.70**
K-B 30min	7.45	7.35	7.71	**7.51**
K-B 1h	8.33	8.26	8.56	**8.38**
K-B 6h	13.59	13.71	14.10	**13.80**
RAW	16.07	19.54	22.81	**19.47**

Table 3.5: WD MAE for all the experiments and different persistence periods in power ramp winds.

The error bar chart in Figure 3.10 clearly illustrates the significant improvement of K-B 1h over RAW results in power ramp winds. At the beginning of the ramp, K-B 1h obtains a 50% of improvement over RAW. This percentage increases with wind speed, reaching practically a 75% error reduction in the last part of the ramp (12-13 m/s). This is a desirable characteristic of the nowcasting tool because it results in more accurate direction predictions in wind speed situations where energy production values are higher.

Table 3.5 shows no significant differences among farm areas in power ramp wind direction MAEs. In general, all the experiments achieve better results for power ramp winds than in general for all cases (Figure 3.7). This is mainly because power ramp situations exclude lower wind occurences, associated with more variability. Moreover, K-B 1h and K-B 30min lead to better results than 1h and 30min persistence, respectively. K-B 1h also reaches lower WD MAE than 30min persistence.

A K-B nowcasting tool can be useful in the daily management of a wind farm. For instance, an operational K-B 1h can back up current orientation methods, which are based on SCADA (Supervisory Control And Data Acquisition) systems [100]. There are also new wind farm control techniques such as yaw-misalignment [108, 109], in which upstream wind turbines redirect wakes to increase the production of downstream turbines, that could also benefit from the WRF K-B filter and its capacity to nowcast wind direction with MAEs below 10° with a 1h time horizon.

Summary and conclusions

In the present work, we studied the ability of a new Kalman-Bayesian postprocessing technique to improve the wind speed and wind direction forecasts derived from high-resolution simulations for an operational wind farm over complex terrain. For the needs of the study, a period of one year is simulated utilizing the WRF atmospheric model at a 333 m horizontal resolution, and its outputs post-processed with the K-B filter. We validate the method for different short-term forecast periods, from 6 hours to 10 minutes, with in-situ real data from meteorological stations on the hub of wind turbines.

The results show that the K-B filter in the very short-term (from 1h to 10min) is capable of improving the initial wind speed forecasts of the atmospheric model significantly, although the latter are already considerably good (RAW annual WS MAE =1.87 m/s). The K-B filter achieves a decrease in the WS MAE to 1 m/s for 1h horizon nowcasting and to 0.72 m/s for the 10 min case. The ME practically disappears when using the K-B 6h. Analyzing all the experiments in different period ranges (months, hours, instants), we demonstrated that for shorter-term cases, K-B postprocessing eliminates any source of error, improving the prediction in all conditions regardless of the intensity and direction of the wind or the moment of the day and the season of the year.

The effectiveness of the hybrid filter in correcting forecasted wind directions was also a key point of the present study. This was achieved by applying the hybrid post process system to the two-dimensional field of horizontal wind speed components (U and V). The results were quite satisfactory as the K-B 6h presents a 22% of amelioration with respect to RAW forecasts. Shorter-term cases decrease their WD MAEs even below 10°, with an important degree of efficiency in any meteorological situation throughout the year.

Emphasis was also given to the behavior of wind direction K-B 1h in power ramp wind cases. The mean results for these are better than for general cases due to the filtering of low winds. K-B 1h WD improves the persistence forecast for 1h and 30min.

In general, the combination of high-resolution WRF simulations and the K-B hybrid filter has shown effectivity and reliability obtaining accurate short-term wind speed and direction predictions, which are of critical importance for an operational wind farm.


USC
UNIVERSIDADE DE SANTIAGO DE COMPOSTELA

Chapter 4

Annual Wake

Introduction

The study of the wind farm wake behavior is a standard practice within the wind energy field [110]. A wind farm wake effect can be summarized in two main physical processes, the momentum (or velocity) deficit, which causes a reduction in the power output of the downstream turbines, and the increased level of turbulence, which also gives rise to unsteady loading on them [111]. It is essential to forecast and understand the impact that the wakes are going to have in the environment before installing the machines. Specifically, it is fundamental to study the effect that a wind farm has over its own turbines (inter-turbine wake) [110].

The wake that each turbine produces around it has a direct impact on the production of the farm and also generates loads on the rest of the machines affecting their lifetime [112]. The wake effect study is not only reduced to the siting plan period, it is also essential to take into account this turbulence phenomenon in wind farm operation. There are even wind farm control techniques such as the yaw-misalignment [113, 109], in which upstream turbines redirect wakes away from downstream turbines. In this way, it is possible to avoid partial wake overlaps, which generate significant loads on downstream wind turbines [100] and increase the production of the farm.

Wake models are in continuous improvement, mainly, to design new turbines, but also to enhance siting techniques for new wind farms and correct wake interactions in existing installations [110]. Current methods of Computational Fluid Dynamics (CFD) are capable of simulating air flow fields accurately, considering the main microscale processes affecting the wind, like buoyancy or turbulence diffusion effects [25]. They can run over complex terrain using orography height values from LiDAR data [26]. They also dispose of specific wind turbine effect schemes [114] to simulate wake effects on wind farm areas and study in detail the motion responses to the aerodynamic loads on the machines. However, if we are interested in the interaction between the wind farm and the local phenomenology in a specific region, these models present some limitations. They do not readily incorporate time-varying lateral boundary data from observations or analysis and, furthermore, thermal effects on turbulence and the wind flow are generally considered constant and hence, are not realistic, as these can vary substantially throughout the day.

Within the meteorological modeling, there are some current NWP models that, at very high resolution ($<$100m), are also able to perform detailed wind microscale processes. These types of simulations are called Large Eddy Simulations (LES), and they also have explicit wind turbines parameterizations available. There are several recent studies with WRF LES simulating wind turbine wakes with high accuracy [39, 40, 41]. However, despite the constant improvements in HPC regarding time and cost, WRF LES still suppose an excessive computational cost in order to perform long-term simulations (> 1 years).

In the present time, WRF wind turbine schemes [34, 58] offer the equilibrium between the reproduction of most of the processes in the atmosphere and a realistic wake effect parametrization with an acceptable computational cost to perform long period simulations. There are many previous studies which have tested these WRF parametrizations in different locations of the world. Many of these experiments were performed over U.S. areas such as Vanderwende et al. [39], Lundquist et al. [49], Vautard et al. [50]. It is worth noting the Wind Forecasting Improvement Project 1 and 2 (WFIP2) [115]. This huge data collection experiment has been used, among other things, to develop and improve model wind turbine and physics parameterizations [116]. Another well know wind farm studied with WRF is the Rev Horns offshore wind farm [54, 56, 58]. Still, to the best of our knowledge, there are no previous works which exploit the capacities of WRF wind farm parametrizations at high resolution in long period studies.

The novelty of our study is based on the analysis of the wind farm wake in a long-term period covering the farm and its surronding. Using the WRF model and the Fitch Wind Turbine scheme [34] as primary tools, we carried out one year of high-resolution daily simulations (333 m) over an area of interest in the East of China. Obtaining high-frequency output every 10 minutes, we performed a detailed analysis of the behavior of the wake effects produced by the wind farm. To do that we ran each daily simulation with and without wind farm scheme and obtain the wind field difference between them. With this method, we can also accurately identify the loss of wind resource due to each wind turbine for any day of the year. In addition, calculating the mean wind speed percentage loss in all timesteps of the year, it is possible to obtain an estimation of the annual wind farm impact on the environment. To our knowledge, this is the first time that a thorough evaluation for such a long period of time has been performed to analyze the wind footprint of a wind farm. The rest of the chapter is organized as follows: In Section 4.2 the methodology is explained in detail, focusing on the WRF configuration and the Fitch scheme used. In Section 4.3, the main results obtained are shown, first for the Jiansgu case in China and then for Coruxeiras (same as Chapters 2 and 3). Finally, in Section 4.4 the conclusions are discussed.

Methodology

Wind farm studied and WRF configuration

The wind farm studied is located in the north part of the Chinese province of Jiangsu, on the east-central coast of China, in front of the Yellow Sea (Figure 4.1a). This region has a humid subtropical climate, and most of it presents a flat terrain. The farm lies in an extense open area close to the sea (Figure 4.1b). The wind of this location is profoundly affected by its proximity to the sea, and its prevailing directions are northeast, east, and east-southeast. Goldwind company `http://www.goldwindglobal.com/` is the developer and operator of this wind farm composed of 74 wind turbines separated by a mean distance of around 700 m for the Y turbines (East side) and about 1 km for the X turbines (West side) (Figure 4.1b).

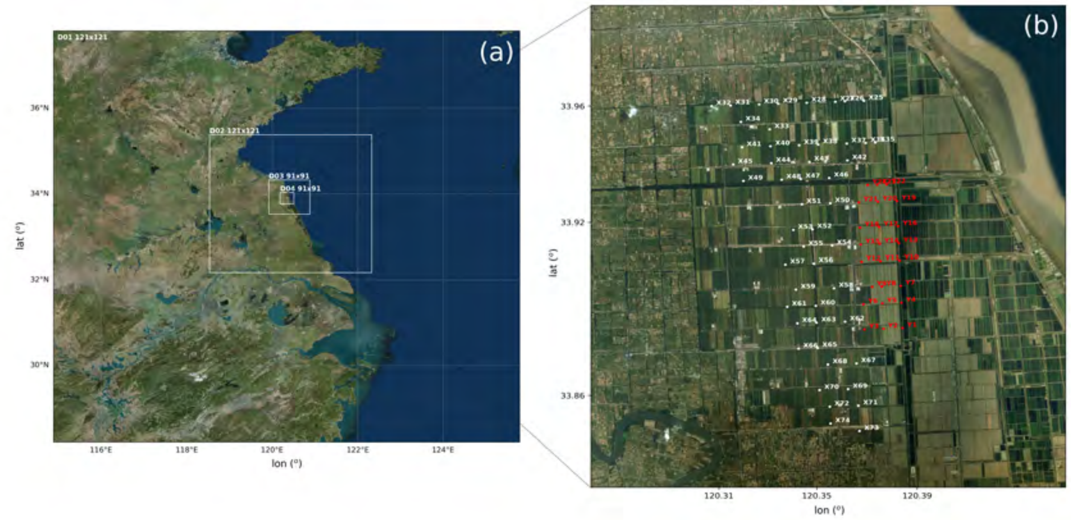

Figure 4.1: (a) Nesting domain's configuration. (b) wind turbines locations, two kinds of machines, WT1 (white) and WT2 (red).

To perform the simulations we used the Advanced Research WRF (ARW) model version WRF 3.7.1 [32]. Figure 4.1a shows the domain's configuration where D01 is centered at 33.75 N and 120.33 W (Figure 4.1a) with 121x121 grid points with 9 km of horizontal resolution. Following the configuration used in Chapter 2 and 3, the horizontal resolutions of D02, D03, and D04 are 3 km (121x121 grid points), 1 km (91x91 grid points) and 333 m (91x91 grid points) respectively. As has been commented in previous chapters, for these kinds of studies, it is fundamental to use a high vertical resolution, both for improving wind and temperature variations in the surface layer [67], and to achieve a better performance of the wind turbine parametrization [35]. In this case, D04 has 67 vertical levels with a non-linear distribution, 8 in the first 200 meters above the ground. Land use information for d04 is obtained from the ESA CCI (European Space Agency Climate Change Initiative) database [65] with a resolution of 300 m. The terrain elevation used comes from the ASTER Global Digital Elevation Map (GDEM) from USGS (United States Geological Survey)[66] with a resolution of 30 m. In the other domains, terrain and land use data are from the WRF global standard database. The next table presents the main physics parameterizations used in the highest resolution domain.

Physics	Name
Planetary Boundary Layer	Mellor–Yamada Nakanishi Niino Level 3
Microphysics	Thompson, Field, Rasmussen and Hall
Cumulus	Disabled
Shortwave Radiation	CAM Collins et al
Longwave Radiation	RRTMG (New version of RRTM)
Land Surface	Unified Noah Land Surface Model
Surface Layer	Nakanishi and Niino surface layer scheme

Table 4.1: Parameterizations for the highest resolution domain, D04.

Same as Coruxerias study (Chapter 2 and 3), the initial 6 h of each run are excluded from the forecast data series used in the analysis of the results, thus, only outputs after this spin-up time are considered.

Annual Wake measurement

As in Chapter 2, the Fitch scheme is used (WF-S hereafter) to estimate the effects of wind turbines. The WF-S represents wind turbines as momentum sinks, transferring one fraction of kinetic energy into turbulent kinetic energy (Equation 4.1) and another fraction into electricity (Equation 4.2)[35]. The MYNN 2.5 level scheme calculates the mixing resulting from the vertical wind shear induced by the momentum sink. MYNN also takes into account the effects of buoyancy and the impact of stability on the turbulent length scale.

$$\frac{\partial TKE_{ijk}}{\partial t} = \frac{0.5{N_t}^{ij}(C_p - C_t)(|V|_{ijk})\,|V|_{ijk}^3 A_{ijk}}{(z_{k+1} - z_k)} \tag{4.1}$$

$$\frac{\partial P_{ijk}}{\partial t} = \frac{0.5{N_t}^{ij} C_p(|V|_{ijk})\,|V|_{ijk}^3 A_{ijk}}{(z_{k+1} - z_k)} \tag{4.2}$$

In equations 4.1 and 4.2: i and j are the grid cell coordinates, k is the vertical level, number of turbines per square meter, Cp is the power coefficient of the wind turbine, Ct is the thrust coefficient of the wind turbine, V is the horizontal velocity vector, A is the rotor swept area and z is the height of the model level.

In the case studied, the wind farm is composed of two different kinds of turbines with different dimensions and power curves (Figure 4.2). The wind turbine scheme is capable of taking into account different types of turbines within the same simulation domain. We introduce in the running settings the characteristics of both machines (Figure 4.2). Each of them is going to have a different wake effect in the environment.

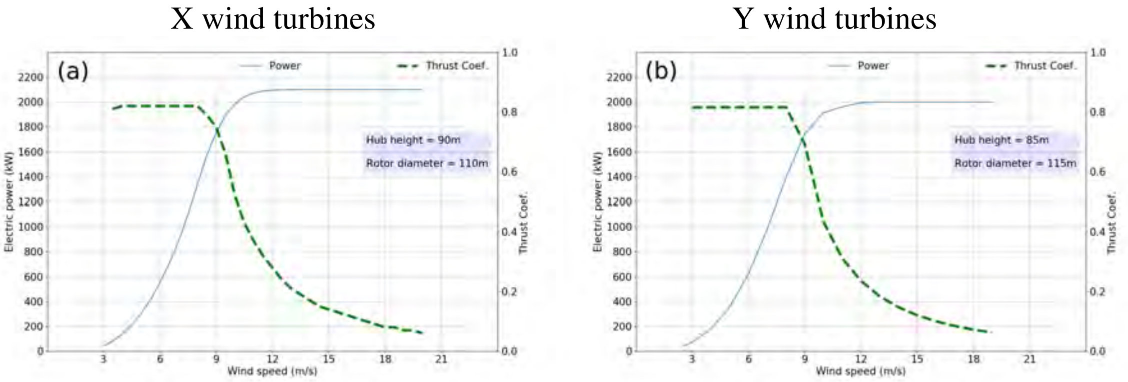

Figure 4.2: (a) X wind turbine wind power curve. (b) Y wind turbine wind power curve. In both cases, the blue line represents power and the dotted green thrust coefficient.

As shown in Chapter 2 (Figure 2.10) we can estimate the impact of wakes on the wind farm by taking the difference between simulations performed with and without wake parameterization. Similarly, in this study, we analyze the broader effect of the wind farm on its surroundings by calculating the mean wind speed percentage loss over all time steps throughout the year from the daily simulation difference between WF-S activated and WF-S deactivated experiments. The result is the mean "Annual Wake" displayed in the next section (Figure 4.6).

Initial-boundary conditions and observations

The study covers the period between 2016-05-01 and 2017-04-30. One year (2016-05-01 to 2017-04-30) of GFS analysis data from the National Center for Environmental Prediction (NCEP) is used as initial and boundary conditions, with a 3-h update interval. The horizontal resolution of this dataset for all variables is 0.25 x 0.25 deg, with 32 levels ranging from 1000 to 10 hPa. The observational data used in this work is provided by Xinjiang Goldwind Science & Technology Co. collected from anemometers located on top of each nacelle. One year ten-minute-interval wind data for three turbines are available. Each one is located in a different part of the installation, X27 in the north, X58 in the center an X68 in the southern part (Figure 4.1b). The next figure shows the annual wind rose for the three of them.

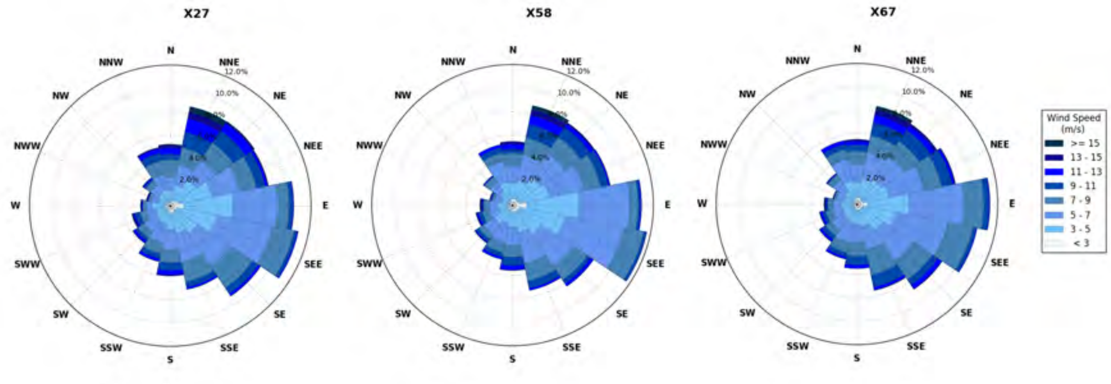

Figure 4.3: Annual wind roses from observations for the three validation WT points X27, X58, and X67 at hub height.

Results

Jiangsu Annual Wake

This section shows the Annual wake result for Jiangsu wind farm (4.3.1) and the validation of this same study using observational data introduced in the previous section (4.3.2). Apart from this, the last subsection presents the Annual Wake in Coruxeiras wind farm obtained from the results of the study presented in Chapter 2.

The main objective of this study is to estimate the mean annual wake of the farm, as is explained in the previous section. This is obtained from the mean wind difference between WRF simulations with and without WF-S across all time steps. Each of these differences per timestep also gives us the wake effect at a specific instant. The next figures show three wakes obtained at different moments during the studied period. The mean instantaneous wind speed in the area (MWS) is also presented in each image.

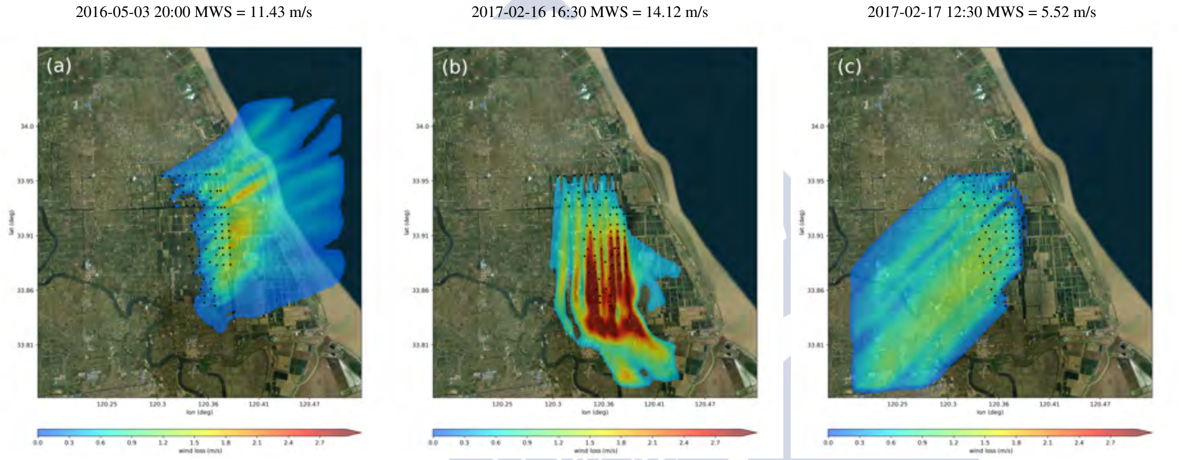
2016-05-03 20:00 MWS = 11.43 m/s

2017-02-16 16:30 MWS = 14.12 m/s

2017-02-17 12:30 MWS = 5.52 m/s

Figure 4.4: (a) Wake produced by a SW wind, (b) wake produced by a N wind, (c) wake produced by a NE wind. On the top of each image, the time instant represented and the mean WS at hub height in the area are indicated.

In Figure 4.4a we can see the wake produced due to the interaction of a southwestern wind with around 11 m/s wind speed over the wind turbines. Wind speed losses of 1.5 m/s are registered in practically all the east part of the farm. This means that at that moment, 35 wind turbines are producing around 300 kW less than the other part of the park (Figure 4.2). Figure 4.4b displays a stronger wake impact on the farm itself created by a higher wind from the north ($\approx$14 m/s). In this case, all the Y machines, and 20 of the X type are receiving wind at 10-11 m/s with a high turbulent regime. Changing the incident wind direction again, Figure 4.4c shows a resultant wake from a low wind ($\approx$5 m/s) from the northeast. What becomes evidaent is how the wake, despite being the result of low wind, extends several kilometers ($\approx$15 km), we can see how the wake even reaches the simulation domain boundary at the lower left corner.

Continuing with the qualitative study of the wakes, the next group of figures displays three examples of daily mean wake effects measured during the period studied.

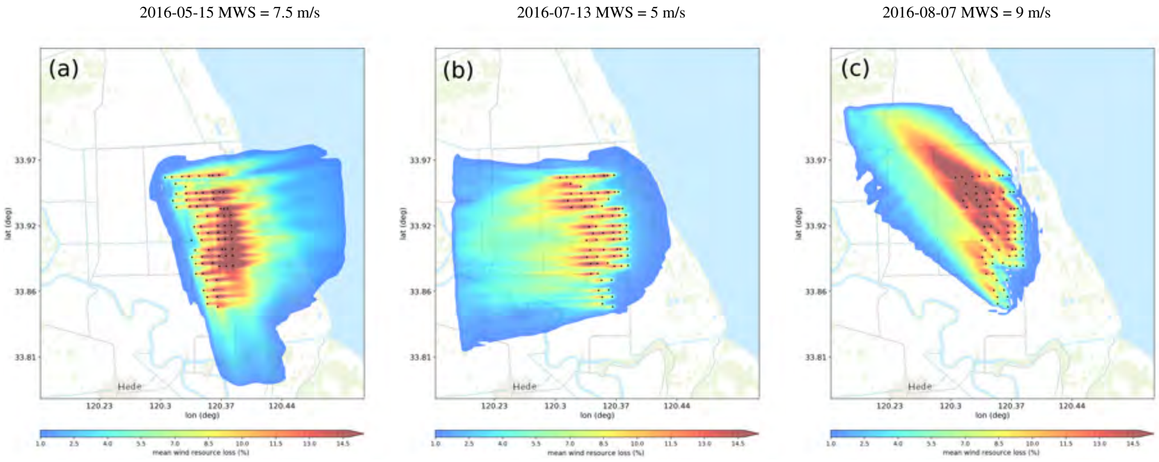

2016-05-15 MWS = 7.5 m/s

2016-07-13 MWS = 5 m/s

2016-08-07 MWS = 9 m/s

Figure 4.5: Daily mean wake effects for different days of the year (wind percentage loses). On the top of each image, the day represented, and the mean WS at hub height in the area are indicated.

Depending on the prevailing winds of the day, daily mean wakes (Figure 4.5) are drawn over a different area and affect a different part of the wind farm, the picture for the 2016-05-15 case (Figure 4.5a) is the result of a mainly western and northwestern wind. In the figure 4.5b case the mean impact is softer due to the lower mean wind module registered for that day. The wake area on the right could be caused by interaction between the wind farm and the land breeze effect. The wake in Figure 4.5c shows a clear mean prevailing southeast wind case with a higher mean wind speed which provokes significant resource losses in all the north part of the wind farm. Just the same as in Figure 4.4c, the straight shape of the wakes at the last part of their edges are due to the contact with the boundary of the simulation domain.

These pictures can be useful information in a wind farm siting project because they allow us to the see how the wake effect from each wind turbine interacts with the other neighbors' wakes and affect other areas of the installation. The two main effects over downstream wind turbines, which are wind resource loses and stress to machines, are well resolved by this technique. A turbine can produce in its nominal power range being affected by a wake effect if the wind is high enough. However, this produces a more turbulent regime, making the machine suffer extra loads which are going to have a negative impact on it in the medium and long-term.

In the same way as for the daily mean wakes, we can calculate the mean wind speed percentage loss over all the timesteps of the year, which is what we call "Annual Wake". This annual measurement is displayed in the next figure for Jiangsu wind farm.

The wind turbines of this farm have a significant separation between them, with around 800 m of mean separation distance all along the installation. Despite this configuration, the high variability of the wind direction (Figure 4.3) and flat orography of all the region (Figure 4.1) results in significant wind resource losses between wind turbines in several directions, and prolonged wake effect all around the wind farm. In figure 4.6b we can see the high percentage of wind resource loss around the wind turbines. The northern row of turbines (from X27 to X32) produce losses of over 7% 2 km away northbound. This high level of resource loss in the near environment not only has a direct effect on wind power production, but also on a machine's lifetime. Figure 4.6a shows a more general view of the wind farm impact on the surroundings. Significant wake effects are distinguished 10 km away from the installation in different directions, especially pronounced in the west area of the farm.

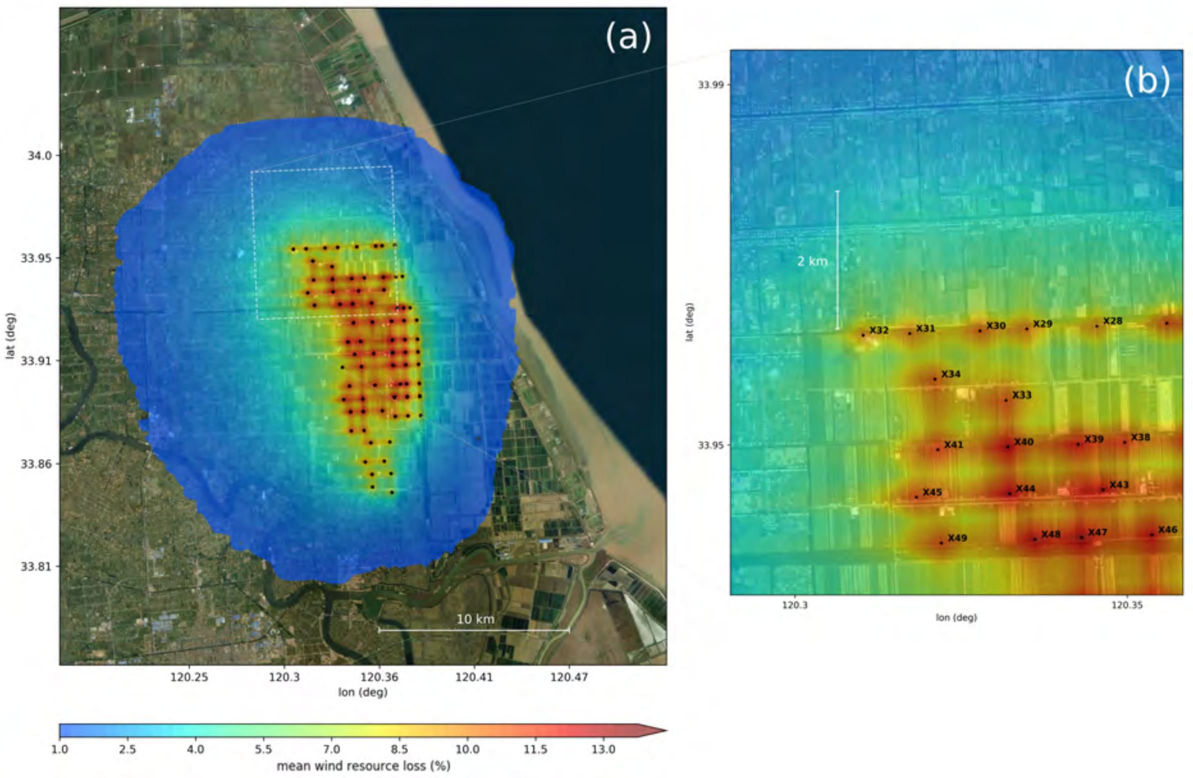

Figure 4.6: (a) Annual wind farm wake. (b) Zoom over the north of the wind farm.

Jiangsu validation

Observational data from three meteorological stations at the hub of three wind turbines is used to validate the wind output from the model used to estimate the Annual Wake. In the next table, we present some wind annual mean errors for each validation point.

	X27 (N)	X54(C)	X67(S)	Mean
ME (m/s)	0.932	0.997	0.964	0.964
CC	0.802	0.797	0.782	0.794
RMSE(m/s)	2.070	2.045	2.056	2.057
MAE(m/s)	1.592	1.565	1.580	1.579

Table 4.2: Annual wind speed ME, CC, RMSE and MAE for three different wind turbines (X27, X54, and X67).

The first thing that stands out is the similarity between the three wind turbines in all the errors measured. This is also reflected in the total mean values (right column), which are practically the same as the ones for each point. This proximity between different turbine results could be in part due to the flat terrain of the region; this characteristic makes all the wind turbines be affected to a similar degree by the wake effects from the rest of the farm. Furthermore, there is not a clear prevailing wind direction, as we can see in the wind roses (Figure 4.3) and the Annual Wake shape in Figure 4.6. The errors show a good performance of the simulations; the total MAE is 1.58 m/s which is below the same error calculated for theCoruxerias case (Chapter 2, Table 2.4, WT-HI-1D). The improvement concerning Coruxeiras seems to be related to the plain topography of this region, which makes forecasting easier without any interaction between complex terrain and wind to resolve. The total RMSE also presents a low value for the same reason. Apart from this, it is important to point out that in this case, we are using GFS analysis instead of GFS forecasting as in Coruxeiras, this has a direct effect on the quality of the simulation in all the domains. However, ME values are more significant than in the Galician case (WT-HI-1D ME= - 0.67 m/s), and with a positive value. The high-resolution simulations with WF-S for this area are overestimating the wind speed in all the region. The expected result for these kinds of simulations is an underestimation of the wind speed due to double counting of the turbulent processes as is explained in Chapter 2. This indicates that the error source can be related to the performance of the coarser resolution phenomena in the other domains. Similar overestimation in the wind for this region of China has been recorded in a Chinese 3km-grid WRF-RTFDDA forecasting system [117] where they attribute this bias to weak wind situations, especially in summer.

To illustrate the day-to-day results of the WRF forecasting tool in terms of wind speed at hub height, we show the next comparison plots between model results and observations at hub height. Specifically, the following plots show the results throughout November for the three validation points tested.

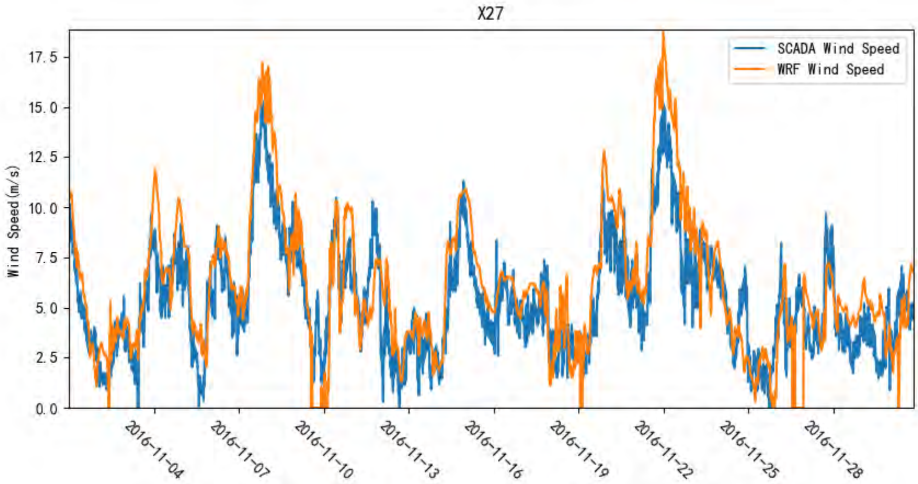

Figure 4.7: November wind speed at X27 hub height for WRF simulations (orange) and observations (blue).

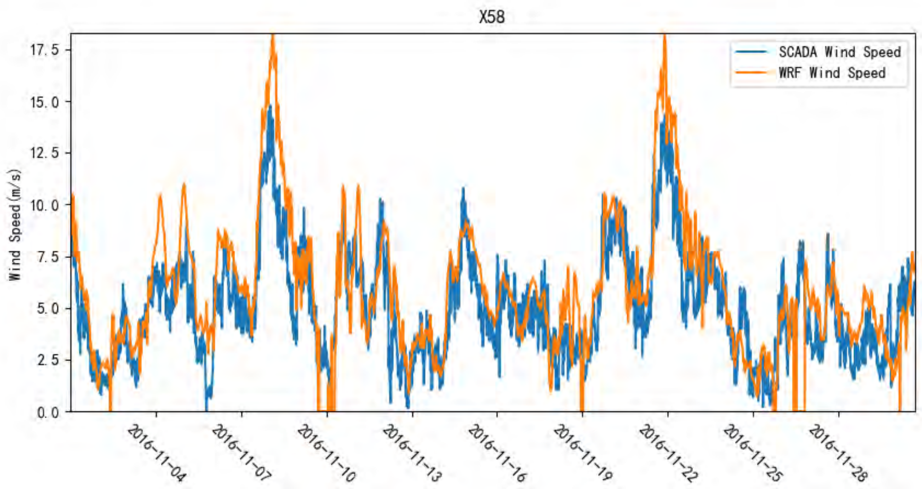

Figure 4.8: November wind speed at X58 hub height for WRF simulations (orange) and observations (blue).

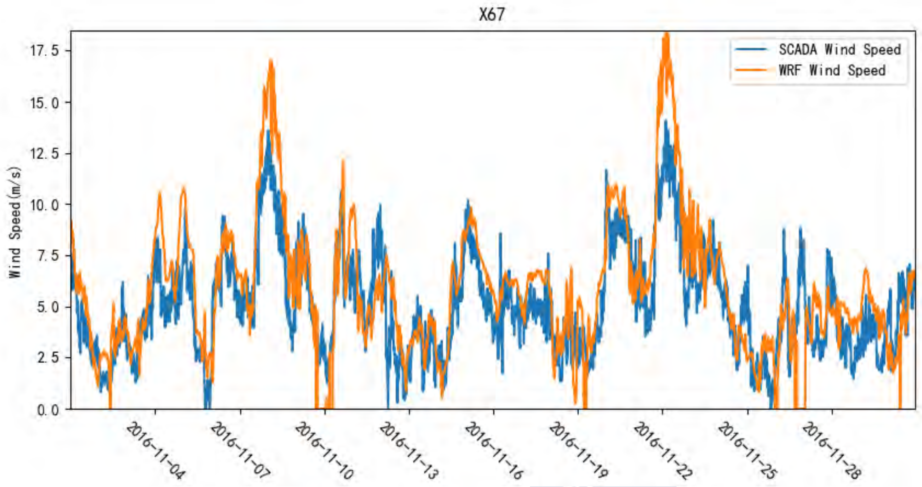

Figure 4.9: November wind speed at X67 hub height for WRF simulations (orange) and observations (blue).

Apart from a few large punctual errors (e.g., 08-11-2016 or 22-11-2016), the wind forecast presents a good tendency in all the cases. As it is expected from mean errors in Table 2.2, the performance of the prediction is very similar in all the cases. The three of them have a good correlation across the whole period represented, which also concords well with the mean correlation values shown in Table 2.2, reaching a total mean value of CC = 0.79.

Annual Wake Coruxeiras

To finish with the presentation of results, in this subsection, we show the Annual Wake measurement for the Coruxeiras wind farm (Chapter 2), which lies in a densely exploited complex terrain region in Galicia. Just as in the Jiangsu case, a period of one year broken into 365 daily runnings is simulated at 333 m, in this case with a daily operational forecasting set-up, using GFS 0.25 Forecasting instead of the GFS 0.25 Analysis employed in Jiangsu. With the same technique as in 4.3.1., we estimate the Annual Wake for this wind farm.

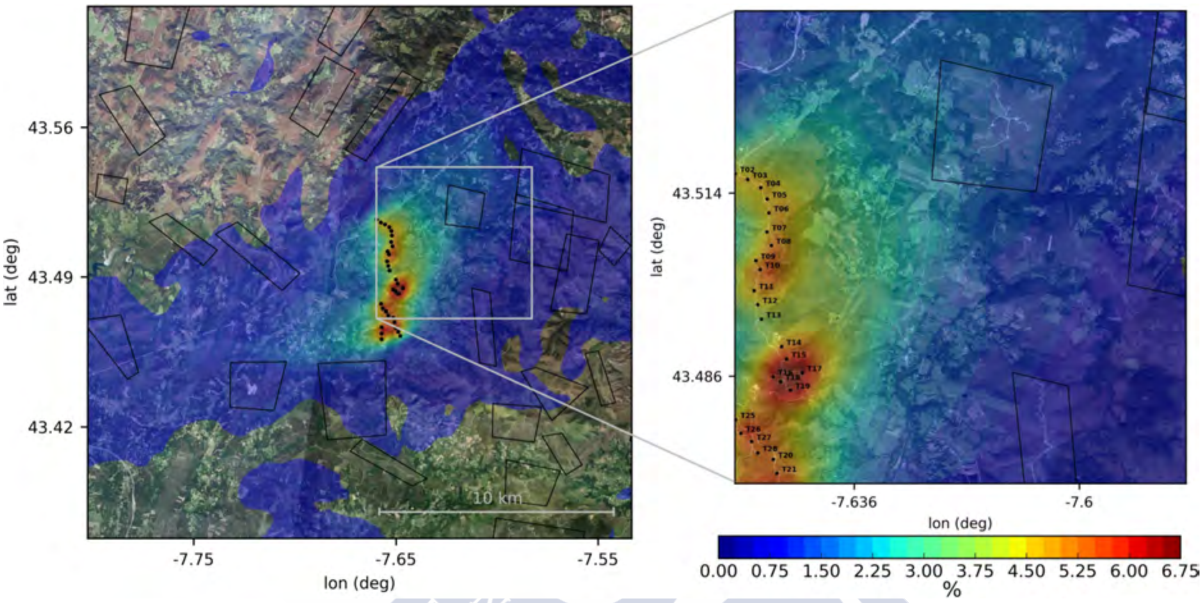

Figure 4.10: (a) Annual wind farm wake, represented in wind speed loss percentage. Other wind farm locations in the area are outlined in black squares. (b) Zoom of the NE of the installation. The wind farm marked on top suffers about a 2.25 % annual resource loss due to the presence of the Coruxeiras wind farm.

The figure shows the significant disturbance that the wind farm produces on the area. Despite the attenuation of the effect caused by the complex terrain, considerable wind resource losses extend for several kilometers, with a pattern corresponding to the wind roses shown in Chapter 2 (Figure 2.7). The wake induces losses of around 0.5 % even at 17 km from the wind farm in the southwest-northeast axis corresponding to the prevailing winds in the area. The considered farm is also significantly affected by its own wake, especially with northerly winds. The central section is the most impacted, with a mean annual decrease in wind speed exceeding 6 %. The high wind resource in the area is intensively exploited by dozens of wind farms, outlined in black in Figure 4.10. From the estimated annual wake, it is apparent that the Coruxeiras wind farm affects others nearby. In turn, the combined wakes of neighboring farms likely decrease observed wind speeds in the location of study as well. Wake effects like those shown in Figure 4.10 would represent significant economic losses and should be taken into account in any initial wind farm plan. For this purpose, the modeling tool that we present in this study can be very useful, not just for exploitation planning, but also to assess the impacts of wind turbines on the environment.

Conclusions

The objective of this study is to calculate the mean annual wake or mean annual wind resource loss in the area due to wake disturbances originating from a wind farm in the Chinese province of Jiangsu. One year of high-resolution WRF with and without the Fitch wind turbine scheme are performed in order to estimate the Annual Wake. Observational data from three different wind turbines are used to validate the wind model results. Furthermore, the Annual wake calculation for the Coruxeiras wind farm (Chapter 2) is also presented.

A measure of the instant wakes can be obtained from the difference between WRF with and without WF-S each timestep. These visual representations help to understand the effects over downstream wind turbines as wind resource losses and stress to machines, both well resolved by this model configuration. It can be interesting to correlate these visual wind results with the same ones for other variables to detect possible dangerous points for a turbine such as, for example, and specific area with high mean wind speed and a significant associated TKE. In the Jiangsu wind farm, despite the spread location of the turbines, the Annual Wake shows considerable wind resource losses among wind turbines in several directions and prolonged wake effects all around the wind farm. The percentage of wind resource loss is very high in the first kilometres away from the machines, reaching, for example, up to 7 % 2 km away northbound. In a more general view, The plain orography of the area allows significant wake effects to maintain themselves at large distances from the farm. Specifically, over 15 km away in different directions aas registered, especially pronounced in the west area of the farm.

The validation presents a small MAE at the three observation points (MAE 1.6 m/s) practically without differences among them. This improvement with respect to the Coruxerias case is mainly due to the flat terrain where the farm is, and the global model analysis data used instead of the forecasting one used in the simulations for the Galician wind farm. The overestimation in the wind ME indicates that the error source can be related to the performance of the coarser resolution phenomena in the other domains. However, a more detailed analysis should be done to confirm this affirmation.

In the Coruxeiras case, the Annual Wake length in complex terrain achieves longer distances than was expected. The environmental footprint extends for several kilometers in the southwest-northeast direction of the prevailing winds, with resource losses of 0.5% even at 17km from the turbines. This result suggests that the combined effect of the dozens of farms existing in the region could be considerable and that the disturbance of neighboring farms is likely causing a significant impact on power production. It would be interesting to carry out a thorough study of the effects of the wind farm cluster on the environment using WF-S and taking into account all the wind farms (Figure 4.10, black squares).

Despite not reaching the scale of small eddies, the model resolution used in this study seems to be more than enough to resolve the majority of the most important processes related to wind farm and planetary boundary interaction. In view of the results, we conclude that this tool can be very useful in the wind energy industry. For instance, it can analyze beforehand the total impact of a future neighbor wind farm construction on an existent wind farm's annual production. It can also provide valuable information to optimize farm designs, increasing the production and lifespan of the machines.

Chapter 5

Extreme events study

Introduction

The Isthmus of Tehuantepec, in the Mexican state of Oaxaca, is the narrowest stretch of land separating the Gulf of Mexico from the Pacific Ocean. The Sierra Madre mountains cross the isthmus from east to west, leaving, however, a pronounced gap in the middle (Chivela Pass), coinciding with the point of shortest distance between the two sea masses, of only 200 km. The elevation of the Chivela pass is 224 m, whereas mountain peaks on the side sierras reach 2000 m, creating ideal conditions to generate a powerful wind corridor [181]. In winter, cold high-pressure systems originating in North America move over the Gulf of Mexico in the wake of south-reaching cold fronts, and large pressure differences develop across the isthmus between the bay of Campeche and the Gulf of Tehuantepec, on the Pacific side. This pressure gradient results in a northerly flow situation, in which the wind is accelerated southward by cold air damming, traveling through Chivela Pass to finally blow violently outward into the Pacific Ocean. In the Gulf of Tehuantepec, the strong sea surface wind stress generates intense upwelling and vertical mixing in the upper ocean [179]. These powerful mountain gap winds are called Tehuantepecers or Tehuanos, and have been the focus of several previous studies [182, 183, 180] detailing the general setting, drivers and dynamics [185] of strong wind situations in the isthmus. The largest number of these events tend to occur in December, with a mean duration of 48h [182].

Little knowledge exists, however, on the fine-scale structure of the Tehuantepecer flow, which is prone to result in downslope windstorms (DSWS hereafter) potentially producing severe turbulent phenomena such as rotors and hydraulic jumps [155, 156] on the Pacific side of the isthmus, to the lee of local orography, particularly during the cold season. There is evidence from observations and earlier numerical studies [185] that the low elevation topography of Chivela pass can excite mountain waves, and also that these are not only restricted to the pass itself but extend into the much higher mountain crests to the west and especially to the east, as the cold air pool is often thick enough to surpass them. The ability to understand and forecast these events is very relevant, since the Isthmus has been an important development site for wind farms since the 2000's [149]. Currently this region allocates 76.8 % of the wind power capacity installed in Mexico, with approximately 2360 MW [148], which is expected to double to 5076 MW by 2020 (`https://www.amdee.org/mapas-eolicos`). In addition, several accidents related to the strong winds are reported by the Oaxacas Civil Protection Commission [140, 141, 142, 143] every year during some Tehuano occurrences.

The main goal of the present work is to study the variability of flow behavior in Tehuano wind episodes across the isthmus of Tehuantepec, depending on topographic barrier height and thermodynamic conditions of the air mass, using high-resolution simulations with the Weather Research and Forecast (WRF) model. Many studies have successfully employed WRF to analyze this kind of mountain-flow events in other parts of the world. In the US, for example, Pokharel et al. [77] study a DSWS and hydraulic jumps to the lee of the Medicine Bow Mountains in southeast Wyoming. Another DSWS in this same area is also investigated by Grubišić et al. [159] with WRF. Cao and Fovell [165] uses high-resolution (660m) simulations to study a DSWS in San Diego County related to Santa Ana winds. Apart from North America, Pokharel et al. [160] analyzes downslope wind events in North Africa with WRF and relate them with the Froude number calculated at the top of the mountain. Prtenjak and Belusic [163] examine in detail the hydraulic jump structure formed in the Croatian coast due to a Bora wind. A similar study on hydraulic jumps, in this case in China is presented in Jung-Hoon and Chung [162]. Another region where lee waves have significant relevance is Iceland. In Ágústsson and Ólafsson [161] a strong lee wave event registered by a plane is well resolved with WRF at 1km resolution over the west of this country. On the other side of the planet, Priestley et al. [164] shows the importance of high resolution in WRF to resolve accurately Föhn winds in the Antarctic Peninsula. To the best of our knowledge, there is not any previous work that studies in detail lee wave phenomena in the Mexican state of Oaxaca.

The high-resolution WRF simulations employed in the present study allow us to obtain a more complete knowledge of these events, from the synoptic scale to the microscale, focusing on the downslope winds and the hydraulic jumps that develop along the Chivela pass and the neighboring mountain ranges. The rest of the chapter is organized as follows: in section II the methodology is explained in detail, from the climatology of the region to the model configuration. In section III, the primary results obtained are shown, divided by the synoptic-mesoscale situation, the upstream-downstream structure of the phenomena and the microscale situation. Finally, in section IV the conclusions reached are discussed.

Methodology

Relation between the Froude number and mountain wave phenomena

Hydraulic jumps (HJ) are turbulent mountain-wave events generally originating downstream of a hill with lee wave activity aloft. HJs are characterized by a strong vertical wind at the end of the lee slope of the hill, accompanied by rotors with negative horizontal vorticity up front and to their rear [157]. These events are caused by a flow regime with wave amplitudes sufficiently large to result in flow separation at the topographic obstacle and strong recirculation in the near-surface flow downstream [156]. The intensity and duration of HJs have a direct dependency on the existing stable layer upstream.

If we simplified the problem as a two-dimensional steady flow, HJs can be considered the result of a transition from supercritical to subcritical flow or vice-versa [155]. If the flow shifts abruptly from a subcritical to a supercritical state, it accelerates down the slope generating a jump at its end. On the other hand, a supercritical flow can change to subcritical when affected by surface friction. This makes the flow thinner, and if the conversion is quick, it can also cause a HJ. Under the two dimensional simplification, it is possible to guess the state of the flow downstream of a topographic barrier by calculating the Froude number (Fr) (Equation (1)) upstream [158]:

$$Fr = \frac{U}{NH} \tag{5.1}$$

$$N = \sqrt{\frac{g}{\theta_0}\frac{d\theta}{dz}} \tag{5.2}$$

with g the acceleration of gravity, $d\theta/dt$, the potential temperature gradient in the stable layer, and θ_i, the potential temperature at the base of this layer. In subcritical cases, $Fr < 1$, whereas in supercritical cases $Fr > 1$. $Fr = 1$ is the critical value between the two states.

The flow dynamics related to a HJ in the atmosphere is complex [175], and there are different Fr calculations that take into account further factors [158, 156, 151] . However, due to the wind flow type for the period studied, a steady blowing due south, Fr in (Eq3) can be considered a good indicator of the flow characteristics over the considered area, especially in HJ cases.

WRF configuration

We use the Advanced Research WRF (ARW) model [101] version 3.9 (WRFV3.9) to perform the simulations. Based on a fully compressible and non-hydrostatic dynamic core, WRFV3.9 is a limited-area mesoscale and microscale model, with a terrain-following hydrostatic-pressure vertical coordinate, designed for operational forecasting, as well as research. For the experiments, we employ a nested domain configuration, in order to achieve sufficiently high resolution in the innermost grids to capture the small scale structure of the flow, while reproducing the synoptic phenomenology conducive to local DSWS in the parent one (Figure 5.1a).

The domain's configuration meets the requirements recommended by Warner [64], including a parent (d01) and four nested grids (d02, d03, d04 and d05) (Figure 5.1a-b) one-way interacting. D01 is centered at 17.91 N and 93.44 W (Figure 5.2c) with 80 x 80 grid points of 36 km of horizontal resolution. The horizontal resolutions of d02, d03, d04, and d05 are: 12 km (91x91 grid points), 4 km (94x94 grid points), 1.3 km (103x103 grid points), and 444 m (106x106 grid points) respectively. D03 covers the whole isthmus area, with Chivela pass approximately in its center, while the highest resolution domains d04 and d05 are slightly displaced to the south and east. D04 includes Chivela pass and the section of the Sierra Madre de Chiapas range east of it, with heights reaching about 2000 m. For its part, the finest grid D05 encompasses the southernmost hills to the east of Chivela pass and the coastal plain at their base. This domain configuration focuses the area of interest of the study on the Pacific side of the Tehuano wind path, including the exit of the mountain gap and the gradually rising mountains east of it, around the only two available observational sites for validation, labeled as MET1 and MET2 in Figure 5.1b.

All the domains have 70 hybrid-sigma vertical levels, 8 of which lie within the first 200 m above ground, at about 16, 46, 71, 96, 122, 147, 173 and 198 m height. The hybrid sigma-pressure vertical coordinate follows the terrain near the surface and gradually transitions to constant pressure at higher levels. The benefit of this vertical coordinate system is a numerical noise reduction in the upper-layers over mountains [168]. We maintain this fine vertical grid spacing in all the domains, to capture as wide a range of motions as possible over the depth

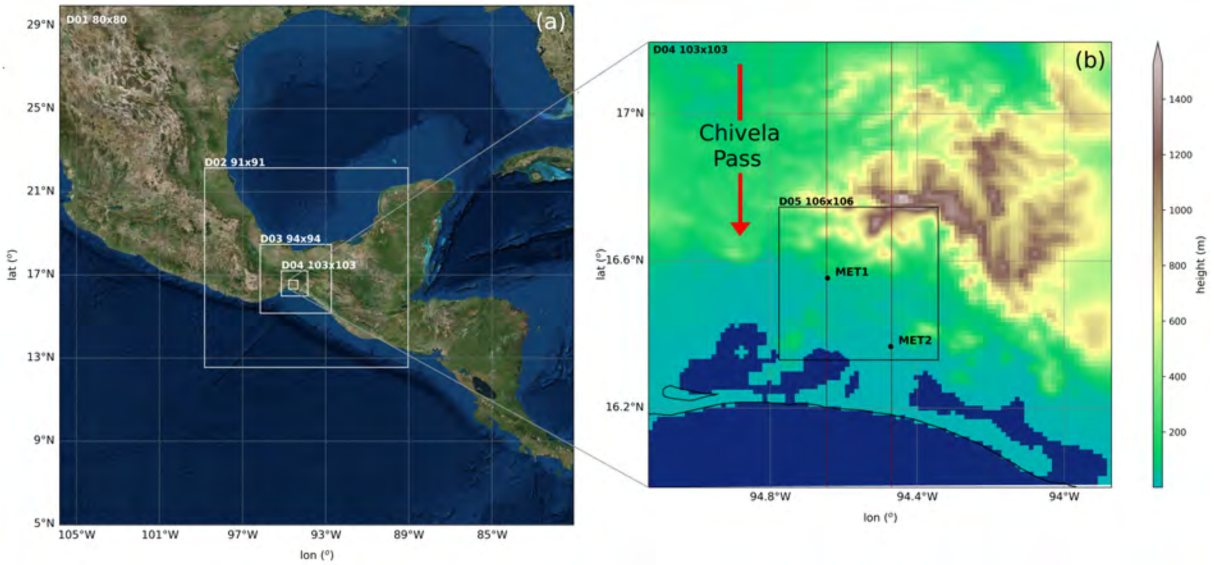

Figure 5.1: WRF nested domain configuration. (a) Coarser three domains with their number of grid points. (b) Higher resolution domains (d04 and d05), both with their respective topographies. MET1 and MET2 are the locations of the meteorological stations used as validation points. The two red lines represent the vertical cross-sections shown in Figures 5.5 and 5.7.

of the boundary layer. Land use information for d04 and d05 is obtained from the ESA CCI (European Space Agency Climate Change Initiative) database [170] with a resolution of 300 m. The terrain elevation used comes from the ASTER Global Digital Elevation Map (GDEM) from USGS (United States Geological Survey)[200] with a resolution of 30 m. In the other domains, terrain and land use data are from the WRF global standard database, both at 30” resolution for d03 and 2’ for d02 and d01.

We simulate a 36-hour period, from 2013-12-23 12:00 to 2013-12-25 00:00 UTC, which has registered DSWS conditions in the observation data. Regarding the main physics options, the simulations use the tropical suite configuration (Table 5.1), introduced in WRF version 3.9., except for the planetary boundary layer, which is parametrized by the Shin-Hong scale-aware scheme (S-H) [171]. The next table summarizes this physics configuration used.

Microphysics	Hong and Lim [70]
Cumulus	Zhang and Wang. [172] ∗disabled in d04 and d05
Long wave radiation	RRTMG [173]
Short wave radiation	RRTMG [173]
Planet boundary layer	Shin and Hong [171]
Surface layer option	Revised MM5 surface layer [144]
Land-surface physics	Noah land-surface [174]

Table 5.1: Main physic parameterizations used.

The S-H planetary boundary layer option is more suitable for the high resolution of the innermost domain (444 m) because it helps to mitigate a double counting effect of the small-scale processes in gray-zone resolutions. Apart from this, this scheme provides a turbulent kinetic energy (TKE) diagnostic variable useful for our analyses.

Global model and real data

Global Forecast System (GFS) analysis data from the National Centers for Environmental Prediction (NCEP) is used as initial and boundary conditions for the WRF model, with a 3-h update interval. The horizontal resolution of this dataset for all variables is 0.5 x 0.5 deg, with 32 vertical levels ranging from 1000 to 10 hPa. The observational data used in this work is provided by the Mexican National Laboratory of remote sensors (`https://clima.inifap.gob.mx/lnmysr/Estaciones/MapaEstaciones`), collected every 15 minutes at two meteorological stations whose location is presented in Table 5.2 and marked in Figure 5.1b as MET1 and MET2. Wind speed, wind direction, and temperature at 3 m height from these points are used for validation.

	name	latitude (°)	longitude (°)	elevation (m)	height (m)
MET1	Santiago Niltepec	16.5535	-94.6439	65	3
MET2	Ixhuatan	16.3673	-94.4717	18	3

Table 5.2: Weather station positions

Model data are extrapolated from their native sigma levels to the height of the meteorological station using Equation (3), which relates the wind speed with the friction wind speed, which is also a diagnostic variable in the model.

$$ws_z = \frac{ws_*}{K} ln(\frac{z}{z_0}) \tag{5.3}$$

Where ws_* in the friction velocity, K is the von Kármán constant, z is the height and z_0 is the rugosity.

Results and discussion

Synoptic and mesoscale situation

Figure 5.2 shows the synoptic situation, from GFS analysis data, in North and Central America 18 hours before (a) and at the end of the period of study (b).

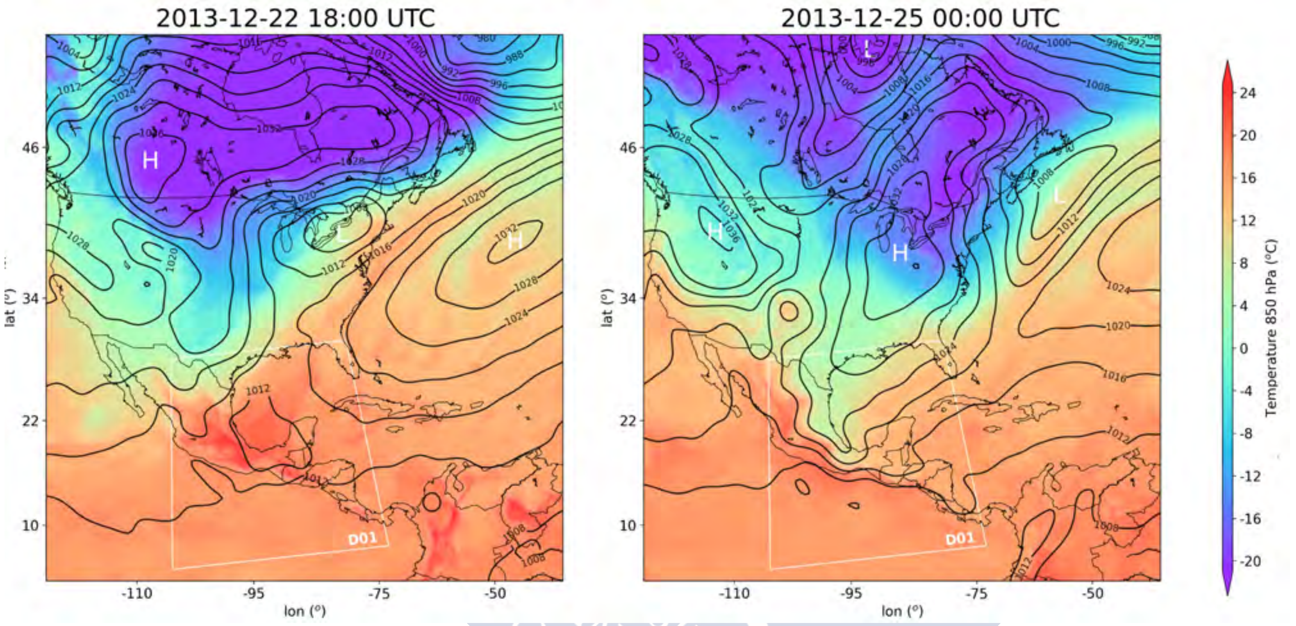

Figure 5.2: (a) Temperature 850 hPa and sea level pressure from GFS 0.5 Analysis data at 2013-12-22 18:00 UTC. (b) Same as (a) at 2013-12-25 00:00 UTC. D01 simulation domain is represented with a white square in both cases.

The large-scale setting is typical of Tehuantepecer wind episodes, where an Arctic air mass east of the Rockies pushes south across the Great Plains, with its leading edge reaching first the Gulf of Mexico (on December 22, Fig 5.2a) and then as far south as the bay of Campeche (one day later, Fig 5.2b), the result of cold air damming east of the Sierra Madre Oriental range in Mexico. The equatorward displacement of the associated high-pressure system on the wake of the cold front creates a strong pressure gradient across the Isthmus of Tehuantepec, ultimately producing the strong mountain gap winds through the low elevation of Chivela pass. The general situation favouring Tehuantepecer winds persists for about 6 days; more pronounced earlier on.

Figure 5.3 shows the mesoscale conditions of the fully developed extreme wind episode at 03:00 UTC of 2013-12-24, from the WRF simulation. In the coarser grid D01 (36 km spacing, outlined in white in Figure 5.2) the cold air damming by the Sierra Madre Oriental mountains is clearly apparent, with the northerly cool air mass intrusion extending to the bay of Campeche, from where it is funneled across the Isthmus of Tehuantepec (Figure 5.3a). The higher resolution of the nested grids shows in greater detail the structure of the gap winds.

Figure 5.3b, from the first nest D02 (12 km grid spacing), depicts the wind field (arrows) highlighting in shades the values above 10 m/s at about 70 m above the surface (sigma level 3), the approximate height of wind turbine hubs. The strong Tehuano outflow from Chivela pass reaches velocities of 25 m/s extending more than 100 km into the Pacific Ocean. High wind speeds are not only restricted to the mountain gap itself; the simulation results suggest that they also occur in the mountains west and especially east of Chivela pass. The potential temperature field on the same sigma=3 level at the enhanced resolution (4km) of the next nested grid D03 (Figure 5.3c) illustrates how the stable cold air mass to the north surmounts the lower hills neighboring the pass, particularly those to the east where elevation increases more gradually. Acceleration on the top of these mountains and to their lee is thus likely related to flow thinning and wave development, which can potentially result in strong downslope winds, rotors and hydraulic jumps. The model sounding in at the NW of Chivela Pass (Figure 5.3d, NP), shows the depth of the cold air pool, defined by the inversion existent at about 800hPa or 2500m in the temperature profile, indeed above the aforementioned mountain tops. The inversion associated to the subsidence within the high pressure system aloft is also clearly apparent just below 500hPa. Above this level, winds are weak and veer from being southeasterly to southwesterly in the upper troposphere. Below 500 hPa, winds back from an easterly to a northeasterly direction at about 800hPa, and more strongly in lower levels, becoming westerly at the surface, indicating intense cold air advection. There is a pronounced reverse wind shear in the lower troposphere.

As mentioned earlier, the only available observations in the area are from stations MET1 and MET2, whose position is marked in Figure 5.3c. They are both located on the Pacific coastal plain, south of the mountains bordering Chivela pass to the east; MET1 closer to the relief and further west than MET2. The wind speed time series covering the entire Tehuano episode for both stations is shown in Figure 5.4. Wind speeds are low in the previous days and show a daily cycle, likely linked to sea breezes, more clearly evident in station MET2 closer to the coast. The situation changes after about December 23 at 6 UTC, when picking up intensity, wind speeds become more constant throughout the day, the signature of a Tehuano wind occurrence. At about 0 UTC on the 29^{th}, the episode decays and winds go back to local breeze regimes. The extent of the simulated period covers the first 36h of the event (shaded in Figure 5.4), corresponding with its highest intensity in both locations. These observations away from Chivela pass show evidence, as the simulations suggest, that the neighboring mountains may also induce strong winds, even though certainly not as far reaching as the mountain gap does.

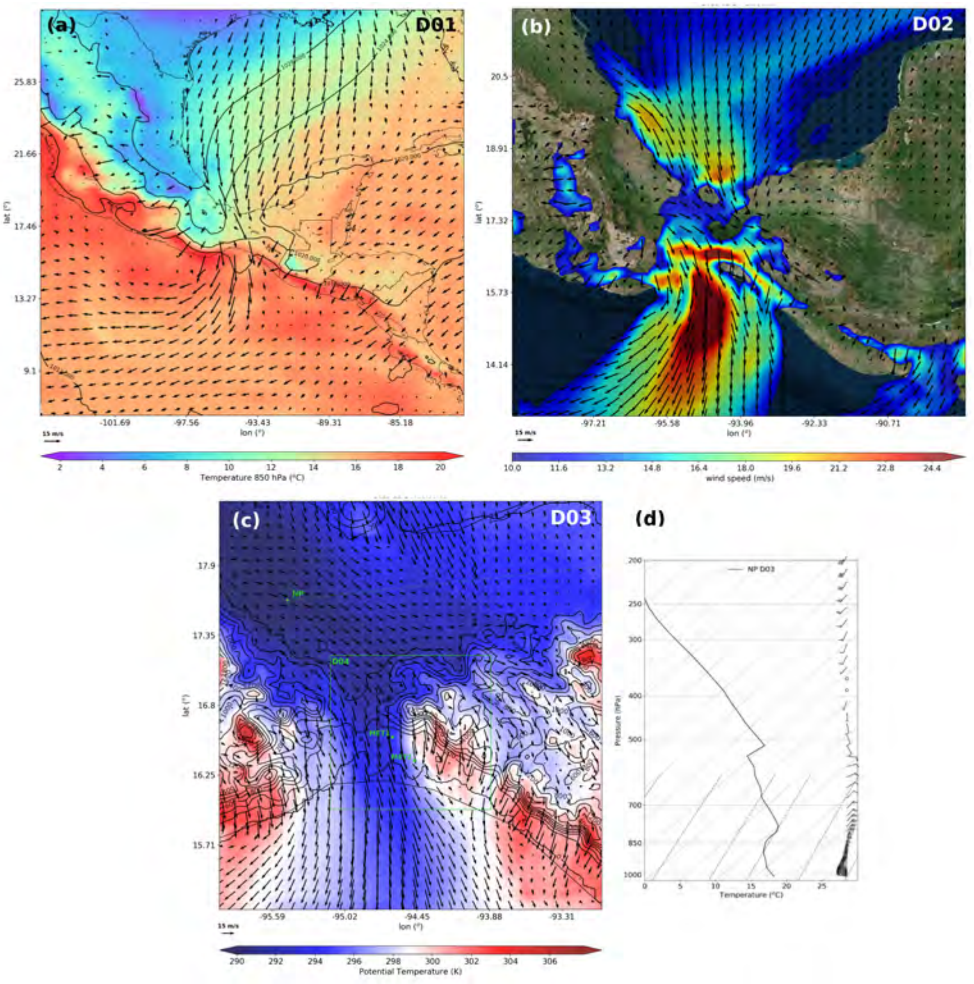

Figure 5.3: 2013-12-24 03:00 UTC (a) 850 hPa temperature, sea level pressure and wind arrows in the parent grid d01, (b) wind speed (values>10 m/s) and wind arrows at σ=3 (about 70m above ground) in d02, and (c) topography (contours) and potential temperature (shades) and wind arrows at σ=3 in d03. (d) Temperature sounding in the northeast Chivela Pass (NP point in (c)).

Upstream-Downstream structure

Figure 5.3 in the previous section shows the general structure of the Tehuano wind event, produced by the cold air intrusion from the north and orographic forcings at different scales. In this section, we focus on the fine scale structure of the flow acceleration across the Isthmus, and more precisely, on that occurring on the westernmost section of the Sierra Madre de Chiapas mountains bordering Chivela Pass, apart from the well-known strong gap wind jet. This is the area covered by the d04 domain of 1.3 km resolution (highlighted in green in Figure 5.3c), encompassing with 137 km from north to south the wind flow path before and after crossing the mountains. Figure 5.5 depicts from d04, latitudinal cross-sections (red lines in Figure 5.1b) facing east (south to the left, north to the right) of different variables at the longitude of the two validation points MET1 (Figure 5.5a-c 5.5g-i) and MET2 (Figure 5.5d-f 5.5j-l).

The tight isentropes on the windward side of the mountains (to the right in Figure 5.5a

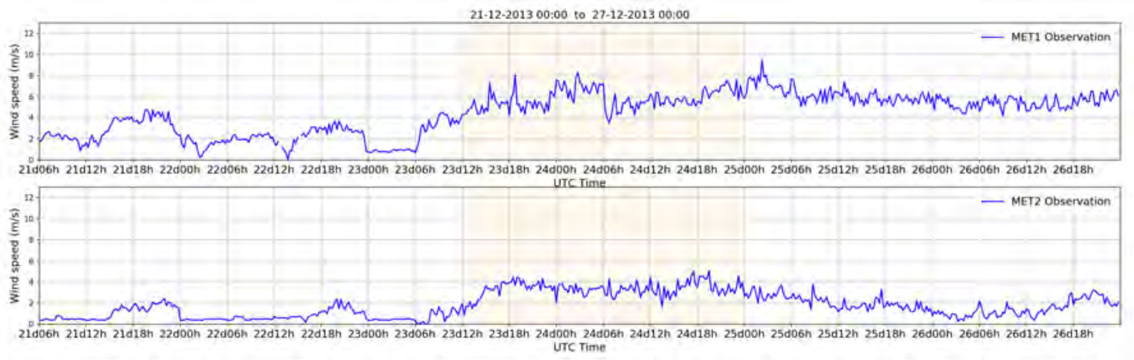

Figure 5.4: Observational wind speed time series from 2013-12-21 to 2013-12-31 in MET1 and MET2.

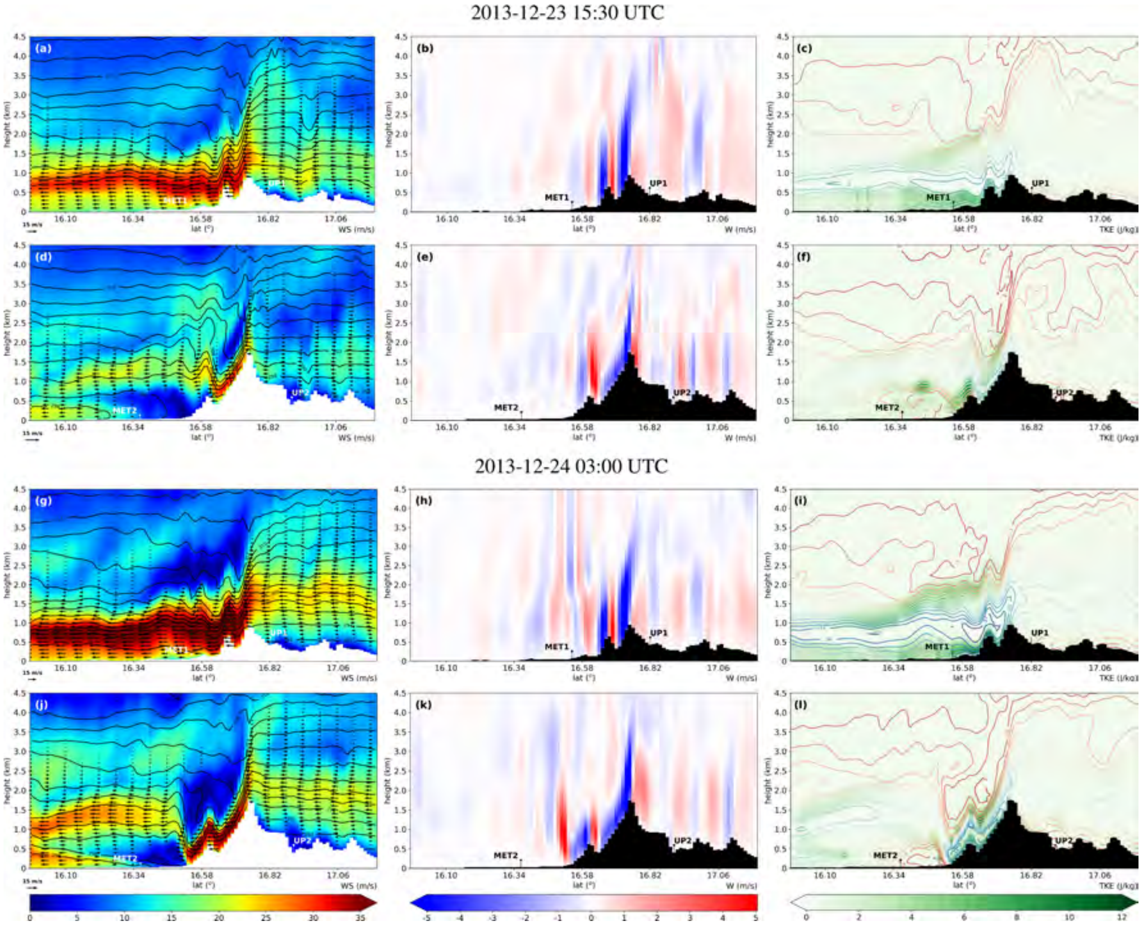

Figure 5.5: D04 vertical cross sections on 2013-12-23 15:30 UTC at MET1 of (a) potential temperature (contours), wind speed (shades), and wind arrows, (b) vertical wind component W and (c) V wind component isolines (positive in blue and negative in red) and turbulent kinetic energy (TKE, shades). (d-f) Same representations for cross sections at MET2. (g-l) Same as a-f on 2013-12-24 03:00 UTC.

and 5.5d), indicate a quite similar stable stratification in the whole lower tropospheric column in both cases; stronger in the layers below about 2.5 km and weaker above. The temperature profile in Figure 5.3d evidences that the latter level corresponds with the depth of the cold air. Winds are northerly in these lower layers to the north of the mountains, with somewhat higher speeds above 20m/s upstream from MET1 than further east, north of MET2.In both cases, winds above the cool pool are much weaker, and back to easterly component at about 4000m. Markowski and Richardson [169] outline seven conditions conducive to DSWS, albeit not all of them absolutely necessary. These conditions are: a mountain with steeper lee slope (1) crossed by strong winds (> 15m/s) (2) mostly normal to the barrier (3). A stable layer above the top and less stable above that (4) with cold air advection and large-scale subsidence to maintain the stability (5). Apart from this, reverse wind shear above (6) and no cool pool in the lee (7), is also desirable. These conditions are all perfectly met for both locations analyzed, as discussed previously, and indeed intense downslope windstorms occur in both cases.

The stably stratified barrier cross flow displays wave activity from early on (Figure 5.5a), and wave breaking enhances turbulent mixing and yields a region of weak stability and reverse flow immediately downwind from the mountain crests (Figure 5.5a 5.5d). In both cases, isentropes on the windward side sink sharply under these layers of low stability on the lee side, much more pronouncedly for the tallest mountain (Figure 5.5d-e-f). Encompassing the well mixed region to the lee, a split streamline develops (Smith et al, 1985), and below its lower branch there is flow thinning and a significant increase in wind speed. The particular features existent on the lee side differ, however, depending of the height of the topographic obstacle. The strong accelerated flow bounded by intense turbulence extends for many kilometers downwind from the lowest mountain, while ending with a hydraulic jump and rotors at the foot when the barrier is higher. The formation of either of these lee wave events is related to the Froude number upstream [158].

Figure 5.6a plots the Froude number (Equation (1)), calculated using the average of the variables at the first 5 sigma levels, approximately between 16 and 120m above ground, at the crest, H=936 m for MET1 case and H= 1736 m for MET2. For the lowest mountain, $Fr \approx 2.5$ during nighttime and even higher at some other times during the day, indicating supercritical conditions. The Brunt-Väisälä frequency is between 0.020 and 0.025 1/s. The generated mountain waves have relatively short wavelength and a modest hydraulic jump that propagates downstream can be seen at the initial stages of the episode at 15 UTC December 23 (Figure 5.5a-f). 12 hours later, during nighttime, the aforementioned strong jet extending for tens of kilometers downwind is fully formed, with values above 35 m/s at about 750m above ground and strong turbulence at the surface and in the layers above the jet, where stability is much reduced. The temperature profile upwind (at 3 UTC December 24 and location UP1 in Figure 5.5) shows stable conditions for the lowest troposphere, specially marked at crest level, below the inversion at about 2000 m signaling the depth of the cool pool. At the observation location MET1, downwind from the mountain, the lowest layers up to about 750 m are well mixed, the result of the intense surface turbulence. Above the latter height and up to about 1.5 km elevation, a strongly stable layer exists corresponding with the aforementioned packing of the isentropes (and streamlines). This is where the highest wind speeds are found. Stability is much reduced further high, in the region encompassed by the dividing streamline.

For the higher mountain north of MET2, $Fr \approx 1$ consistently in the period, indicating a critical flow regime, prone to the formation of HJs [156]. The Brunt-Väisälä frequency is between 0.012 and 0.015 1/s and the generated waves have higher amplitudes than in the MET1 case. Wave overturning and breaking is also much more pronounced (Figure 5.5a-c) and the forming well mixed region to the lee of the crest is deeper. Isentropes and streamlines that sink underneath this region are packed in a very shallow layer on the lee slope of the mountain, generating an intense downslope windstorm with speeds above 35 m/s at the surface. These strong winds end abruptly at the foot of the hill, where the flow transitions to subcritical conditions and a marked stationary hydraulic jump forms, with vertical wind speeds of 6 m/s. A rotor extending from the jump to the location of observation station MET2 is also evident in Figure 5.5d-f. The temperature profile upstream is very similar to that of the MET1 case, but downwind from the mountain at location MET2, lacks the strongly stratified layer present in the case of the lowest mountain.

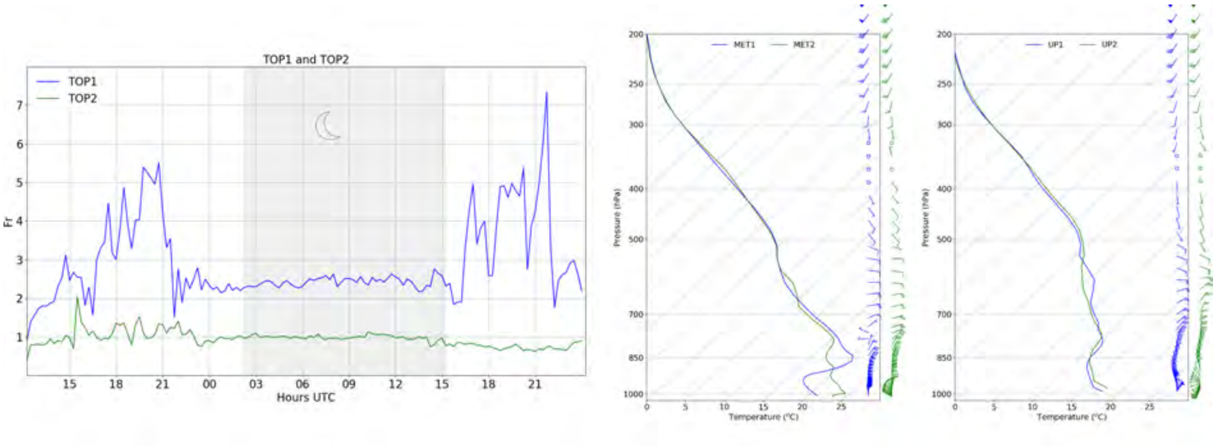

Figure 5.6: (a) Froude number in front of each station on the top of the mountain, TOP1 and TOP2. The grey zone represents night time. (b) Temperature vertical profile in MET1 and MET2 and (c) the same for their corresponding upstream points UP1 and UP2.

Results from the innermost nested grid d05 with the finest resolution (Figure 5.7) suggest that trapped lee waves develop in the MET1 case within the high stability layer where the strongest winds are found, just below the low stability region aloft that prevents their vertical propagation. This wavelike pattern is a common feature in DSWS periods [77, 157] and fully formed 12 h later (Fig 7c), extends for more than 100 km downstream aligned with the general orientation in the northwest-southeast direction of the Sierra in the region. Waves are absent further east in the MET2 cross section, where the topographic barrier is higher and a stationary HJ forms instead, as discussed above.

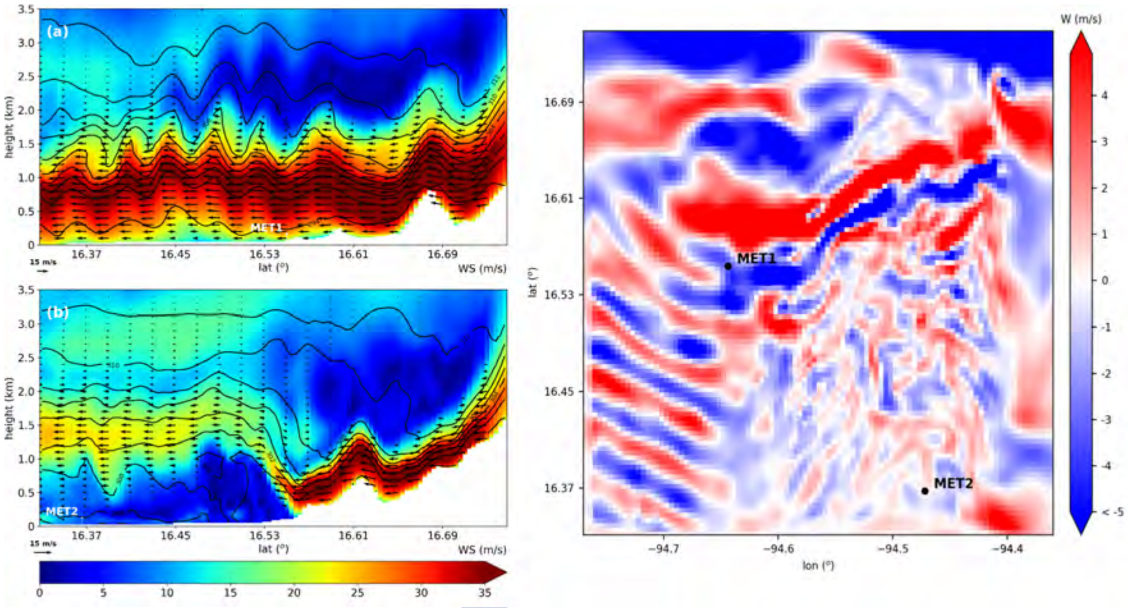

Figure 5.7: As in Fig 5.5a and 5.5d, 2013-12-24 03:00 UTC, d05 vertical cross sections at (a) MET1 and (b) MET2 of potential temperature (contours, K), wind speed (shades, m/s), and wind arrows. (c) Vertical wind speed (m/s) in d05 at sigma level 17 (about 1400 m above ground) when the trapped lee wave pattern in the region is fully formed at 15:30 UTC 2013-12-24.

Validation

Finally, we contrast our simulation results with the very few data available for validation at meteorological stations MET1 and MET2. The two plots in Figure 5.8 compare the simulated wind speed (in d04 and d05) with observations from both stations.

Wind speed results from d04 and d05 at location MET1 are quite similar, and compare well with observations (Figure 5.8a), slightly better so those from d05, with a mean absolute error (MAE) of 1.55 m/s (Table 5.2). The similarity in the low mean error between both simulations and their high correlation throughout the period are due to the nature of the event in that area, an intense and mostly steady jet that the d04 domain resolution (1.3 km) is already capable of resolving accurately. However, results in MET2, which registers the HJ situations, present more differences between d04 and d05 (Figure 5.8b) and there is a significant improvement in d05 with respect to its parent domain d04. Wind speeds in d04 are overestimated (Mean error ME = 2.76 m/s), and present a daily cycle that is absent or very subtle in the observations. The complexity and fast variability of HJs formation in this area are better resolved in the higher resolution grid, which perhaps reproduces more accurately the stagnant flow and rotor formations downstream from the HJ. With regard to wind direction, errors are small for MET1 and significantly higher for MET2, due to the same reasons. As for wind direction, results from the finer grid d05 are also better than in d04. Temperature errors are equal or below 1 K in both locations and domains, hence the surface thermal evolution is well captured.

Lee waves can promote orographic cloud formation at different scales, depending on the amplitude of the wave and the elevation [176, 177]. Model results in d05 suggest that lenticular clouds form at the crests of the trapped lee waves depicted in Figure 5.7. Figure 5.9a shows

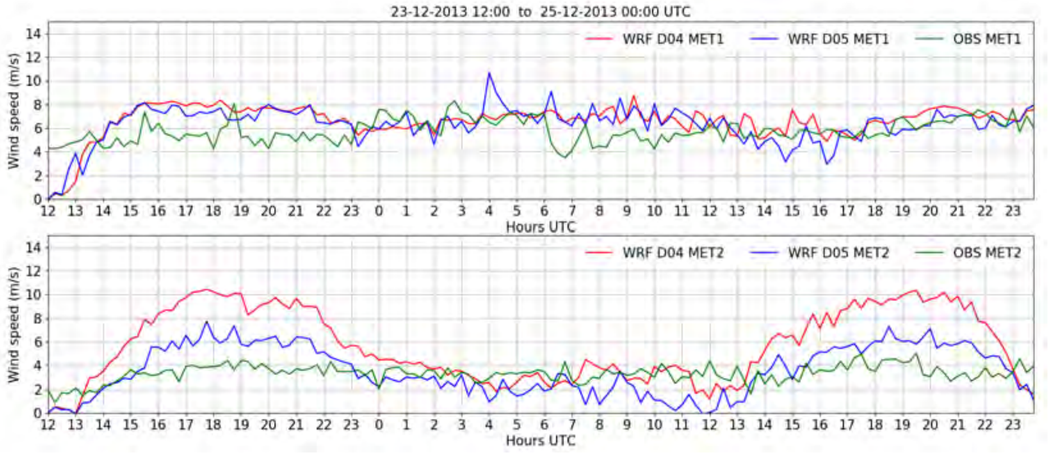

Figure 5.8: (a) Wind speed comparison among observations at MET1 (green), and model output from d04 (red) and, d05 (blue). (b) Same for station location MET2.

	WS MAE (m/s)	**WS ME** (m/s)	**WD MAE** (°)	**T MAE** (K)	**T ME** (K)
MET1 D04	1.82	1.26	16.15	0.85	-0.80
MET1 D05	1.55	0.80	13.63	0.77	-0.71
MET2 D04	2.76	2.35	27.87	0.71	0.01
MET2 D05	1.31	0.18	24.07	1.02	0.61

Table 5.3: Wind speed (WS), wind direction (WD), and temperature (T) mean errors (ME) and mean absolute errors (MAE) at MET1 and MET2 locations during the simulated period and for the two higher resolution domains (d04 and d05).

a 3D representation of the modeled cloud water mixing ratio at 2013-12-24 15:30 UTC in d05. Cross sections of wind speed at the surface observation locations MET1 and MET2 as in Figure 5.5 and Figure 5.7 are also included for reference. A 2D view of the same cloud mixing ratio variable and wind arrows at sigma level 17 (about 1.4 km above ground), revealing existing clouds, are depicted overlaying a satellite image of the area. An actual satellite image from Geostationary Operational Environmental Satellite - R Series (GOES-R) (`http://www.goes-r.gov/education/docs/fs_imagery.pdf`) around the same time is shown for comparison, indicating that remarkably similar mountain wave cloud formations were indeed observed in the area. The actual existence of these lenticular clouds with the same location and pattern as in the simulation further validates the model results.

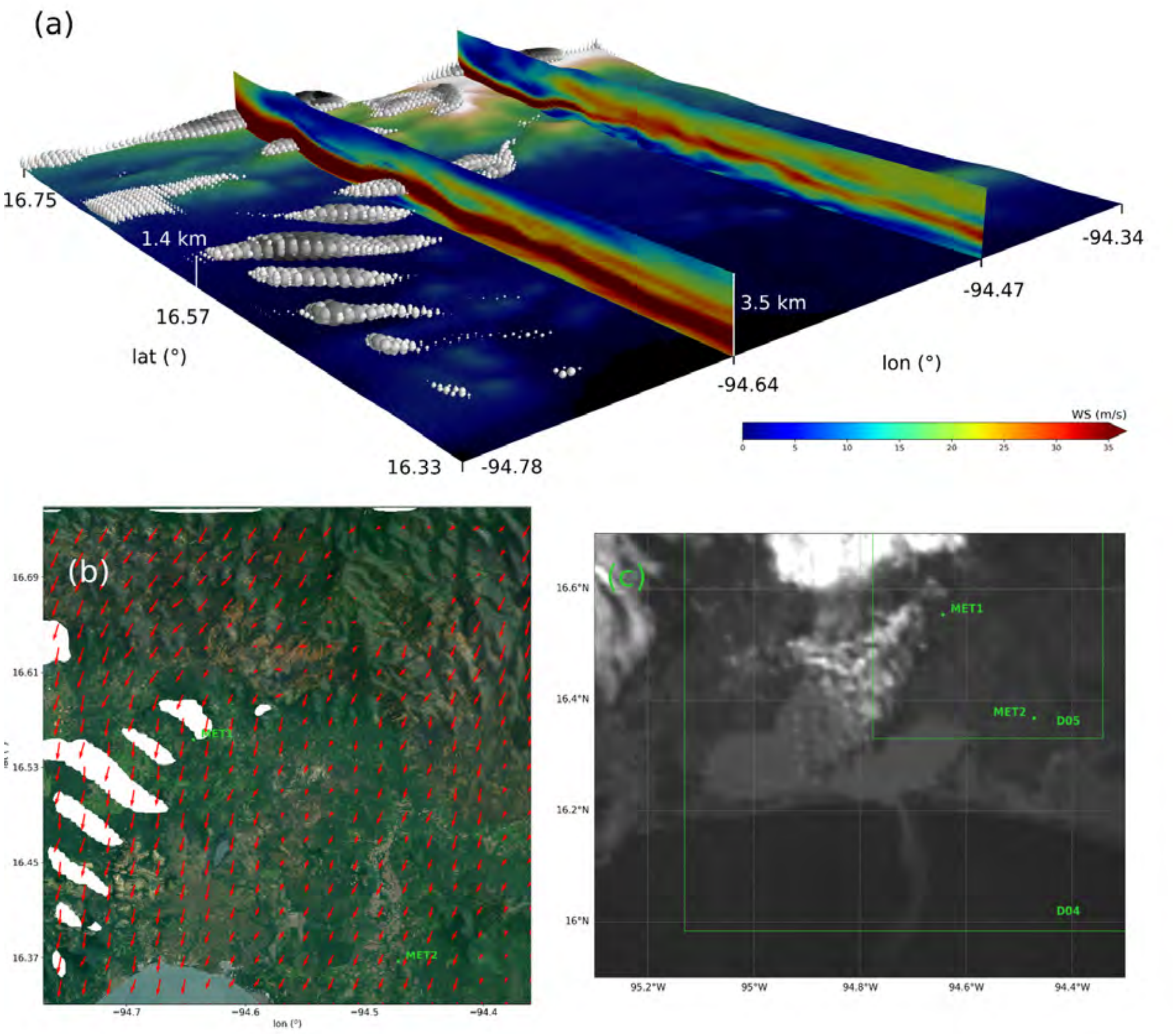

Figure 5.9: (a) Cloud water mixing ratio 3D representation in d05 at 2013-12-24 15:30 UTC. The two cross sections show the N-S wind profile at the longitudes of the meteorological stations MET1 and MET2. (b) Satellite image of the terrain in d05 and cloud water mixing ratio (white shades) and wind arrows at about 1.4 km above ground. (c) GOES-R satellite image on 2013-12-24 20:30 UTC, revealing very similar lenticular cloud formations in the same locations.

Summary and conclusions

In the present work, we studied lee wave phenomena occurring during Tehuano events on the Pacific side of the Isthmus of Tehuantepec using WRF high-resolution simulations. Orographic forcings at different scales result in the well-known gap wind jet off Chivela pass, but also in downslope windstorms and hydraulic jumps in the neighboring mountains. We analyzed these phenomena in an episode in December 2013 having the typical genesis of Tehuantepecer wind events. An Arctic air mass in North America pushed as far south as the bay of Campeche due to cold air damming east of the Rockies continuing to the east of the Sierra Madre Oriental range in Mexico. The displacement of the associated high-pressure system on the wake of the cold front created large pressure differences across the Isthmus of Tehuantepec, ultimately producing the strong mountain gap winds through the low elevation of Chivela pass.

The model simulates these intense winds, blowing with speeds at the surface of more than 25 m/s that extend for many kilometers from the mountain gap, fanning out well into the Gulf of Tehuantepec, as it is commonly observed in Tehuano events [185].

The depth of the cold surge on the coastal plains of the Gulf of Mexico side of the Isthmus is about 2500m, therefore thick enough to surmount the lower elevations to the west, and especially to the east of Chivela pass. The flow over these mountains results in intense downslope wind storms to their lee, with the generation of intense turbulence, hydraulic jumps and rotors, depending on the particular height of the topography. We focus on two locations of different barrier elevation from where there are surface observations downwind: one of 963m closer to Chivela pass and another further east, with height increasing to 1736m.

The thermodynamic characteristics of the air mass are rather uniform upwind both mountains, with strong stability within the cool pool and weaker above, and intense northerly winds that back and weaken to a more easterly component aloft. Mountain waves are generated in both cases, with smaller amplitudes for the lower mountain, where the Brunt-Väisälä frequency at crest height is between 0.020 and 0.025 s-1, than for the higher mountain, where the Brunt-Väisälä frequency is about half. Wave breaking produces mixing and generates a region of low stability to the lee of the mountains, which is deeper where the waves have higher amplitude. The Froude number is around 2.5 at crest height in the lower barrier and the flow presents a supercritical behavior. The region of low stability to the lee of the mountain lies above about 1500m and leads to a packing of the isentropes and streamlines underneath, resulting in strong stability and flow acceleration. An intense jet develops with wind speeds of 35 m/s at about 750m above ground extending for tens of kilometers downwind from the mountains. Wind speeds are reduced closer to the surface due to intense turbulence. Trapped lee waves form at about 1500m, just below the well mixed layer aloft that prevents their vertical propagation. The Froude number decreases to about 1 further east as elevation rises and the flow presents a critical regime. Isentropes on the windward side of the mountain sink much more pronouncedly under the wider mixed layer generated by wave breaking to the lee, and are tightly packed in a shallow layer above the surface. This generates an intense wind storm on the lee slope of the mountain, with surface wind speeds up to 35 m/s. The accelerated flow down the mountain ends abruptly at its foot, where the flow turns to subcritical state and a marked stationary hydraulic jump forms, with vertical velocities of 6 m/s. A rotor circulation develops further downstream from the jump.

Only limited observations are available to validate our model results. Errors in surface wind speeds, directions and temperature are small at the only two stations available on the Pacific coastal plain downwind from the mountains. In addition, lenticular clouds similar in location and pattern to those produced by the model, are apparent in satellite imagery of the day of the event, provides valuable indication that the mountain lee wave phenomena simulated indeed corresponds to a real scenario.

Our model results suggest that more extreme wind events develop in the area during Tehuano evends beyond the gap wind jet. This include downslope wind storms and hydraulic jumps, which are intense and highly turbulent flows that can have a substantial impact on the existent wind farm industry in the region.


USC
UNIVERSIDADE
DE SANTIAGO
DE COMPOSTELA

Chapter 6

Microscale phenomena analysis

Introduction

The study of microscale wind flow phenomena has always been a point of interest within the wind industry. There are several well know wind events related with it that turbine designers and operations managers have to take into account, such as high operating gusts, extreme direction change, high coherent gust with direction change or extreme wind shear. All these turbulent wind events have been defined and categorized for a long time within the sector [118]. However, their capacity to, for example, cause torque reversals that can damage a turbine, or provoke decalibrations on hub sensors, have only recently been recognized and measured [30]

A good part of these recent developments has been possible thanks to numerical modeling tools, which are continuously improving their techniques within turbulent phenomena characterization and forecasting. Specifically, this is one of the main strengths of CFD (Fluid Dynamic Simulations) models, as introduced in Chapter 2. These tools are useful and currently well established in the wind energy field to study future installation areas and design new wind farms [119, 120, 121]. However, as stated in previous chapters, they always work over stationary conditions, even with the best initial conditions, these simulations do not allow us to capture all the complexity of the phenomena at different scales that affect each region of study and which have a significant effect on turbulent fluxes that can flow in the area.

Another modeling tool which is increasingly being used is WRF Large Eddy Simulations (LES). Based on a very high-resolution WRF simulation and a deactivation of the planetary boundary layer scheme, this WRF configuration can be utilized to simulate turbulent wind flows for wind energy applications [20]. WRF LES permits run simulations in two different ways, as an ideal case or within a nesting configuration fed by global model and mesoscale conditions in the boundaries (real-world). Many current WRF LES studies published are based on these ideal cases [122, 123]. This methodology assumes periodic boundary conditions and horizontal homogeneity [124] with the relatively uncomplicated surface. WRF LES ideal is extensively used for wind farm applications such as wakes studies, as commented in Chapter 4, or to analyze the performance of wind turbine schemes and boundary forcings [125, 20].

WRF LES real-world (LES-RW hereafter) is also each day the more commonly developed modeling technique. These simulations are fully coupled to the mesoscale parent domains giving realistic atmospheric forcing to the LES simulation. The high resolution of this methodology is capable of resolving an important part of the turbulent wind spectrum phenomena (Chapter 1, Figure 1.4). A representative example of this modeling tool is the manuscript presented by Rai et al. [36] , where they run an LES-RW 30m resolution for a complex terrain area in Oregon (US) to study the effect of horizontal grid spacing on the coarser mesoscale nesting domains. Huang et al. [83] use LES-RW in combination with the Advanced Hurricane Weather Research and Forecasting model to resolve micro-scale wind velocity fields in Hangzhou (China) during a typhoon event. Doubrawa et al. [126] evaluates different approaches for treating grey zone resolutions [127] in full-physics LES-RW of the atmosphere with observational data obtained during the Prince Edward Island Wind Energy Experiment (Canada) [128].

In WRF-LES, proper boundary conditions are fundamental to reliably produce turbulence fields in the finer domain [129]. There are two main ways to provide turbulent boundary conditions to an LES-RW. The first is, the possibility to use several domains in LES mode, which is the most common method, used for example in [130] with 3 LES domains or in [131] with two. The second is, the possiblity to introduce perturbed boundary conditions artificially generated just for the innermost LES domain. Within this field, the generalized cell perturbation method developed by Muñoz-Esparza and Kosović [132], Muñoz-Esparza et al. [133] it is highlighted. It employs a novel stochastic approach based upon finite amplitude perturbations of the potential temperature field applied in the region near the inflow boundaries of the LES domain.

It is fundamental to keep developing new modeling techniques to resolve with more reliability, turbulent microscale phenomena, and make them available to more users. These types of simulations can be high-fidelity tools that provide valuable information about turbulent processes in a wide range across atmospheric stability situations, both in flat regions as well as in complex terrain. In this study, we evaluate LES-RW on a complex terrain wind farm area in the south of China. To do that, we simulate a 10-day period broken into daily runnings using a mesoscale-microscale coupling configuration finishing in two domains LES and reaching a 98 m horizontal resolution in the innermost one. To solve the instability of the simulations, we apply a zonal smoothing technique which softens the orography close to numerically unstable points. Moreover, the results obtained are validated using observational data from three meteorological stations in different points along the area. The rest of the chapter is organized as follows: in Section 6.2 the methodology is explained in detail, focusing on the WRF-LES configuration, the zonal smoothing technique, and the turbulent intensity calculation. In section 6.3, the main results obtained are shown, and finally, in section 6.4 the conclusions are discussed.

Methodology

This section explains the configuration and tools used to perform LES-RW simulations in the area studied. This kind of running requires a specific scheme configuration and nesting design (6.2.1), different adjustments in the preprocessing part such as the terrain smoothing (6.2.2) and an explicit calculation of the Turbulence Intensity (6.2.3).

Studied area and WRF LES configuration

To perform the simulations of this study we use the Advanced Research WRF (ARW) model [32] version 3.9 (WRFV3.9). In this case, we focus the analysis on a small region using a very high-resolution domain, so a meso-microscale multiple nesting is necessary. Specifically, the area of interest is a complex terrain wind farm future location in the Chinese province of Guangxi (UTC+8). This region on the southeast of the country (Figure 6.1b) presents a subtropical monsoon climate. The weather is generally soft and with four seasons. Summer is the rainy season, especially in June. Autumn and spring are mild, and winter is characterized as being breezy and slightly wet. The prevailing wind directions in the area are North and Northeast.[134]

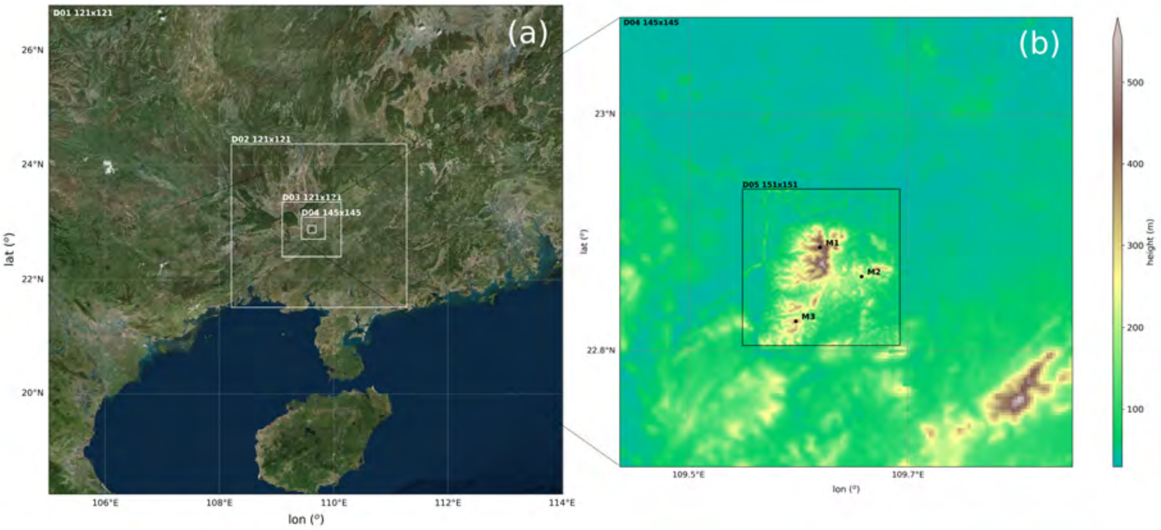

Figure 6.1: WRF nested domain configuration. (a) Coarser three domains with their number of grid points. (b) Higher resolution domains (d04 and d05), both with their respective topographies. MET1, MET2, and MET3 are the locations of the meteorological stations used as validation points (Subchapter 6.2.4).

We use a nesting configuration with one parent domain centered in 22.79 latitude and 109.66 longitude and four nested domains (d02, d03, d04, and d05) with one-way interaction (Figure 6.1c). As indicated in Figure 6.1, the first three domains, with 8, 2.6 and 0.88 km horizontal resolution have 121x121 grid points. In the higher resolution LES domains (296 m and 98 m resolution) we increase the number of points, d04 with 145x145 and d05 with 151x151 grid points. In LES-RW It is essential to use domains with big dimensions to leave enough space to mix the boundary conditions properly and to develop the turbulent eddies all over the domain [36]. The horizontal resolution in LES also acquires more importance than in mesoscale simulations, in this study, there are 55 vertical levels in all domains, with a non-linear distribution and with more of them near the ground. Thus, the aspect ratio ($\alpha = \Delta x / \Delta z$) in the lower PBL is close to 4, which is in the recommended range in LES simulations [20] . We maintain this fine vertical grid spacing in all the domains, to capture as wide a range of motions as possible over the depth of the boundary layer. In LES simulations, apart from looking for more accurate reproduction of near surface thermal fluxes, it is essential to use this high vertical resolution to avoid numerical instabilities in the running.

In common with the rest of the studies in previous chapters, terrain elevation data used in D04 and D05 comes from the ASTER Global Digital Elevation Map (GDEM) from USGS [66] with a resolution of 30 m. For land use static data, however, we use a different database as in the rest of the experiments of the thesis. Specifically, we define the land-use variable with the 30-m Finer Resolution Observation and Monitoring of Global Land Cover (FROM-GLC) from the Centre for Earth System Science, in Tsinghua University, Beijing [135]. This very high-resolution database was produced using Landsat Thematic Mapper (TM) and Enhanced Thematic Mapper Plus (ETM+) data.

To obtain realistic LES performance in D05 domain, we apply an LES configuration in D05 and D04. In this way, D05 is provided with LES turbulent boundary conditions. The main difference between the first three domains (MESO domains) and the LES ones is the planetary boundary layer (PBL) scheme. We use MYNN PBL [72] parameterization to model the turbulence in MESO domains. However, in LES domains, we deactivate this parameterization, allowing the model to resolve the large eddy microscale phenomena explicitly. In addition to this, we employ a 3-D turbulence model to parametrize the Subgrid-scale turbulence (SGS hereafter), in this case, the TKE 1.5 order closure model [136]. The next table summarizes the relevant physics schemes used in D04 and D05 LES domains:

Physics	**Name**
Planetary Boundary Layer	Disabled
Microphysics	Morrison, Thompson and Tatarskii
Cumulus	Disabled
Shortwave Radiation	RRTMG Iacono et al.
Longwave Radiation	RRTMG Iacono et al.
Land Surface	Unified Noah Land Surface Model
Surface Layer	Nakanishi and Niino surface layer scheme
Turbulence model	1.5 order TKE closure (3D)

Table 6.1: Main parameterizations in higher resolution domains (D04 and D05).

Turbulence intensity calculation

Some WRF planetary boundary layer schemes such as, MYNN (used in this study in coarser domains), the non-local first-order YSU [67] or Shin and Hong [137], parameterizes the vertical profile of mixing in PBL and also provides prognostic TKE variables such as output which can be used to calculate the Turbulent Intensity (TI). However, WRF-LES does not employ any of these parameterizations at its very high resolution, PBL scheme is deactivated with the expectation that Navier Stokes fluid dynamic equations can resolve an important part of the kinetic energy in the atmospheric boundary layer. In this way, it is possible to calculate

TI in one domain point by using the wind speed standard deviation and its module (Equation 6.1), which is how it is generally measured with observational data [138]. In this particular case, we use a 4 Hz temporal frequency output from the model to obtain the standard deviation and mean wind speed for each 10 min period. However, despite the high horizontal resolution used (98 m), there are still small turbulent phenomena that the model does not resolve. Any microscale event with a smaller scale than the grid resolution (SGS) is not taken into account in the TI calculation commented above. In relation to this, the 1.5 TKE 3D order closure used in the simulations computes an SGS TKE internally as a prognostic variable to predict the eddy viscosity [136]. This TKE (TKE_{SGS}) is extracted from the model and used to calculate the fraction of TI related to the smaller non-resolved eddies (Equation 6.1 TKE_{SGS}).

$$TI_{Tot} = TI_{LES} + TI_{SGS} = \frac{\sigma_{ws}}{\sqrt{u^2+v^2}} + \sqrt{\frac{TKE_{SGS}}{u^2+v^2}} \tag{6.1}$$

where u and v are the wind components, $sigma_{ws}$ is the wind module standard deviation every 10 minutes, and TKE_{SGS} is the turbulent kinetic energy parameterized with SGS.

TI_{SGS}, even considering the high horizontal resolution employed in the experiment, can be very important in the calculation of the total TI. Apart from this, having two sources of turbulence characterized gives added value to the study of a region through these methods.

Initial-boundary conditions and observations

The study covers the period between 2017-09-10 and 2017-10-19. These 10 days have registered a mean WS of around 7 m/s in the stations used as validation points, a value which is also close to the annual mean value for this area and height. GFS analysis data from the National Center for Environmental Prediction (NCEP) is used as initial and boundary conditions, with a 3-h update interval. The horizontal resolution of this dataset for all variables is 0.25 x 0.25 deg, with 32 levels ranging from 1000 to 10 hPa. Currently, GFS0.25 has a public database begining February 2015. GFS has an initialization every six hours (00 UTC, 06 UTC, 12 UTC, 18 UTC), for each daily simulation we use the first file from each initialization and its 3h file (+12 h spin up from previous day).

The observational data used in this work is provided by Xinjiang Goldwind Science & Technology Co. (`http://www.goldwindglobal.com/`) collected from meteorological stations at hub height designed to study future wind farm areas. Precisely, 10 minute-minute-intervals of wind speed, wind direction, and turbulence intensity are measured at 80 meters height and temperature at 10 meters height. The next table outlines the location and terrain height of the validation points.

Terrain smoothing

WRF LES simulations, especially in complex terrain, are usually numerically unstable. In many cases, this is because of significant height terrain differences between one grid point and its neighbor. During the geogrid process, the WRF model let us use a smoothing tool that helps to avoid this kind of 'unstable' points. This tool literally smoothes the terrain in our simulation domain, reducing the HGT differences between grid points. Figure 6.2b shows the result of a 12-pass-smoothing (the ground is smoothed twelve times by the configuration selected) over the d05 domain original terrain data (Figure 6.2a). A strong softened HGT can be distinguished if

ID	Longitude (°)	Latitude (°)	Terrain height (m)	Obsevation height (m)	
				WS/WD/TI	T
M1	109.61977	22.88750	471.6	80.0	10.0
M2	109.65786	22.86325	266.5	80.0	10.0
M3	109.59784	22.82531	226.1	80.0	10.0

Table 6.2: Meteorological station locations and heights.

we compare these two images. This can help us in some conflictive points, but can also reduce accuracy in our simulation, especially in LES cases.

One more laborious, but more accurate possibility with smoothing, consists in locating the unstable points in a simulation and performing a gradual smoothing; stronger to softer from the center of thepoints outwards to their environments. To find the unstable points from a simulation without smoothing we decrease the timestep and check the value of the vertical wind component (W). With this scenario, unstable areas tend to register unreal very high values (>50 m/s) near the ground, but the simulation keeps running some time because of the low timestep, which temporarily avoids the violation of the vertical CFL condition (Courant-Friedrichs-Levy number [139]). With the location of the unstable points, it is possible to modify the original HGT variable in the static preprocessing file (*geo em.d0X.nc*) by taking concentrical subregions of different smoothed outputs from the points (Figure 6.2b). (tool used: python's xarray library `http://xarray.pydata.org/en/stable/`).

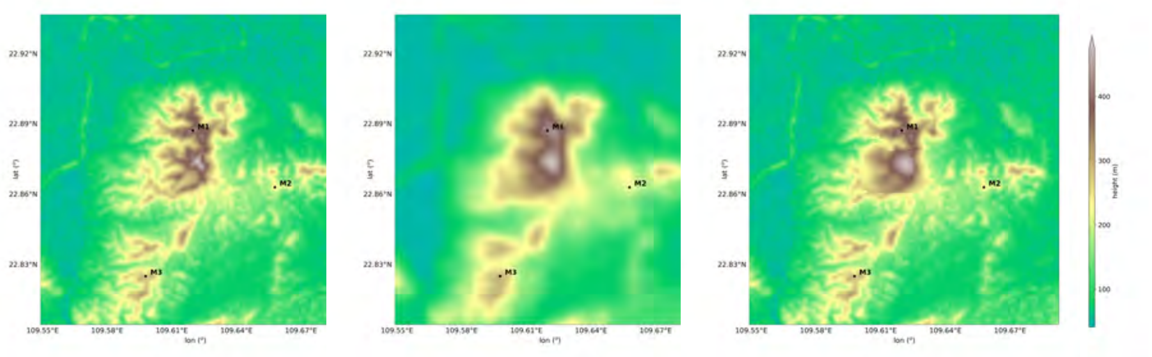

Figure 6.2: (a) D05 original HGT variables, (b) D05 HGT with 12-pass-smoothing, (c) D05 HGT with zonal smoothing over unstable points at the centre of the domain.

Apart from the smoothing issue used to avoid numerical divergence in the simulations, the higher resolution domains have been established without cutting any significant mountain height with their boundaries. This is a consideration always recommended with WRF simulations, but it acquires more importance in potentially unstable runnings as in this study.

Results and discussion

This section outlines the main results of in this study. We validate the results of all the period studied with the observational data available from several points of the area of interest. Precisely, in subsection 6.3.1 we present different mean errors and plot representations for wind speed, wind direction, and temperature. In subsection 6.3.2 we focus the analysis in the TI calculation results.

General results

Taking the same line as previous chapters, in this experiment we represent the observations for meteorological stations compared with the results from the model. These figures and the different statistical measures calculated for the whole period (Chapter 3, Equations 3.4 to 3.8) depict the capacities of WRF-LES simulations to represent the local wind phenomenology of this complex terrain area. First, we analyze the tool regarding wind speed (WS) forecast accuracy. The next figure shows the comparison of the observed and forecasted wind speed module in each station and several mean error calculations for the 10-day analysis.

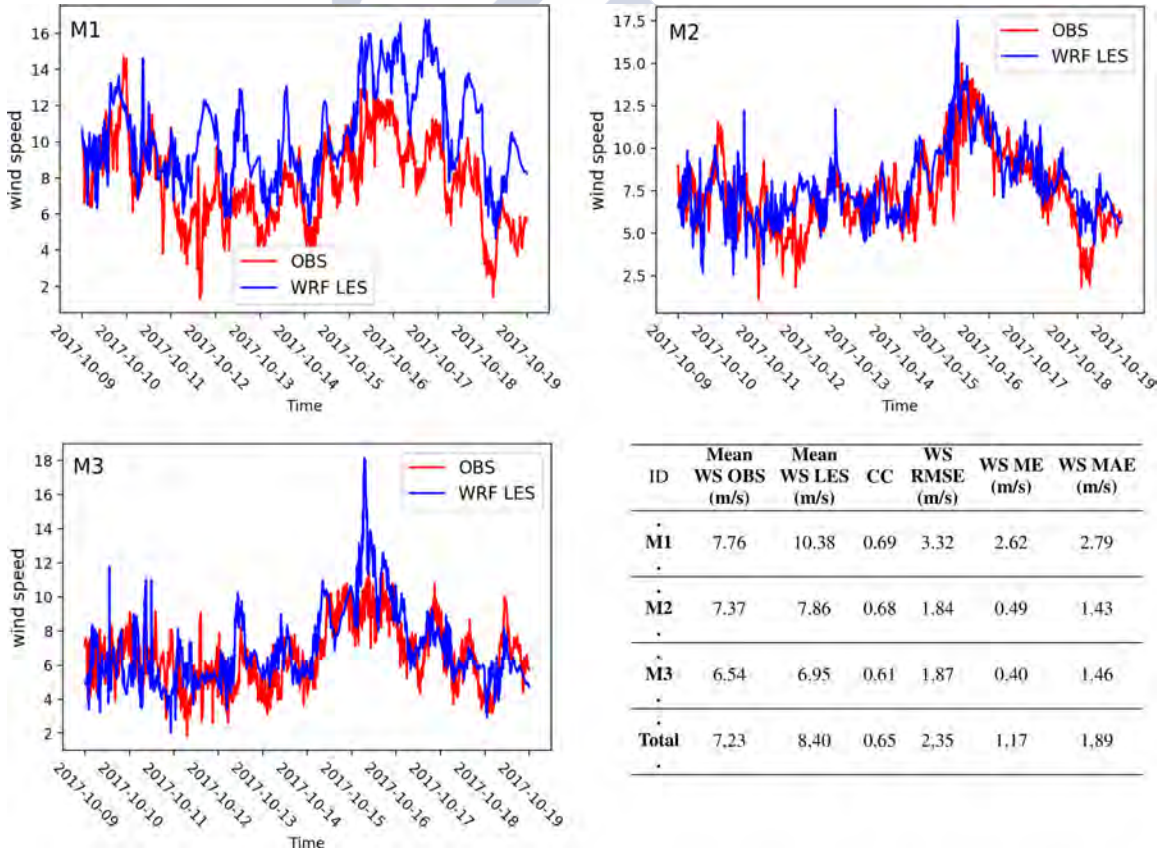

ID	Mean WS OBS (m/s)	Mean WS LES (m/s)	CC	WS RMSE (m/s)	WS ME (m/s)	WS MAE (m/s)
M1	7.76	10.38	0.69	3.32	2.62	2.79
M2	7.37	7.86	0.68	1,84	0.49	1,43
M3	6.54	6,95	0,61	1,87	0,40	1,46
Total	7,23	8,40	0,65	2,35	1,17	1,89

Figure 6.3: (a) 2017/10/09-2017/10/19 (UTC) Wind direction at M1 (80 meters height) for WRF-LES (blue) and observations (red). (b) Same as (a) at M2.(c) Same as (a) at M3.

Table 6.3: Mean wind speed observed and forecasted for each validation point. Different mean wind speed errors measured in each point along the studied period: Correlation Coefficient (CC), Root Mean Square Error (RMSE), Mean Error (ME) and Mean Absolute Error (MAE).

The plot representations and its respective measured errors allow us to comprehend instactly the performance of the simulations. The northernmost station representation displays a significant overestimation in practically all the period studied (Figure 6.3a). This is also reflected in the WS ME, and consequently in the MAE and RSME (Table 6.3). Figure 6.3b and c show much better general results in the other two stations (M2 and M3), with an accurate wind field representation, reaching WS MAE of 1.43 and 1.46 m/s respectively. The ME is also distinctly lower than M1 in both of them (below 0.5 m/s). The significant M1 overestimation reflected in the WS ME and the relatively good CC suggests that at least part of the deviation obtained could be related to a misalignment between observation and model output heights. This could be due to an error in the measurement recording or a deviation in the height of the grid cell and/or its neighbors for this specific point in the model domain. All this leads to a total WS MAE = 1.89 m/s for the three stations, which can be considered a good result taking into account the complexity of the terrain. This MAE is practically the same as the one reached in Coruxeiras wind farm WRF forecasts (Chapter 2, Table 2.4). Leaving aside the mean errors, the three model plots (blue lines) reflect an increase in the variability of each recorded time period. The very high resolution and its respective small temporal scale (timestep) used to perform the simulation are able to reproduce smaller scale eddies (Chapter 1, Figure 1.4 green line) giving more reality to the simulations which is reflected in all the variables recorded.

Continuing with the discussion about the capabilities of LES-RW, we review the model performance predicting wind direction. To do that, in the next figure we present the results of the three validation points following the same structure as with WS in Figure 6.3.

The plot representations and the WD MAE results (Table 6.4) depict satisfactory results during the ten day period. The wind direction, which is maintained between 350° and 100° across all the period, is well estimated by LES-RW, obtaining results close to the observation results across the whole series. This small deviation tendency is visible in the three plots and the MAE results with a total MAE of 17.49°. Despite the prevailing N – NE wind during the whole the experiment (reason of the vertical lines in the center of the plots), there are no significant differences between stations. The southern station, M3, despite being more affected by the topography effects due to the direction of the incoming wind, does not register significant higher deviations (MAE=19.51°) than the other two stations further north (15.36° and 17.62°). Two of the main factors of a proper RW-LES performance are coherent boundary turbulent forcing and a good turbulent phenomena reproduction within the innermost domain.These seem to be well resolved by the domains configurations and the parameterizations used. On the one hand, as it is reflected in the accurate WD M1 and M2 results, the d04 LES domain providesappropriate boundary forcings to the higher resolution domain. On the other hand, d05 maintains the turbulent behavior of the wind fields throughout the region, registering promising WD and WS results in M3, which is mainly affected by the local performance of its own domain.

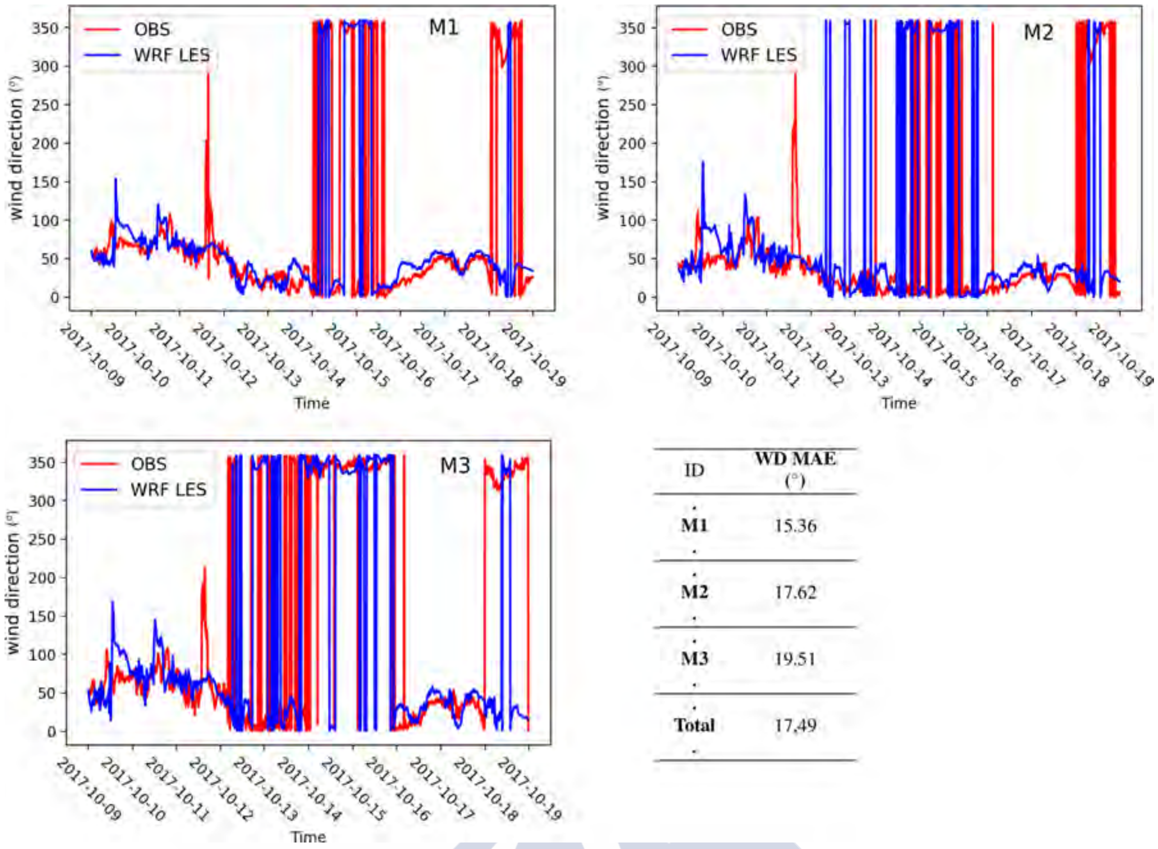

Figure 6.4: (a) 2017/10/09-2017/10/19 (UTC) Wind direction at M1 (80 meters height) for WRF-LES (blue) and observations (red). (b) Same as (a) at M2.(c) Same as (a) at M3.

ID	WD MAE (°)
M1	15.36
M2	17.62
M3	19.51
Total	17.49

Table 6.4: Mean wind direction Mean Absolute Error (MAE) in each point for the period studied.

As can be seen in the WS and WD results for the different stations, RW-LES with the several LES domains forcing technique is able to obtain realistic results across the majority of the area of the domain, even atpoint M3, which is relatively close to its border. This is an advantage with respect to boundary cell perturbation methods which need an extended relaxation zone in all the nearby areas to the horizontal boundary layers to obtain reliable turbulent representations [81]. This makes less area of the domain profitable, which is a problem for situations as in this study, where there are several locations of interest which need to be resolved within the same simulation domain. The only way for these methods to face the relaxation zone issue is increasing the domain area and, therefore, increasing computational costs.

After analyzing one of the main topics of interest in this study, which is the wind representation by LES-RW, we examine the capacities of the tool for resolving the temperature fields near to surface. Specifically, continuing with Figure 6.4 and 6.5 structure, the next figure displays, a comparison between observed and forecasted T at 10-meter height in the three validation points and summary table with different statistical measures for the whole period.

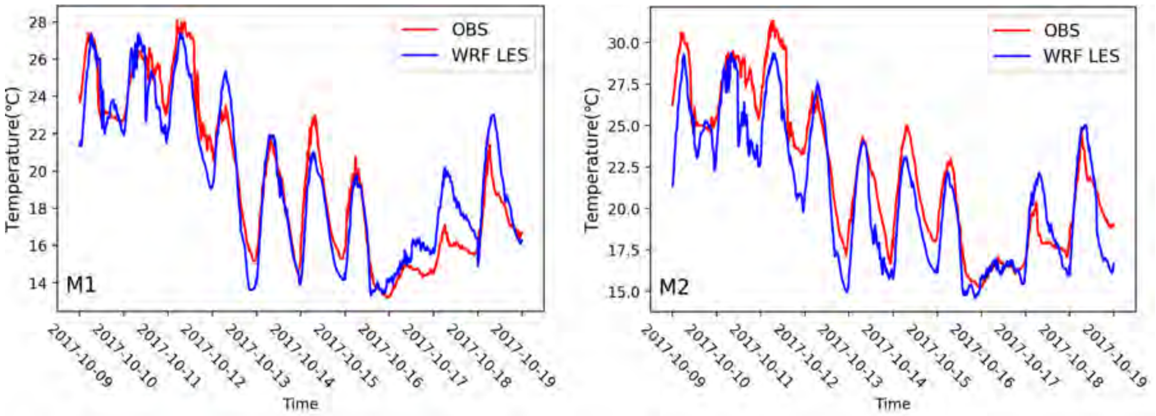

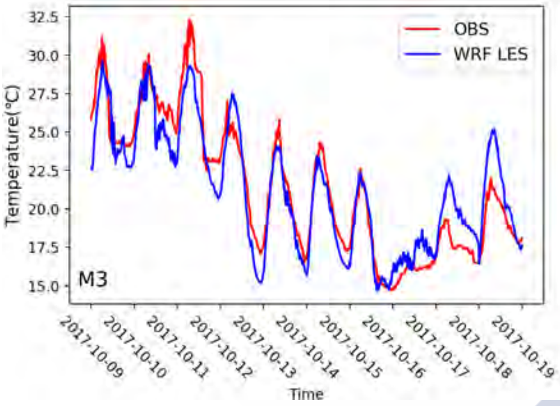

Figure 6.5: (a) 2017/10/09-2017/10/19 (UTC) Temperature at M1 (10 meters height) for WRF-LES (blue) and observations (red). (b) Same as (a) at M2. (c) Same as (a) at M3.

Table 6.5: Mean temperature observed and forecasted for each validation point. Different mean wind speed errors measured at each point for the studied period: Correlation Coefficient (CC), Root Mean Square Error (RMSE), Mean Error (ME) and Mean Absolute Error (MAE).

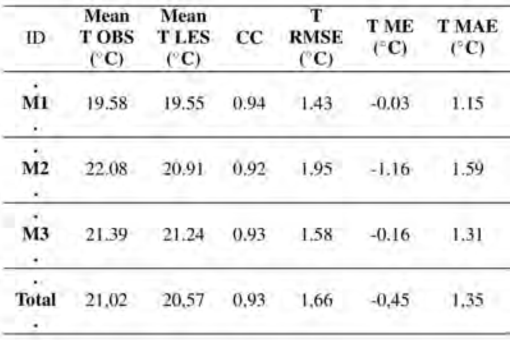

ID	Mean T OBS (°C)	Mean T LES (°C)	CC	T RMSE (°C)	T ME (°C)	T MAE (°C)
M1	19.58	19.55	0.94	1.43	-0.03	1.15
M2	22.08	20.91	0.92	1.95	-1.16	1.59
M3	21.39	21.24	0.93	1.58	-0.16	1.31
Total	21,02	20,57	0,93	1,66	-0,45	1,35

Both plot series comparison for M1, M2, and M3 (Figure 6.5a, b, and c respectively), and mean errors in Table 6.5, show a proper general representation of T in the stations by LES simulations. The mean statistical values are relatively close between the three points. M1 recorded the best results, with the smallest MAE (1.15 °C) and RMSE (1.43 °C), and a practically inesistent ME (-0.03 °C). The southern station, M3, obtains the least accurate results, with higher MAE and RMSE, 1.59 °C and 1.95 °C respectively and a general T underestimation reflected in the series plot (Figure 6.5b), and its ME (-1.16 °C). In any case, these are not important variations between stations; all the T MAE are below 1.6 °C reaching a total mean value of 1.35 °C. The correlation coefficient is very high in the three locations, something which is also noticeable in the plot series representation. CC T results cannot be compared with the same statistical measure for WS or WD, the temporal scale of variability of T is different to WS. In any case, the total mean CC = 0.93 can be considered as an excellent result for a near-surface temperature.

Temperature validation can be summarized by small MAEs, practically no ME in M1 and M3 and a very high CC in all cases. The accurate representation of T at the 10-meter height reflects that the simulations are well resolving that surface layer-terrain fluxes well and this has a direct effect on the correct reproduction of the microscale wind behavior that we are looking for in this study. Apart from an appropriate physical schemes configuration and a high horizontal resolution, the implementation of accurate land use data, as in this experiment (FROM CLC 30m), seems to have a major positive effect on the reproduction of T fields, especially at this low height. When we are running simulations at this high resolution, and we want variable series for one specific point, it is very important to check the aspect of the LU database input at the locations analyzed and their near surroundings. A mistake in the land use in our validation point can provoke a notable bias in the output during all the period simulated.

After seeing the evaluation of the forecasting tool with WS, WD and T validations at point we check we can affirm that the LES-RW yields a good representation of an important part of the microscale phenomena in the area studied. The main statistical indicators used for each variable (Table 6.3, 6.4 and 6.5) score low errors at all the points. The more significant deviation from observations is registered in WS results for M1. Taking into account the excellent WS results in M2 and M3, and the low WD errors at all the points, the source of overestimation seems to be related with an inaccuracy in the orography data. The very good T ME registered in M1 partially discards the possibility of a mismatch between model output and observation height. However, there could still be incorrect height data at the north/northeast of the point which makes the wind blow over the point with a higher speed than observations have registered.

Turbulence Intensity

In this subsection, we address the turbulence intensity measurement from RW-LES. In particular, we obtain the forecasted TI following the calculation described in 6.2.2 in the validation points at 80 meters height and we analyze the results using the observational data from the meteorological stations at this same height. First, and continuing with the same format as in the previous subsection, Figure 6.6 displays a plot representation of TI forecasted and observed in the three locations and a summary table with different mean statistical values for each point and the total mean of them.

In a first quantitative assessment, TI RW-LES results in Figure 6.6 reflect one common thing in the three plots, real behavior. The TI reproduced by the model presents a high variability throughout all the period which concords with the real data from observations. The TI obtained in WRF mesoscale simulations, using parameterized TKE values, is not able to reproduce these variations because the model configuration does not have enough spatial and temporal resolution to capture these motions. Aside from this, the simulations are also capable of reproducing the daily cycle that this variable uses to present higher values during the daytime (thermal influence) and lower ones at night.

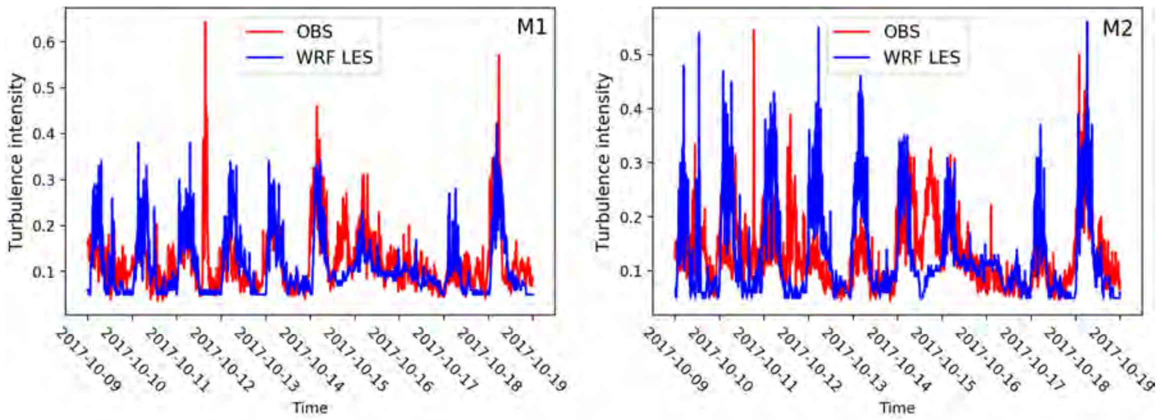

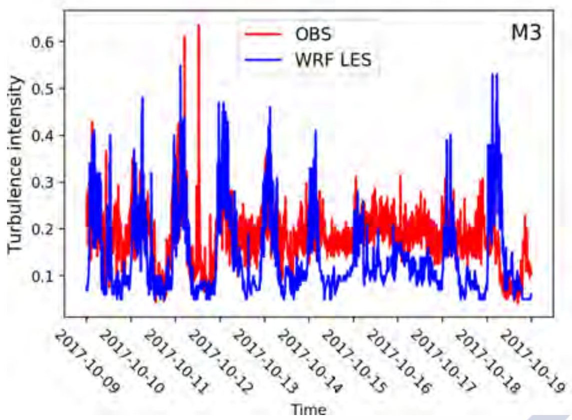

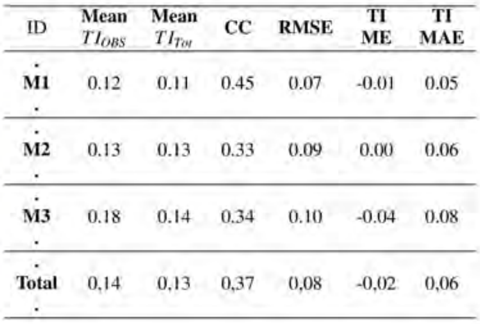

ID	Mean TI_{OBS}	Mean TI_{Tot}	CC	RMSE	TI ME	TI MAE
M1	0.12	0.11	0.45	0.07	-0.01	0.05
M2	0.13	0.13	0.33	0.09	0.00	0.06
M3	0.18	0.14	0.34	0.10	-0.04	0.08
Total	0,14	0,13	0,37	0,08	-0,02	0,06

Figure 6.6: (a) 2017/10/09-2017/10/19 UTC turbulent intensity at M1 (80 meters height) for WRF-LES (blue) and observations (red). (b) Same as (a) at M2.(c) Same as (a) at M3.

Table 6.6: Mean turbulent intensity observed and forecasted for each validation point. Different mean TI errors measured in each point for the studied period: Correlation Coefficient (CC), Root Mean Square Error (RMSE), Mean Error (ME) and Mean Absolute Error (MAE).

Focusing on the mean results (Table 6.6), M1 registers the best MAE (0.05) and M3 the worse (0.08), obtaining a total TI MAE of 0.06 taking into account the three locations. ME values register an underestimation in M1 and M3. This statistical measure is especially useful for analyzing this variable because a negative ME result can mean that the simulation is not resolving with enough energy the turbulent phenomena which meteorological stations are capturing. This is something common in this kind of LES-RW spectral energy analysis, previous studies at this resolution reveal a similar tendency [126, 125]. TI from Equation 6.1 does not take into account any eddy smaller than the resolution of d05 (98 m), leaving the last part of the wind energy spectrum (Figure 1.4, Chapter 1) to the parameterized TIsgs which is not capable of capturing the whole the range of microscale phenomena from the smaller eddies. However, taking these limitations into account, a total ME deviation of -0.02 can be considered as ans accurate result. Overall, ME, MAE and RMSE reflect reasonably good results for the TI forecasted by LES-RW.

As described in 6.2.2, TI measured from LES-RW is the sum of the TI explicitly resolved by the model (TI_{LES}) and TI diagnosed by the subgrid-scale parameterization (TI_{SGS}). The first term is the result of the TKE produced by the larger eddies and the second is the TKE which represents the smaller motions. In order to analyze in more detail the behavior of these variables, the next figure displays the plot series for TI_{Tot}, TI_{SGS} and TI_{LES} in MET3.

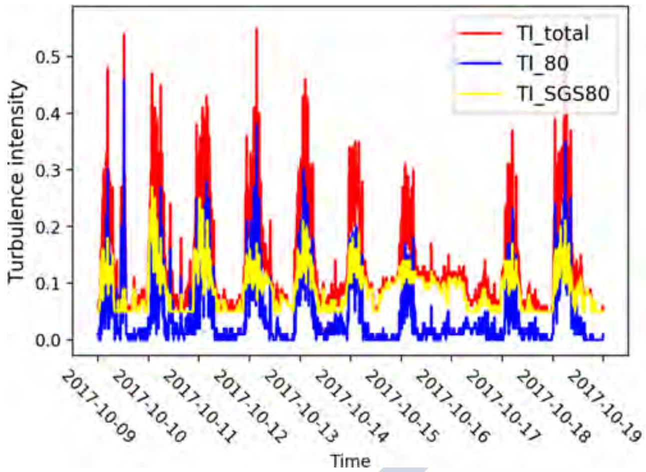

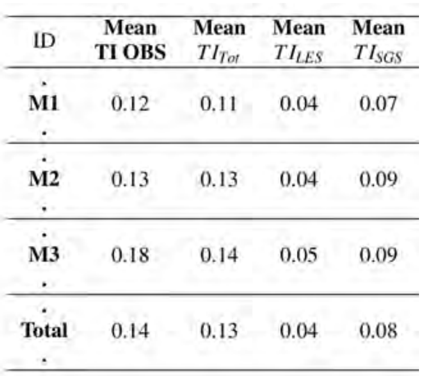

ID	Mean TI OBS	Mean TI_{Tot}	Mean TI_{LES}	Mean TI_{SGS}
M1	0.12	0.11	0.04	0.07
M2	0.13	0.13	0.04	0.09
M3	0.18	0.14	0.05	0.09
Total	0.14	0.13	0.04	0.08

Figure 6.7: (a) 2017/10/09-2017/10/19 (UTC) TI_{Tot} (red), TI_{LES} (blue) and TI_{SGS} (yellow) at M1 (80 meters height) for WRF-LES (blue) and observations (red)

Table 6.7: Mean values for TI_{obs}, TI_{Tot}, TI_{LES} and TI_{SGS} for the period studied in M1, M2, and M3.

The decomposition of TI in Figure 6.7 allows us to see the role of each part of TI throughout the 10 day period. TI_{LES} is clearly more present during the daytime, representing most of the TI_{Tot} registered during that part of the day. These periods are also the moments of the study with higher observed TI due to the influence of thermal interaction with the surface. TI_{SGS}, however, follows a different pattern. The subgrid-scale part of TI is present during the whole period. It represents the smaller eddies which affect the area in practically every moment of the day, without significant differences between day and night. The mean values in Table 6.7 highlight the importance of both sources of turbulence. The three stations register similar values, leaving a total mean amount of 66 % of TI_{Tot} coming from the smaller eddies ($<$ 98m) estimated by TIsgs. It is evident that the primary objective of the TI forecasting is to achieve realistic results with small mean error, but, apart from this, being also able to characterize two different sources of turbulent kinetic energy with this method gives added values to this kind of tool.

After the quantitative analysis of the capacities of RW-LES solving the turbulence which affects the validation points, we finish with this chapter, showing a qualitative view of the behavior of RW-LES flows along d05 domain. In particular, Figure 6.8 displays a vertical and a horizontal cut for each of the wind component (U, V and W) in a low wind instant the day after the studied period.

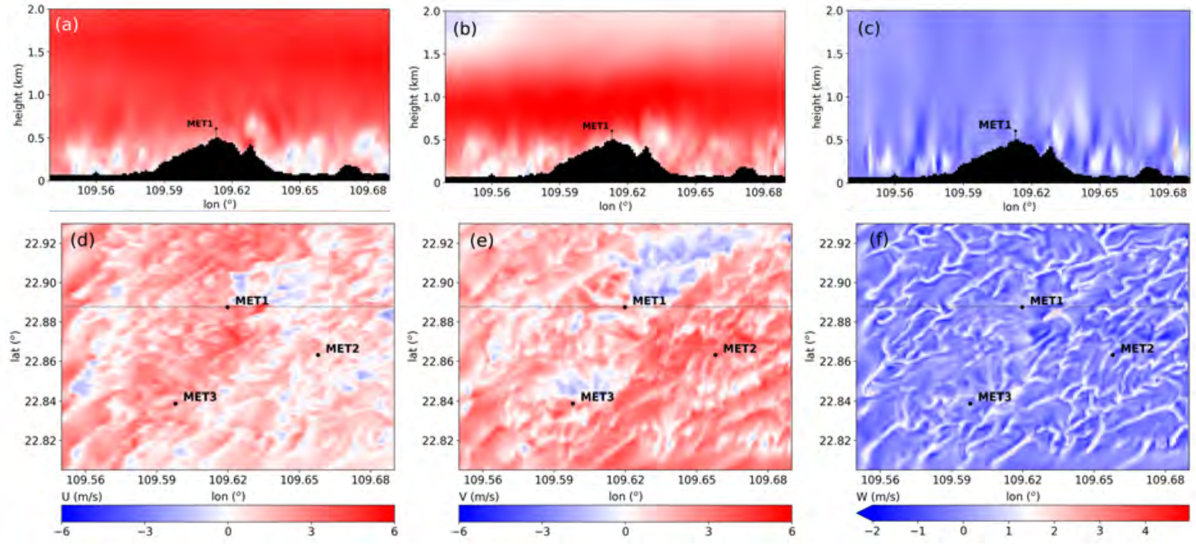

Figure 6.8: Instantaneous wind components at 2017-10-20 09:00 UTC for d05. (a) U plot along a longitudinal cut through M1. (b) Same as (a) for V component, (c) Same as (a) for W component. (d) U field at 80 m height. (e) V field at 80 m height. (f) W field at 80 m height.

The general perspective of all the composition of pictures shows a clear turbulent regime in all the images. Vertical cuts depict turbulent structures in most of the longitudes of the cut drawing the end of the mixing layer around 500 meters height at that moment. U and V vertical plots present several convective rolls at right and left of the center elevation. These updraft and downdrafts motions which are related to thermal fluxes are also clearly visible in the W vertical cut. Focusing on the horizontal cut, we can distinguish turbulent structures throughout most of the domain in the three representations. The SW prevailing wind interacts with the orography of the region producing microscale wind fields of different sizes. We can see how, for example, the NE area which surrounds M1 is affected by a NE wind flow (blue area in Figure 6.8d and e) helped by the small mountain where M1 is located. The horizontal W representation in Figure 6.8f has a different aspect as U and V plots. It has finer structures which represent positive vertical winds resulting from the combination of thermal terrain-lower PBL interactions and wind field accelerations due to the complexity of the topography.

Conclusions

The objective of this study was to develop a tool to analyze and characterize microscale phenomena in wind farm areas by using WRF-LES simulations. The model has been configured to simulate this type of simulations at very high resolution, a computational time optimization, and different numerical stability techniques were necessary to achieve that objective. The results have been tested using observational data from three different locations in the area. The following is a summary of the main conclusions to be drawn from experience.

With LES-RW simulations we have sought to obtain accurate wind module, wind direction and turbulent intensity results in the wind farm area studied. The strong points of these simulations are related to their high horizontal and vertical resolution. Reaching this very high resolution, deactivating the PBL parameterization of the simulation and by selecting the appropriate settings, we are able to dynamically reproduce a large part of the turbulent phenomenology of the studied zones. The vertical resolution also acquires particular importance as it affects wind and temperature calculations in the lowest part of the PBL.

A zonal smoothing tool was developed to avoid problems of instability due to the complex terrain. This method looks for the points of numerical instability in the domain and modifies the orography data around them. This gives stability to the simulation, modifying the domain as little as possible. The results have been very satisfactory; the zonal smoothing has been used successfully in several portions of the domain, making the simulations more stable and reducing computational time.

Wind speed forecasting evaluation leaves a total MAE of 1.89 m/s. Excellent results in M2 and M3, and a prominent overestimation in M1 which seems to be related to some incorrect height data at the north/northeast of the point. RW-LES has accurately reproduced wind direction motion during the 10-day experiment, as the total MAE indicates (17.49°). The small errors yielded by the model in the temperature validation at 10 m height (MAE = 1.35 K and ME= -0.45 K) reflect a good reproduction of the thermal fluxes near surface which have a major impact on the correct reproduction of the microscale wind behavior.

TI measured from LES-RW was obtained from the sum of the TI explicitly resolved by the model and TKE diagnosed by the subgrid-scale parameterization (TI_{SGS}). TI results in the three validation points present a realistic performance of microscale phenomena by RW-LES, which achieves a total MAE of 0.06 and just a slight mean underestimation (ME=-0.02). Moreover, this method to estimate TI, allows us to characterize two different sources of turbulence adding extra value to the study. The qualitative analysis of the RW-LES displayed in horizontal and vertical wind field plots show realistic microscale flow all along the domain.

We can conclude that the experience with LES-RW simulations has been satisfactory. It has also become clear that the use of WRF-LES as an operational tool requires a high technical level and significant computing resources. There are many lines of improvement on which we can continue working to make this tool more competitive regarding time and stability. In any case, it can be affirmed WRF-LES is a current and future tool within the wind industry. Throughout this experience, we have seen that WRF-LES is a field in continuous growth, with constant new developments and improvements in parameterizations in recent years. To this, must be added the exponential increase of the computing capacity, which allows ever quicker simulation and at a lower price. All this context promotes new ways of using this type of modeling tools, new products with promising uses in the sector.


USC
UNIVERSIDADE
DE SANTIAGO
DE COMPOSTELA

Chapter 7

Main Conclusions

The objective of this thesis has been the achievement of an improvement in the quantification and understanding of some of the main interactions between the atmospheric planetary boundary layer and the terrain, focusing on the behavior of wind flows at different scales. We intend to improve the tools, within numerical modeling, for the analysis of such mechanisms, contributing in this manner to the optimization of wind resource use. Throughout the thesis, we have addressed different topics within this field, starting from wind resource forecasting and nowcasting, continuing with the wind turbines wakes and extreme events studies and finishing with the microscale phenomena analysis in a wind farm area. The main conclusions reached from this thesis are summarized in the next points:

- Wind resource forecasting is one of the main duties in daily wind farm operation. The WRF atmospheric model at high resolution has been tested for this purpose in a real wind farm over complex terrain. Results show that WRF yields good wind power operational predictions for this kind of wind farm, due to a good representation of the planetary boundary layer behavior of the region and the excellent performance of the Fitch scheme (wind turbine scheme) under these conditions. The study supports the concept of utilizing WRF high-resolution simulations as part of a wind speed and energy forecast tool within the wind energy industry.

- The combination of the WRF model with a post-process technique which combines a non-linear Kalman filter and a Bayesian model has allowed us to perform very short-term wind predictions (nowcasting). The method obtains large improvements in wind speed and direction nowcasting with respect to the original forecast in different meteorological situations throughout an entire year. The accuracy and reliability of the results demonstrate the potential utility that this tool can have for a variety of applications in wind farm operations and energy markets.

- The wind turbine wake effects present a reduction in the power output and the increased level of turbulent loads over the downstream turbines. The two Annual Wake analyses performed in this thesis show considerable wind resource losses among wind turbines in several directions and extensive wake effects all around the wind farm. This new technique can help to analyze beforehand the total impact of a future neighboring wind farm construction on an existent wind farm's annual production and provide valuable information to optimize new farm designs.

- Some extreme wind events such as downslope wind storms, which are highly dependent on local orographic forcings, can have significant impacts on operative wind farms. WRF high-resolution simulations have been used to analyze one of these events in a big wind farm cluster in Mexico. The study reveals a significant fine-scale structure in the strong Tehuano wind flow depending on the Froude number; calculated upstream the topographic barrier that the wind crosses. The model accurately represents spatially heterogeneous intense downslope windstorm and hydraulic jumps for several hours, obtaining low errors in wind speed, wind direction, and temperature.

- The microscale phenomena analysis is always a point of interest within the wind industry. WRF Large Eddy Simulations (LES) are presented as a reliable tool for this issue due to its capacity for resolving an important part of the turbulent wind spectrum phenomena. The experiment performed on a real wind farm in China shows that LESs reach realistic Turbulent Intensity and wind representations, obtaining low errors at all the validation points used.

This thesis has tackled several issues related with wind phenomenology at the meso and microscale and its implications in the wind energy field. The experience has been successful, not only the results and conclusions, but also for the paths left open in the addressed field. New opportunities have become evident. Wind energy is just an example of the importance of the study of the atmosphere, the air layer that supports life on the Earth. The scientific community has the responsibility of continuing with the search for answers explaining the atmospheric processes that surround us. For that, it is crucial for researchers to work collaboratively more than ever, joining forces in ambitious common plans, keeping scientific tools alive in open-access communities and sharing knowledge between international agencies and research groups.

Chapter 8

Bibliography

[1] G. A. Heath, P. O'Donoughue, D. J. Arent, and M. Bazilian, "Harmonization of initial estimates of shale gas life cycle greenhouse gas emissions for electric power generation," *Proceedings of the National Academy of Sciences*, vol. 111, no. 31, pp. E3167–E3176, 2014.

[2] S. Review, "Life Cycle Greenhouse Gas Emissions of Coal-Fired Electricity Generation," vol. 16, 2012.

[3] C. Kaito, A. Ito, S. Kimura, Y. Kimura, Y. Saito, and T. Nakada, *Topotactical growth of indium sulfide by evaporation of metal onto molybdenite*, 2000, vol. 218, no. 2.

[4] United Nations, "Convention on Climate Change: Climate Agreement of Paris." pp. 1–27, 2015.

[5] P. Karnoe, "Wind Energy in America: A History," pp. 417–419, 1999.

[6] J. K. Kaldellis and D. Zafirakis, "The wind energy (r)evolution: A short review of a long history," *Renewable Energy*, vol. 36, no. 7, pp. 1887–1901, 2011.

[7] W. Scheuermann, D. Grafnetter, E. Ostor-Lamm, E. Nussel, and M. Ganowa, "Blood thiocyanate levels and self-reported smoking habits compared in two large cardiovascular population studies." *Cor et vasa*, vol. 33, no. 2, pp. 150–161, 1991.

[8] S. Sawyer, S. Teske, and M. Dyrholm, "The Global Wind Energy Outlook," *Gwec*, 2016.

[9] Wind Europe, "Wind in power 2016 European Statistics," *EWEA European statistics*, no. February, pp. 1–12, 2016.

[10] Asociación Empresarial Eólica 2016, "The voice of the sector," Tech. Rep., 2016.

[11] Global Wind Energy Council, "Global wind report," Global Wind Energy Council, Tech. Rep., 2017.

[12] L. Fried, S. Shukla, and S. Sawyer, *Growth Trends and the Future of Wind Energy*. Elsevier Inc., 2017.

[13] B. Valpy, G. Hundleby, K. Freeman, A. Roberts, and A. Logan, "Future renewable energy costs: Offshore wind," InnoEnergy, Tech. Rep., 2017.

[14] J. M. Guerrero, C. Lumbreras, D. D. Reigosa, P. Garcia, and F. Briz, “Control and Emulation of Small Wind Turbines Using Torque Estimators,” *IEEE Transactions on Industry Applications*, vol. 53, no. 5, pp. 4863–4876, 2017.

[15] D. Jesús and Y. Villarreal, “VIV resonant wind generators,” vol. 2, no. 1, pp. 1–6, 2018.

[16] Norvento S.L.U., “Aerogenerador nED100,” Tech. Rep., 2017.

[17] I. Van der Hoven, “Power spectrum of horizontal wind speed in the frequency range from 0.0007 to 900 cycles per hour,” *Journal of Meteorology*, vol. 14, pp. 160–164, 1957.

[18] M. A. Escalante Soberanis and W. Mérida, “Regarding the influence of the Van der Hoven spectrum on wind energy applications in the meteorological mesoscale and microscale,” *Renewable Energy*, vol. 81, pp. 286–292, 2015.

[19] K. E. Trenberth, “The definition of {El} {Niño},” *Bull. Amer. Meteorol. Soc.*, vol. 78, no. August, pp. 2771–2777, 1997.

[20] J. D. Mirocha, M. J. Churchfield, D. Muñoz-Esparza, R. K. Rai, Y. Feng, B. Kosović, S. E. Haupt, B. Brown, B. L. Ennis, C. Draxl, J. Sanz Rodrigo, W. J. Shaw, L. K. Berg, P. J. Moriarty, R. R. Linn, V. R. Kotamarthi, R. Balakrishnan, J. W. Cline, M. C. Robinson, and S. Ananthan, “Large-Eddy Simulation Sensitivities to Variations of Configuration and Forcing Parameters in Canonical Boundary-Layer Flows for Wind Energy Applications,” *Wind Energy Science Discussions*, pp. 1–40, 2017.

[21] National Renewable Energy Laboratory NREL, “Renewable Electricity Futures Study: Renewable Electricity Generation and Storage Technologies: Volume 2 of 4,” *Renewable Electricity Futures Study: Renewable Electricity Generation and Storage Technologies, Volume 2*, vol. 2, pp. 185–188, 2012.

[22] C. M. Wyman and C. J. Jablonowski, “A Workflow and Estimate for the Economic Viability of Offshore Wind Projects,” *Wind Engineering*, vol. 39, no. 5, pp. 579–594, 2015.

[23] E. Y. T. MINISTERIO DE INDUSTRIA, “Real Decreto 413/2014, de 6 de junio. DISPOSICIONES GENERALES,” p. 43876, 2014.

[24] Boletín Oficial del Estado (B.O.E.), “Ley 8/2009, de 22 de diciembre, por la que se regula el aprovechamiento eólico en Galicia y se crean el canon eólico y el Fondo de Compensación Ambiental,” pp. 9842–9863, 2010.

[25] F. Flores, R. Garreaud, and R. C. Muñoz, “CFD simulations of turbulent buoyant atmospheric flows over complex geometry: Solver development in OpenFOAM,” *Computers and Fluids*, vol. 82, pp. 1–13, 2013.

[26] N. Lukač, G. Štumberger, and B. Žalik, “Wind resource assessment using airborne LiDAR data and smoothed particle hydrodynamics,” *Environmental Modelling and Software*, vol. 95, pp. 1–12, 2017.

[27] C. Ferreira, J. Gama, L. Matias, A. Botterud, J. Wang, and (INESC Porto), “A survey on wind power ramp forecasting.” U.S. Departament of Energy, Tech. Rep. 1, 2010.

[28] D. R. Drew, D. J. Cannon, J. F. Barlow, P. J. Coker, and T. H. Frame, “The importance of forecasting regional wind power ramping: A case study for the UK,” *Renewable Energy*, vol. 114, pp. 1201–1208, 2017.

[29] M. Prósper, O. C. Carlos, F. Canoura Fernández, and G. Miguez-Macho, “Wind power forecasting for a real onshore wind farm on complex terrain using WRF high resolution simulations,” *Renewable Energy*, pp. 1–22, 2018.

[30] P. Dvorak, “How turbulent winds abuse wind turbine drivetrains,” vol. 7, pp. 1–7, 2015.

[31] G. Galanis, E. Papageorgiou, and A. Liakatas, “A hybrid Bayesian Kalman filter and applications to numerical wind speed modeling,” *Journal of Wind Engineering and Industrial Aerodynamics*, vol. 167, no. November 2015, pp. 1–22, 2017.

[32] W. C. Skamarock, J. B. Klemp, J. Dudhia, D. O. Gill, D. M. Barker, M. G. Duda, X.-y. Huang, W. Wang, J. G. Powers, and M. M. Division, “A Description of the Advanced Research WRF Version 3,” no. June, 2008.

[33] W. Wang, C. Bruyère, M. Duda, J. Dudhia, D. Gill, M. Kavulich, K. Keene, H.-C. Lin, J. Michalakes, S. Rizvi, X. Zhang, J. Berner, and K. Smith, “ARW Version 3 Modeling System User’s Guide,” *Journal of Palestine Studies*, vol. 37, no. 1, pp. 204–205, 2007.

[34] M. Division and O. Sciences, “Parameterization of Wind Farms in Climate Models,” pp. 6439–6458, 2013.

[35] M. Division, O. Sciences, and N. Renewable, “Mesoscale Influences of Wind Farms throughout a Diurnal Cycle,” no. 2005, pp. 2173–2198, 2013.

[36] R. K. Rai, L. K. Berg, B. Kosović, J. D. Mirocha, M. S. Pekour, and W. J. Shaw, “Comparison of Measured and Numerically Simulated Turbulence Statistics in a Convective Boundary Layer Over Complex Terrain,” *Boundary-Layer Meteorology*, vol. 163, no. 1, pp. 69–89, 2017.

[37] C. H. Moeng and P. P. Sullivan, “A comparison of shear-and buoyancy-driven planetary boundary layer flows,” *Journal of the Atmospheric Sciences*, pp. 193–207, 1994.

[38] A. Chaudhari, A. Hellsten, and J. Hämäläinen, “Full-Scale Experimental Validation of Large-Eddy Simulation of Wind Flows over Complex Terrain: The Bolund Hill,” *Advances in Meteorology*, vol. 2016, pp. 1–25, 2016.

[39] B. J. Vanderwende, B. Kosović, J. K. Lundquist, and J. D. Mirocha, “Simulating effects of a wind turbine array using LES and RANS,” *Journal of Advances in Modeling Earth Systems*, vol. 8, no. 3, pp. 1376–1390, 2016.

[40] J. D. Mirocha, B. Kosovic, M. L. Aitken, and J. K. Lundquist, “Implementation of a generalized actuator disk wind turbine model into the weather research and forecasting model for large-eddy simulation applications,” *Journal of Renewable and Sustainable Energy*, vol. 6, no. 1, 2014.

[41] M. L. Aitken, B. Kosović, J. D. Mirocha, and J. K. Lundquist, "Large eddy simulation of wind turbine wake dynamics in the stable boundary layer using the Weather Research and Forecasting Model," *Journal of Renewable and Sustainable Energy*, vol. 6, no. 3, 2014.

[42] J. Zhao, Z. H. Guo, Z. Y. Su, Z. Y. Zhao, X. Xiao, and F. Liu, "An improved multi-step forecasting model based on WRF ensembles and creative fuzzy systems for wind speed," *Applied Energy*, vol. 162, pp. 808–826, 2016.

[43] Y. Li, C. Dai, W. Tongxun, Z. Zhou, S. Zhou, L. Cai, P. Musilek, and E. Lozowski, "Separate wind power and ramp predictions based on meteorological variables and clustering method," *2016 IEEE 6th International Conference on Power Systems, ICPS 2016*, 2016.

[44] Y. Che, X. Peng, L. Delle Monache, T. Kawaguchi, and F. Xiao, "A wind power forecasting system based on the weather research and forecasting model and Kalman filtering over a wind-farm in Japan," *Journal of Renewable and Sustainable Energy*, vol. 8, no. 1, 2016.

[45] Y. Che and F. Xiao, "An integrated wind-forecast system based on the weather research and forecasting model, Kalman filter, and data assimilation with nacelle-wind observation," vol. 053308, 2016.

[46] M. M. Division, O. Sciences, N. Renewable, M. M. Division, and N. Renewable, "Local and Mesoscale Impacts of Wind Farms as Parameterized in a Mesoscale NWP Model," no. 2005, pp. 3017–3038, 2012.

[47] B. Vanderwende and J. K. Lundquist, "Could Crop Height Affect the Wind Resource at Agriculturally Productive Wind Farm Sites?" *Boundary-Layer Meteorology*, vol. 158, no. 3, pp. 409–428, 2016.

[48] A. C. Fitch, "Climate impacts of large-scale wind farms as parameterized in a global climate model," *Journal of Climate*, vol. 28, no. 15, pp. 6160–6180, 2015.

[49] J. K. Lundquist, J. C-Y Lee, C. Draxl, P. Moriarty, S. Ananthan, F. Zhang, and H. Li, "Can Wind Farms in Inner Mongolia Affect the Air Quality in Beijing?" no. April, 2016.

[50] R. Vautard, F. Thais, I. Tobin, F.-M. Bréon, J.-G. D. de Lavergne, A. Colette, P. Yiou, and P. M. Ruti, "Regional climate model simulations indicate limited climatic impacts by operational and planned European wind farms," *Nature Communications*, vol. 5, pp. 1–9, 2014.

[51] S. Santoni, C., Garcia-Cartagena, E. J., Iungo, G. V., Leonardi, "Coupling of mesoscale Weather Research and Forecasting model to a high fidelity Large Eddy Simulation," *Journal of Physics: Conference Series*, vol. 1037, p. 062010, 2018.

[52] G. Xia, M. C. Cervarich, S. B. Roy, L. Zhou, J. R. Minder, P. A. Jimenez, and J. M. Freedman, "Simulating Impacts of Real-World Wind Farms on Land Surface Temperature Using the WRF Model: Validation with Observations," *Monthly Weather Review*, vol. 145, no. 12, pp. 4813–4836, 2017.

[53] R. Kumar, T. Stallard, and P. Stansby, “Assessment of WRF prediction of velocity profile and turbulence intensity by comparison to field measurement,” *Proceedings of the International Offshore and Polar Engineering Conference*, no. June, 2017.

[54] P. A. Jiménez, J. Navarro, A. M. Palomares, and J. Dudhia, “Mesoscale modeling of offshore wind turbine wakes at the wind farm resolving scale: a composite-based analysis with the Weather Research and Forecasting model over Horns Rev,” no. February 2014, pp. 559–566, 2015.

[55] A. M. P. Pedro A. Jiménez, Jorge Navarro and J. Dudhia, “Mesoscale modeling of offshore wind turbine wakes at the wind farm resolving scale: a composite-based analysis with the Weather Research and Forecasting model over Horns Rev,” *Wind Energy*, vol. 17, no. December 2013, pp. 657–669, 2013.

[56] O. Eriksson, M. Baltscheffsky, S. P. Breton, S. Söderberg, and S. Ivanell, “The Long distance wake behind Horns Rev i studied using large eddy simulations and a wind turbine parameterization in WRF,” *Journal of Physics: Conference Series*, vol. 854, no. 1, 2017.

[57] O. Eriksson, J. Lindvall, S. P. Breton, and S. Ivanell, “Wake downstream of the Lillgrund wind farm - A Comparison between les using the actuator disc method and a Wind farm Parametrization in WRF,” *Journal of Physics: Conference Series*, vol. 625, no. 1, 2015.

[58] P. J. Volker, J. Badger, A. N. Hahmann, and S. Ott, “The explicit wake parametrisation V1.0: A wind farm parametrisation in the mesoscale model WRF,” *Geoscientific Model Development*, vol. 8, no. 11, pp. 3715–3731, 2015.

[59] S. C. Pryor, R. J. Barthelmie, and T. J. Shepherd, “The Influence of Real-World Wind Turbine Deployments on Local to Mesoscale Climate,” *Journal of Geophysical Research: Atmospheres*, vol. 123, no. 11, pp. 5804–5826, 2018.

[60] Y. J. Kim, “Downstream effects from contemporary wind turbine deployments Downstream deployments effects from contemporary wind turbine,” 2018.

[61] J. A. Santos, C. Rochinha, M. L. R. Liberato, M. Reyers, and J. G. Pinto, “Projected changes in wind energy potentials over Iberia,” *Renewable Energy*, vol. 75, no. 2015, pp. 68–80, 2015.

[62] R. Lorente-Plazas, J. P. Montávez, P. A. Jimenez, S. Jerez, J. J. Gómez-Navarro, J. A. García-Valero, and P. Jimenez-Guerrero, “Characterization of surface winds over the Iberian Peninsula,” *International Journal of Climatology*, vol. 35, no. 6, pp. 1007–1026, 2015.

[63] Ecotèctnia, “Technical Report 74 1.6,” ECOTÈCNIA, s.coop.c.l., Tech. Rep., 2007.

[64] T. T. Warner, “Quality assurance in atmospheric modeling,” *Bulletin of the American Meteorological Society*, vol. 92, no. 12, pp. 1601–1610, 2011.

[65] European Environment Agency, *CLC2006 technical guidelines*, 2007, vol. 2010, no. 17.

[66] J. A. Slater, B. Heady, G. Kroenung, W. Curtis, J. Haase, D. Hoegemann, C. Shockley, and K. Tracy, “Evaluation of the New ASTER Global Digital Elevation Model,” vol. 77, no. 4, pp. 335–349, 2009.

[67] H. H. Shin, S.-Y. Hong, and J. Dudhia, “Impacts of the Lowest Model Level Height on the Performance of Planetary Boundary Layer Parameterizations,” *Monthly Weather Review*, vol. 140, no. 2, pp. 664–682, 2012.

[68] E. J. Mlawer, S. J. Taubman, P. D. Brown, M. J. Iacono, and S. A. Clough, “Radiative transfer for inhomogeneous atmospheres: RRTM, a validated correlated-k model for the longwave,” *Journal of Geophysical Research: Atmospheres*, vol. 102, no. D14, pp. 16 663–16 682, 1997.

[69] J. Dudhia, “Numerical Study of Convection Observed during the Winter Monsoon Experiment Using a Mesoscale Two-Dimensional Model,” pp. 3077–3107, 1989.

[70] S. Hong and J. Lim, “The WRF single-moment 6-class microphysics scheme (WSM6),” pp. 129–151, 2006.

[71] M. Tewari, F. Chen, W. Wang, J. Dudhia, M. A. Lemone, K. Mitchell, R. H. Cuenca, C. Springs, A. Force, and W. Agency, “Implementation and Verification of The Unified NOAH Land Surface Model In The WRF Model,” *20th Conference on Weather Analysis and Forecasting/16th Conference on Numerical Weather Prediction*, 2004.

[72] M. Nakanishi and H. Niino, “An improved Mellor-Yamada Level-3 model: Its numerical stability and application to a regional prediction of advection fog,” *Boundary-Layer Meteorology*, vol. 119, no. 2, pp. 397–407, 2006.

[73] J. S. Kain, “The Kain–Fritsch Convective Parameterization: An Update,” *Journal of Applied Meteorology*, vol. 43, no. 1, pp. 170–181, 2004.

[74] A. A. Wyszogrodzki, Y. Liu, N. Jacobs, P. Childs, Y. Zhang, G. Roux, and T. T. Warner, “Analysis of the surface temperature and wind forecast errors of the NCAR-AirDat operational CONUS 4-km WRF forecasting system,” *Meteorology and Atmospheric Physics*, vol. 122, no. 3-4, pp. 125–143, 2013.

[75] D. Pozo, J. C. Marín, L. Illanes, M. Curé, and D. Rabanus, “Validation of WRF forecasts for the Chajnantor region,” *Monthly Notices of the Royal Astronomical Society*, vol. 459, no. 1, pp. 419–426, 2016.

[76] J. Zhao, Y. Guo, X. Xiao, J. Wang, D. Chi, and Z. Guo, “Multi-step wind speed and power forecasts based on a WRF simulation and an optimized association method,” *Applied Energy*, vol. 197, pp. 183–202, 2017.

[77] B. Pokharel, B. Geerts, X. Chu, and P. Bergmaier, “Profiling radar observations and numerical simulations of a downslopewind storm and rotor on the lee of the Medicine Bow mountains in Wyoming,” *Atmosphere*, vol. 8, no. 2, 2017.

[78] G. M. Wang, D. F. Liu, Y. P. Xu, T. Meng, and F. Zhu, “PET/CT imaging in diagnosing lymph node metastasis of esophageal carcinoma and its comparison with pathological

findings," *European Review for Medical and Pharmacological Sciences*, vol. 20, no. 8, pp. 1495–1500, 2016.

[79] M. O. Mughal, M. Lynch, F. Yu, and J. Sutton, "Forecasting and verification of winds in an East African complex terrain using coupled mesoscale - And micro-scale models," *Journal of Wind Engineering and Industrial Aerodynamics*, vol. 176, no. December 2017, pp. 13–20, 2018.

[80] C. L. Archer, H. P. Simão, W. Kempton, W. B. Powell, and M. J. Dvorak, "The challenge of integrating offshore wind power in the U.S. electric grid. Part I: Wind forecast error," *Renewable Energy*, vol. 103, pp. 346–360, 2017.

[81] D. Muñoz-Esparza, J. K. Lundquist, J. A. Sauer, B. Kosović, and R. R. Linn, "Coupled mesoscale-LES modeling of a diurnal cycle during the CWEX-13 field campaign: From weather to boundary-layer eddies," *Journal of Advances in Modeling Earth Systems*, vol. 9, no. 3, pp. 1572–1594, 2017.

[82] D. Muñoz-Esparza, B. Kosović, J. Mirocha, and J. van Beeck, "Bridging the Transition from Mesoscale to Microscale Turbulence in Numerical Weather Prediction Models," *Boundary-Layer Meteorology*, vol. 153, no. 3, pp. 409–440, 2014.

[83] M. Huang, Y. Wang, W. Lou, and S. Cao, "Multi-scale simulation of time-varying wind fields for Hangzhou Jiubao Bridge during Typhoon Chan-hom," *Journal of Wind Engineering and Industrial Aerodynamics*, vol. 179, no. April, pp. 419–437, 2018.

[84] G. N. Kariniotakis and P. Pinson, "Evaluation of the MORE-CARE wind power prediction platform. Performance of the fuzzy logic based models," no. June, 2003.

[85] G. Kariniotakis, I. Martí, D. Casas, P. Pinson, T. S. Nielsen, H. Madsen, G. Giebel, J. Usaola, and I. Sanchez, "What performance can be expected by short-term wind power prediction models depending on site characteristics ?" *EWC 2004 Conference*, pp. 22–25, 2004.

[86] E. Vanem, "Long-term time-dependent stochastic modelling of extreme waves," *Stochastic Environmental Research and Risk Assessment*, vol. 25, no. 2, pp. 185–209, 2011.

[87] G. Giebel, *On the benefits of distributed generation of wind energy in Europe, PhD thesis from the Carl von Ossietzky Universitat Oldenburg*, E. . Fortschritt-Berichte VDI. Reihe 6, Ed., Dusseldorf, Germany, 2001, no. August.

[88] G. Resconi, "Geometry of risk analysis (morphogenetic system)," *Stochastic Environmental Research and Risk Assessment*, vol. 23, no. 4 SPEC. ISS., pp. 425–432, 2009.

[89] P. S, G. G, and G. Kallos, "Solar and photovoltaic forecasting through post-processing of the global environmental multiscale numerical weather prediction model," *Progress in Photovoltaics: Research and Applications*, 2011.

[90] G. Galanis, P. Louka, P. Katsafados, I. Pytharoulis, and G. Kallos, “Applications of Kalman filters based on non-linear functions to numerical weather predictions,” *Annales Geophysicae*, vol. 24, no. 10, pp. 2451–2460, 2006.

[91] G. Galanis, G. Emmanouil, P. C. Chu, and G. Kallos, “A new methodology for the extension of the impact of data assimilation on ocean wave prediction,” *Ocean Dynamics*, vol. 59, no. 3, pp. 523–535, 2009.

[92] P. Crochet, “Adaptive Kalman filtering of 2-metre temperature and 10-metre wind-speed forecasts in Iceland,” *Meteorological Applications*, vol. 11, no. 2, pp. 173–187, 2004.

[93] G. Galanis and M. Anadranistakis, “A one-dimensional Kalman filter for the correction of near surface temperature forecasts,” *Meteorological Applications*, vol. 9, no. 4, pp. 437–441, 2002.

[94] E. Kalnay, *Atmospheric modeling, data assimilation, and predictability*, 2003.

[95] R. E. Kalman and R. S. Bucy, “New Results in Linear Filtering and Prediction Theory,” *Journal of Basic Engineering*, vol. 83, no. 1, p. 95, 1961.

[96] R. E. Kalman, “A New Approach to Linear Filtering and Prediction Problems,” *Journal of Basic Engineering*, vol. 82, no. 1, p. 35, 1960.

[97] C. Stathopoulos, A. Kaperoni, G. Galanis, and G. Kallos, “Wind power prediction based on numerical and statistical models,” *Journal of Wind Engineering and Industrial Aerodynamics*, vol. 112, pp. 25–38, 2013.

[98] S. Hua, S. Wang, S. Jin, S. Feng, and B. Wang, “Wind speed optimisation method of numerical prediction for wind farm based on Kalman filter method,” *The Journal of Engineering*, vol. 2017, no. 13, pp. 1146–1149, 2017.

[99] P. Louka, G. Galanis, N. Siebert, G. Kariniotakis, P. Katsafados, I. Pytharoulis, and G. Kallos, “Improvements in wind speed forecasts for wind power prediction purposes using Kalman filtering,” *Journal of Wind Engineering and Industrial Aerodynamics*, vol. 96, no. 12, pp. 2348–2362, 2008.

[100] A. Zaher, S. D. McArthur, D. G. Infield, and Y. Patel, “Online wind turbine fault detection through automated SCADA data analysis,” *Wind Energy*, vol. 12, no. 6, pp. 574–593, 2009.

[101] W. Skamarock, J. Klemp, J. Dudhi, D. Gill, D. Barker, M. Duda, X.-Y. Huang, W. Wang, and J. Powers, “A Description of the Advanced Research WRF Version 3,” NCAR, Tech. Rep. June, 2008.

[102] A. C. Beljaars, “The parametrization of surface fluxes in largescale models under free convection,” *Quarterly Journal of the Royal Meteorological Society*, vol. 121, no. 522, pp. 255–270, 1995.

[103] P. Patlakas, E. Drakaki, G. Galanis, C. Spyrou, and G. Kallos, “Wind gust estimation by combining a numerical weather prediction model and statistical post-processing,” in *Energy Procedia*, vol. 125. Elsevier B.V., 2017, pp. 190–198.

[104] T. G. Box G., *Bayesian Inference in Statistical Analysis*, J. Wiley and Sons, Eds., John Wiley and Sons. INC New York, USA, 1992.

[105] J. Bernardo and A. Smith, *Bayesian Theory*, John Wiley and Sons. INC New York, USA, 2000.

[106] I. Kuikka, "Wind Nowcasting: Optimizing runway in use," Tech. Rep., 2009.

[107] H. Utsumi, T. Misaka, and W. Moteki, "Prediction Model of Internal Relative Humidity During Self-desiccation in Hardened Cement Pastes," *Concrete Research and Technology*, vol. 26, no. 3, pp. 11–19, 2015.

[108] M. T. Van Dijk, J. W. Van Wingerden, T. Ashuri, Y. Li, and M. A. Rotea, "Yaw-Misalignment and its Impact on Wind Turbine Loads and Wind Farm Power Output," in *Journal of Physics: Conference Series*, vol. 753, no. 6, 2016.

[109] M. Churchfield and P. Fleming, "Wind Turbine Wake-Redirection Control at the Fishermen's Atlantic City Windfarm," *Offshore Technology* . . . , no. May, 2015.

[110] P. Mckay, "Group Dynamics of Commercial Scale Wind Turbines," 2011.

[111] M. P. S. G. B. Sofia Elena Colescab, "Renewable and sustainable energy reviews," *Elsevier*, vol. 56, pp. 156–170, 2016.

[112] G. M. Wang, D. F. Liu, Y. P. Xu, T. Meng, and F. Zhu, "PET/CT imaging in diagnosing lymph node metastasis of esophageal carcinoma and its comparison with pathological findings," *European Review for Medical and Pharmacological Sciences*, vol. 20, no. 8, pp. 1495–1500, 2016.

[113] J. R. Marden, S. D. Ruben, and L. Y. Pao, "A model-free approach to wind farm control using game theoretic methods," *IEEE Transactions on Control Systems Technology*, vol. 21, no. 4, pp. 1207–1214, 2013.

[114] A. Alaimo, A. Esposito, A. Messineo, C. Orlando, and D. Tumino, "3D CFD analysis of a vertical axis wind turbine," *Energies*, vol. 8, no. 4, pp. 3013–3033, 2015.

[115] R. Krishnamurthy, S. Otarola-Bustos, and L. S. Leo, "WFIP2 project University of Notre Dame Halo Scanning Doppler LiDAR (lidar.z07) Quality Controlled Dataset ," pp. 1–11, 2017.

[116] J. Wilczak, C. Finley, J. Freedman, J. Cline, L. Bianco, J. Olson, I. Djalalova, L. Sheridan, M. Ahlstrom, J. Manobianco, J. Zack, J. R. Carley, S. Benjamin, R. Coulter, L. K. Berg, J. Mirocha, K. Clawson, E. Natenberg, and M. Marquis, "The wind forecast improvement project (WFIP): A public-private partnership addressing wind energy forecast needs," *Bulletin of the American Meteorological Society*, vol. 96, no. 10, pp. 1699–1718, 2015.

[117] L. Pan, Y. Liu, G. Roux, W. Cheng, Y. Liu, J. Hu, S. Jin, and S. Feng, "Seasonal variation of the surface wind forecast performance of the 3km-grid WRF-RTFDDA forecasting system over China ." Boulder, Colorado, 2018.

[118] C. Gong, "IEC International Standard 61400-1," *Order A Journal On The Theory Of Ordered Sets And Its Applications*, pp. 1–9, 2008.

[119] Y. Li, A. M. Castro, T. Sinokrot, W. Prescott, and P. M. Carrica, "Coupled multi-body dynamics and CFD for wind turbine simulation including explicit wind turbulence," *Renewable Energy*, vol. 76, pp. 338–361, 2015.

[120] S. C. Goh, S. R. Boopathy, C. Krishnaswami, and J. U. Schlüter, "Tow testing of Savonius wind turbine above a bluff body complemented by CFD simulation," *Renewable Energy*, vol. 87, pp. 332–345, 2016.

[121] A. Rezaeiha, I. Kalkman, and B. Blocken, "CFD simulation of a vertical axis wind turbine operating at a moderate tip speed ratio: Guidelines for minimum domain size and azimuthal increment," *Renewable Energy*, vol. 107, pp. 373–385, 2017.

[122] R. J. Beare, M. K. Macvean, A. A. M. Holtslag, J. Cuxart, I. Esau, J. C. Golaz, M. A. Jimenez, M. Khairoutdinov, B. Kosovic, D. Lewellen, T. S. Lund, J. K. Lundquist, A. McCabe, A. F. Moene, Y. Noh, S. Raasch, and P. Sullivan, "An intercomparison of large-eddy simulations of the stable boundary layer," *Boundary-Layer Meteorology*, vol. 118, no. 2, pp. 247–272, 2006.

[123] F. K. Chow, R. L. Street, M. Xue, and J. H. Ferziger, "Explicit Filtering and Reconstruction Turbulence Modeling for Large-Eddy Simulation of Neutral Boundary Layer Flow," *Journal of the Atmospheric Sciences*, vol. 62, no. 7, pp. 2058–2077, 2005.

[124] N. Zhang, X. Wang, and Z. Peng, "Large-Eddy Simulation of Mesoscale Circulations Forced by Inhomogeneous Urban Heat Island," *Boundary-Layer Meteorology*, vol. 151, no. 1, pp. 179–194, 2014.

[125] K. R. Raj, H. Gopalan, and J. W. Naughton, "Effects of spatial and temporal resolution of the turbulent inflow on wind turbine performance estimation," *Wind Energy*, vol. 20, no. 8, pp. 1495–1500, 2016.

[126] P. Doubrawa, A. Montornès, R. J. Barthelmie, S. C. Pryor, and P. Casso, "Analysis of Different Gray Zone Treatments in WRF-LES Real Case Simulations," *Wind Energy Science*, no. January, pp. 1–23, 2018.

[127] J. C. WYNGAARD, "Toward Numerical Modeling in the "Terra Incognita" JOHN," no. 2, pp. 3–4, 2004.

[128] G. M. Wang, D. F. Liu, Y. P. Xu, T. Meng, and F. Zhu, "PET/CT imaging in diagnosing lymph node metastasis of esophageal carcinoma and its comparison with pathological findings," *European Review for Medical and Pharmacological Sciences*, vol. 20, no. 8, pp. 1495–1500, 2016.

[129] J. Mirocha, B. Kosović, and G. Kirkil, "Resolved Turbulence Characteristics in Large-Eddy Simulations Nested within Mesoscale Simulations Using the Weather Research and Forecasting Model," *Monthly Weather Review*, vol. 142, no. 2, pp. 806–831, 2014.

[130] C. Talbot, E. Bou-Zeid, and J. Smith, "Nested Mesoscale Large-Eddy Simulations with WRF: Performance in Real Test Cases," *Journal of Hydrometeorology*, vol. 13, no. 5, pp. 1421–1441, 2012.

[131] Y. Liu, T. Warner, Y. Liu, C. Vincent, W. Wu, B. Mahoney, S. Swerdlin, K. Parks, and J. Boehnert, "Simultaneous nested modeling from the synoptic scale to the LES scale for wind energy applications," *Journal of Wind Engineering and Industrial Aerodynamics*, vol. 99, no. 4, pp. 308–319, 2011.

[132] D. Muñoz-Esparza and B. Kosović, "Generation of Inflow Turbulence in Large-Eddy Simulations of Nonneutral Atmospheric Boundary Layers with the Cell Perturbation Method," *Monthly Weather Review*, vol. 146, no. 6, pp. 1889–1909, 2018.

[133] D. Muñoz-Esparza, R. Sharman, J. Sauer, and B. Kosović, "Toward Low-Level Turbulence Forecasting at Eddy-Resolving Scales," *Geophysical Research Letters*, vol. 45, no. 16, pp. 8655–8664, 2018.

[134] C. Nie, H. Li, L. Yang, B. Ye, E. Dai, S. Wu, Y. Liu, and Y. Liao, "Spatial and temporal changes in extreme temperature and extreme precipitation in Guangxi," *Quaternary International*, vol. 263, pp. 162–171, 2012.

[135] P. Gong, J. Wang, L. Yu, Y. Zhao, Y. Zhao, L. Liang, Z. Niu, X. Huang, H. Fu, S. Liu, C. Li, X. Li, W. Fu, C. Liu, Y. Xu, X. Wang, Q. Cheng, L. Hu, W. Yao, H. Zhang, P. Zhu, Z. Zhao, H. Zhang, Y. Zheng, L. Ji, Y. Zhang, H. Chen, A. Yan, J. Guo, L. Yu, L. Wang, X. Liu, T. Shi, M. Zhu, Y. Chen, G. Yang, P. Tang, B. Xu, C. Giri, N. Clinton, Z. Zhu, J. Chen, and J. Chen, "Finer resolution observation and monitoring of global land cover: First mapping results with Landsat TM and ETM+ data," *International Journal of Remote Sensing*, vol. 34, no. 7, pp. 2607–2654, 2013.

[136] D. K. Lilly, "The Representation of Small-Scale Turbulence in Numerical Simulation Experiments." *Proceedings of the IBM Scientific Computing Symposium on Environmental Sciences*, no. November, pp. 195–210, 1966.

[137] S.-Y. Hong, Y. Noh, and J. Dudhia, "A New Vertical Diffusion Package with an Explicit Treatment of Entrainment Processes," *Monthly Weather Review*, vol. 134, no. 9, pp. 2318–2341, 2006.

[138] K. S. Hansen, R. J. Barthelmie, L. E. Jensen, and A. Sommer, "The impact of turbulence intensity and atmospheric stability on power deficits due to wind turbine wakes at Horns Rev wind farm," *Wind Energy*, vol. 20, no. 8, pp. 1495–1500, 2012.

[139] R. Baxter, N. Hastings, A. Law, and E. J. Glass, *The Courant–Friedrichs–Lewy (CFL) Condition*, 2008, vol. 39, no. 5.

[140] Agustín Santiago, "Atendió Protección Civil más de 20 reportes en el Istmo por fuertes vientos," Salina Cruz, Oaxaca, 2018.

[141] J. Hernández, "Motorista pierde la vida en accidente sobre carretera 190," Santiago Niltepec, Oaxaca, 2018.

[142] Rar, “Suspenden clases en escuelas del Istmo de Oaxaca por fuertes vientos,” Oaxaca, 2018.

[143] Óscar Rodríguez, “Viento provoca voladura de camión en Oaxaca,” La Ventosa, 2018.

[144] P. A. Jiménez, J. Dudhia, J. F. González-Rouco, J. Navarro, J. P. Montávez, and E. García-Bustamante, “A Revised Scheme for the WRF Surface Layer Formulation,” *Monthly Weather Review*, vol. 140, no. 3, pp. 898–918, 2012.

[145] M. Angel, G. Miguez, and F. Canoura, “W ind power forecasting for a real onshore wind farm on complex terrain using WRF high resolution simulations. .”

[146] Z. Yang, Y. Li, and J. E. Seem, “Optimizing Energy Capture of Cascaded Wind Turbine Array With Nested-Loop Extremum Seeking Control,” *Journal of Dynamic Systems, Measurement, and Control*, vol. 137, no. 12, p. 121010, 2015.

[147] A. Ecot and R. Boronat, “ecotècnia 74 , 80 1.67 & 80 2.0,” ALSTOM, Tech. Rep., 2008.

[148] R. Baxter, N. Hastings, A. Law, and E. J. Glass, “Prospectiva de Energías Renovables 2017-2031,” Tech. Rep. 5, 2017.

[149] P. J. Coldwell, A. Ricardo, F. Quiroga, and F. Z. Reyes, “Reporte de Avance de Energias Limpias 2017,” Tech. Rep., 2017.

[150] B. V. G. Associates, “The Power of Onshore Wind,” Tech. Rep. June, 2018.

[151] R. B. Smith, “On Severe Downslope Winds,” *Americal Meteorological Society*, 1985.

[152] A. Estévez, C. Muñoz-Pina, and R. Morales, “Wind Farms in Oaxaca, Mexico: Complex Contracting and Spatial Effects,” *Fourth Annual Conference on Transforming Development Through Inclusive Green Growth*, no. September, pp. 6–7, 2016.

[153] D. Wood, S. LOZANO, and O. Romero-Hernandez, “Wind energy potential in Mexico’s Northern Border States,” *Comprehensive Renewable Energy*, vol. 2, no. May, pp. 73–92, 2012.

[154] Q. Hernández-Escobedo, F. Manzano-Agugliaro, and A. Zapata-Sierra, “The wind power of Mexico,” *Renewable and Sustainable Energy Reviews*, vol. 14, no. 9, pp. 2830–2840, 2010.

[155] D. R. Durran, “Another look at downslope windstorms. Part I: The development of analogs to supercritical flow in an infinitely deep, continuously stratified fluid,” *Journal of the Atmospheric Sciences*, vol. 43, no. 21, pp. 2527–2543, 1986.

[156] P. F. Sheridan and S. B. Vosper, “A flow regime diagram for forecasting lee waves, rotors and downslope winds,” *Meteorological Applications*, vol. 13, no. 2, pp. 179–195, 2006.

[157] R. F. Hertenstein and J. P. Kuettner, “Rotor types associated with steep lee topography: Influence of the wind profile,” *Tellus, Series A: Dynamic Meteorology and Oceanography*, vol. 57, no. 2, pp. 117–135, 2005.

[158] R. B. Smith, "Low Froude Number Flow Past Three-Dimensional Obstacles. Part I: Baroclinically Generated Lee Vortices," *Journal of the Atmospheric Sciences*, vol. 46, no. 8, pp. 3611–3613, 1989.

[159] V. Grubišić, S. Serafin, L. Strauss, S. J. Haimov, J. R. French, and L. D. Oolman, "Wave-induced boundary-layer separation in the lee of the Medicine Bow Mountains. Part II: Numerical modeling," *Journal of the Atmospheric Sciences*, p. 150904104933002, 2015.

[160] A. K. Pokharel, M. L. Kaplan, and S. Fiedler, "Subtropical Dust Storms and Downslope Wind Events," *Journal of Geophysical Research: Atmospheres*, vol. 122, no. 19, pp. 10 191–10 205, 2017.

[161] H. Ágústsson and H. Ólafsson, "Simulations of Observed Lee Waves and Rotor Turbulence," *Monthly Weather Review*, vol. 142, no. 2, pp. 832–849, 2014.

[162] K. Jung-Hoon and I.-U. Chung, "Study on Mechanisms and Orographic Effect for the Springtime Downslope Windstorm over the Yeongdong Region Jung-Hoon," *Atmosphere*, vol. 16, no. 2, pp. 67–83, 2006.

[163] M. T. Prtenjak and D. Belusic, "Formation of reversed lee flow over the north-eastern Adriatic during bora," *Geofizika*, vol. 26, no. 2, pp. 145–155, 2009.

[164] M. D. Priestley, J. G. Pinto, H. F. Dacre, and L. C. Shaffrey, "The role of cyclone clustering during the stormy winter of 2013/2014," *Weather*, vol. 72, no. 7, pp. 187–192, 2017.

[165] Y. Cao and R. G. Fovell, "Downslope Windstorms of San Diego County. Part I: A Case Study," *Monthly Weather Review*, vol. 144, no. 2, pp. 529–552, 2016.

[166] G. Ganbat, J. M. Seo, J. Y. Han, and J. J. Baik, "A theoretical study of the interactions of urban breeze circulation with mountain slope winds," *Theoretical and Applied Climatology*, vol. 121, no. 3-4, pp. 545–555, 2015.

[167] R. N. Hoffman and S. M. Leidner, "An Introduction to the Near–Real–Time QuikSCAT Data," *Weather and Forecasting*, vol. 20, no. 4, pp. 476–493, 2005.

[168] J. G. Powers, J. B. Klemp, W. C. Skamarock, C. A. Davis, J. Dudhia, D. O. Gill, J. L. Coen, D. J. Gochis, R. Ahmadov, S. E. Peckham, G. A. Grell, J. Michalakes, S. Trahan, S. G. Benjamin, C. R. Alexander, G. J. Dimego, W. Wang, C. S. Schwartz, G. S. Romine, Z. Liu, C. Snyder, F. Chen, M. J. Barlage, W. Yu, and M. G. Duda, "The weather research and forecasting model: Overview, system efforts, and future directions," *Bulletin of the American Meteorological Society*, vol. 98, no. 8, pp. 1717–1737, 2017.

[169] P. Markowski and Y. Richardson, *Mesoscale meteorology in midlatitudes*, 2010, vol. 137.

[170] S. Bontemps, P. Defourny, J. Radoux, E. Van Bogaert, C. Lamarche, F. Achard, P. Mayaux, M. Boettcher, C. Brockmann, G. Kirches, M. Zülkhe, V. Kalogirou, F. Seifert, and O. Arino, "Consistent global land cover maps for climate modelling communities: current achievements of the ESA' and cover CCI," *ESA Living Planet Symposium 2013*, vol. 2013, no. December, pp. 9–13, 2013.

[171] H. H. Shin and S.-Y. Hong, "Representation of the Subgrid-Scale Turbulent Transport in Convective Boundary Layers at Gray-Zone Resolutions," *Monthly Weather Review*, vol. 143, no. 1, pp. 250–271, 2015.

[172] C. Zhang, Y. Wang, and K. Hamilton, "Improved Representation of Boundary Layer Clouds over the Southeast Pacific in ARW-WRF Using a Modified Tiedtke Cumulus Parameterization Scheme *," *Monthly Weather Review*, vol. 139, no. 11, pp. 3489–3513, 2011.

[173] M. J. Iacono, J. S. Delamere, E. J. Mlawer, M. W. Shephard, S. A. Clough, and W. D. Collins, "Radiative forcing by long-lived greenhouse gases: Calculations with the AER radiative transfer models," *Journal of Geophysical Research Atmospheres*, vol. 113, no. 13, pp. 2–9, 2008.

[174] M. Tewari, F. Chen, W. Wang, J. Dudhia, M. A. LeMone, K. Mitchell, M. Ek, G. Gayno, J. Wegiel, and R. H. Cuenca, "IMPLEMENTATION AND VERIFICATION OF THE UNIFIED NOAH LAND SURFACE MODEL IN THE WRF MODEL," *Bulletin of the American Meteorological Society*, pp. 2165–2170, 2004.

[175] T. L. Clark and W. R. Peltier, "Critical level reflection and the resonant growth of nonlinear mountain waves," pp. 3122–3134, 1984.

[176] L. Armi and G. J. Mayr, "The descending stratified flow and internal hydraulic jump in the lee of the Sierras," *Journal of Applied Meteorology and Climatology*, vol. 50, no. 10, pp. 1955–2011, 2011.

[177] J. Szmyd, "Influence of lee waves and rotors on the near-surface flow and pressure fields in the northern foreland of the Tatra Mountains," *Meteorological Applications*, vol. 23, no. 2, pp. 209–221, 2016.

[178] C. M. Appendini, J. Hernández-Lasheras, R. Meza-Padilla, and J. A. Kurczyn, "Effect of climate change on wind waves generated by anticyclonic cold front intrusions in the Gulf of Mexico," *Climate Dynamics*, vol. 0, no. 0, pp. 1–17, 2018.

[179] X. Hong, M. Peng, S. Wang, and Q. Wang, "Simulating and understanding the gap outflow and oceanic response over the Gulf of Tehuantepec during GOTEX," *Dynamics of Atmospheres and Oceans*, vol. 82, pp. 1–19, 2018.

[180] O. A. Jaramillo and M. A. Borja, "Wind speed analysis in La Ventosa, Mexico: A bimodal probability distribution case," *Renewable Energy*, vol. 29, no. 10, pp. 1613–1630, 2004.

[181] R. Romero-Centeno, J. Zavala-Hidalgo, A. Gallegos, and J. J. O'Brien, "Isthmus of tehuantepec wind climatology and ENSO signal," *Journal of Climate*, vol. 16, no. 15, pp. 2628–2639, 2003.

[182] M. J. Brennan, H. D. Cobb, and R. D. Knabb, "Observations of Gulf of Tehuantepec Gap Wind Events from QuikSCAT: An Updated Event Climatology and Operational Model Evaluation," *Weather and Forecasting*, vol. 25, no. 2, pp. 646–658, 2010.

[183] J. P. McCreary, H. S. Lee, and D. B. Enfield, "The response of the coastal ocean to strong offshore winds: With application to circulations in the Gulfs of Tehuantepec and Papagayo," *Journal of Marine Research*, vol. 47, no. 1, pp. 81–109, 1989.

[184] D. R. Durran, "Lee Waves and Mountain Waves," *Encyclopedia of Atmospheric Sciences*, pp. 1161–1169, 2013.

[185] W. J. Steenburgh, D. M. Schultz, and B. A. Colle, "The Structure and Evolution of Gap Outflow over the Gulf of Tehuantepec, Mexico," *Monthly Weather Review*, vol. 126, no. 10, pp. 2673–2691, 1998.

[186] R. S. Arthur, J. D. Mirocha, K. A. Lundquist, and R. L. Street, "Using a canopy model framework to improve large-eddy simulations of the neutral atmospheric boundary layer in the Weather Research and Forecasting model," *Monthly Weather Review*, pp. MWR–D–18–0204.1, 2018.

[187] P. Doubrawa, A. Montornes, R. J. Barthelmie, S. C. Pryor, G. Giroux, and P. Casso, "Effect of Wind Turbine Wakes on the Performance of a Real Case WRF-LES Simulation," *Journal of Physics: Conference Series*, vol. 854, no. 1, 2017.

[188] C. Xu, J. Yang, C. Li, W. Shen, Y. Zheng, and D. Liu, "A Research on Wind Farm Micro-sitting Optimization in Complex Terrain," *International Conference on aerodynamics of Offshore Wind Energy Systems and wakes*, pp. 669–679, 2013.

[189] A. C. Fitch, J. B. Olson, J. K. Lundquist, J. Dudhia, A. K. Gupta, J. Michalakes, and I. Barstad, "Local and Mesoscale Impacts of Wind Farms as Parameterized in a Mesoscale NWP Model," *Monthly Weather Review*, vol. 140, no. 9, pp. 3017–3038, 2012.

[190] A. H. Schrotenboer, M. A. uit het Broek, B. Jargalsaikhan, and K. J. Roodbergen, "Coordinating technician allocation and maintenance routing for offshore wind farms," *Computers and Operations Research*, vol. 98, pp. 185–197, 2018.

[191] GWEC, "GWEC Global Wind 2017 report: Offshore Wind," 2018.

[192] A. Montornès, "WRF LES, the microscale awakens," Boulder, Colorado, pp. 1323–1330, 2002.

[193] H. Xu, Y. Wang, and M. Wang, "The Performance of a Scale-Aware Nonlocal PBL Scheme for the Subkilometer Simulation of a Deep CBL over the Taklimakan Desert," *Advances in Meteorology*, vol. 2018, 2018.

[194] A. Montornès, P. Casso, B. Kosovic, and G. Lizcano, "WRF-LES in the real world: Towards a seamless modeling chain for wind industry applications," *17th Annual WRF Users' Workshop*, 2016.

[195] Wind Europe, "Wind in power 2017. Annual combined onshore and offshore wind energy statistics," Wind Europe, Tech. Rep., 2018.

[196] D. Muñoz-Esparza, B. Kosović, C. García-Sánchez, and J. van Beeck, "Nesting Turbulence in an Offshore Convective Boundary Layer Using Large-Eddy Simulations," *Boundary-Layer Meteorology*, vol. 151, no. 3, pp. 453–478, 2014.

[197] D. W. Keith, J. F. Decarolis, D. C. Denkenberger, D. H. Lenschow, S. L. Malyshev, S. Pacala, and P. J. Rasch, "The influence of large-scale wind power on global climate." *Proceedings of the National Academy of Sciences of the United States of America*, vol. 101, no. 46, pp. 16 115–16 120, 2004.

[198] Eea, *Europe's onshore and offshore wind energy potential*, 2009, vol. 6, no. 6.

[199] American Wind Energy Association, "U.S. Wind Industry 2016 Annual Market Update," p. 2, 2016.

[200] J. A. Slater, B. Heady, G. Kroenung, W. Curtis, J. Haase, D. Hoegemann, C. Shockley, and K. Tracy, "Evaluation of the New ASTER Global Digital Elevation Model," vol. 77, no. 4, pp. 335–349, 2009.

[201] Ewea, "Wind in power - 2015 European statistics," *2015 European statistics.*, vol. 2016, no. February 13, p. The European Wind Energy Association, 2016.

[202] Q. Wang, H. Wu, A. R. Florita, C. Brancucci Martinez-Anido, and B. M. Hodge, "The value of improved wind power forecasting: Grid flexibility quantification, ramp capability analysis, and impacts of electricity market operation timescales," *Applied Energy*, vol. 184, pp. 696–713, 2016.

[203] M. Bilal, K. Solbakken, and Y. Birkelund, "Wind speed and direction predictions by WRF and WindSim coupling over Nygårdsfjell," *Journal of Physics: Conference Series*, vol. 753, no. 8, 2016.

[204] N. Troldborg and J. Sørensen, "A simple atmospheric boundary layer model applied to large eddy simulations of wind turbine wakes," *Wind Energy*, vol. 17, no. April 2013, pp. 657–669, 2014.

Derived publications

- M.A. Prósper, C. Otero-Casal, F. Canoura and G. Miguez-Macho (2018), *‘Wind power forecasting for a real onshore wind farm on complex terrain using WRF high-resolution simulations’*. Renewable Energy.

- M.A. Prósper, I. Sosa, C. Otero-Casal and G. Miguez-Macho (2018), *‘Extreme wind event study in a wind farm area on the Isthmus of Tehuantepec using WRF high-resolution simulations’*. *Under review.

- C. Otero-Casal, P. Patlakas, M.A. Prósper, G. Galanis, and G. Miguez-Macho (2018), *‘Development of a high-resolution wind forecast system based on the WRF model and a hybrid Kalman-Bayesian filter’*. *Under review.

International congress contributions

- Workshop: WRF/MPAS Users’ Workshop, Boulder, Colorado (US), 06-2018. *’Downslope wind storm study in a wind farm area on the Isthmus of Tehuantepec using WRF high-resolution simulations.’*

- Congress: European Geosciences Union General Assembly (EGU), Vienna (Austria), 04-2018. (1) *’Mean Annual Wake study for a wind farm in the province of Jiangsu (China)’* & (2)*’Extreme wind event study in a wind farm area on the Isthmus of Tehuantepec using WRF high- resolution simulations’*.

- Workshop: WRF Users’ Workshop, Boulder, Colorado (US), 06-2017. *’Stability analysis for different wind farm locations using WRF high resolution simulations’*.

- Congress: European Geosciences Union General Assembly (EGU), Vienna (Austria), 04-2017. *’Wind power forecasting for a real onshore wind farm on complex terrain using WRF high resolution simulations’*.

USC
UNIVERSIDADE
DE SANTIAGO
DE COMPOSTELA

Versión extendida resumen

El desarrollo de la energía eólica tiene un efecto directo en la reducción de las emisiones de dióxido de carbono procedentes del sector energético. Dicha industria es uno de los mayores contribuyentes antropogénicos al problema mundial del cambio climático. Por ello, y por ser la energía renovable más expandida a nivel global, existe una clara necesidad de optimizar la explotación eólica. La modelización numérica es una herramienta que forma parte del presente y del futuro de este sector, porque es capaz de reproducir el efecto de los parques eólicos en la atmósfera y de obtener su predicción de producción a corto plazo. Además de esto, los modelos meteorológicos nos permiten mejorar los métodos de análisis de recurso eólico cualquier región del planeta. La presente tesis busca lograr una detallada cuantificación y entendimiento de las principales interacciones entre la capa límite de la atmósfera y la topografía, centrándose en el comportamiento de los flujos de viento a diferentes escalas. A mayores de esto, se pretende mejorar los instrumentos, dentro de la modelización numérica, encargados de analizar dichos mecanismos, contribuyendo de esta forma a la optimización del aprovechamiento del recurso eólico. La principal herramienta empleada en esta tesis es el modelo WRF (Weather Reseach and Forecasting). Se trata de un sistema de predicción numérica a meso y microescala diseñado tanto para la investigación atmosférica como para predicción operativa. En la mayoría de las partes de la investigación se realizarán simulaciones a alta resolución con dicho modelo. De este modo se obtendrá información precisa sobre campos de viento cercanos a la superficie y procesos turbulentos en una amplia gama de condiciones de estabilidad atmosférica y zonas del planeta, tanto en regiones llanas como en terreno complejo.

Europa, con 168,7 GW de potencia eólica total instalada a finales de 2017, ha cubierto el 10,4% de sus necesidades de consumo eléctrico con energía eólica. En España, la energía eólica representa una de las principales fuentes de energía. A pesar del estancamiento en el desarrollo de parques eólicos desde 2014, España sigue siendo el quinto país en potencia eólica instalada, sólo por detrás de China, EE.UU., Alemania e India. en este momento hay 23075 MW de potencia eólica instalada en 1077 parques, que cubren la demanda eléctrica de unos 10 millones de hogares. La mayoría de los clusters de parques eólicos del país están situados en el norte de Galicia y Castilla y León. Existe una clara necesidad de mejorar la explotación del recurso eólico, dado que la cantidad de energía eólica producida está aumentando rápidamente debe ser incorporada eficientemente a la red eléctrica para su distribución. Para ello, es esencial tener un conocimiento claro del flujo de aire que alimenta los parques, entendiendo su comportamiento en capas cercanas a la superficie, y siendo capaces de realizar pronósticos locales precisos a corto plazo con el fin de optimizar la construcción y explotación de parques eólicos. La previsión de la energía eólica a corto plazo presenta muchos retos. En la mayoría de los casos, los parques onshore se ven afectados por eventos a microescala que son especialmente complicados de predecir porque tienen una fenomenología turbulenta, generando variaciones en la dirección de viento y cambios de intensidad en cortos períodos de tiempo. En los últimos años, debido al crecimiento global de la energía eólica y al aumento exponencial de la capacidad de computo, ha habido un desarrollo importante en los métodos de pronóstico de energía eólica y eólica a corto plazo.

La modelización numérica, además de reproducir el efecto de parques en la atmósfera, permite mejorar los métodos de análisis de recurso eólico de un región determinada. Los modelos a mesoescala como el WRF (Weather Research and Forecasting) son capaces de realizar simulaciones con una resolución horizontal de menos de cien metros, Large Eddy Simulations (LES) con el objetivo de predecir y caracterizar los fenómenos turbulentos extremos que afectan a los parques eólicos y tienen un impacto directo en la producción de energía. Este tipo de herramientas de predicción numérica también se pueden combinar con modelos de post-procesado estadísticos. En este tipo de estudios normalmente se utilizan simulaciones de menor resolución en el que desarrollan un sistema de pronóstico de viento que combinan simulaciones WRF con herramientas estadísticas como los filtros Kalman. Con respecto a las herramientas específicas de parques para predicciones de modelos numéricos, las versiones de WRF 3.3 y posteriores incluyen una parametrización del parque eólico capaz de simular los efectos de estela de un aerogenerador en el entorno cercano y calcular su producción según la curva de potencia, coeficientes estándar y dimensiones de la máquina.

De todos modos, es difícil encontrar estudios que utilicen estas herramientas específicamente para los parques eólicos y comparen directamente los resultados con las observaciones. Debido a la dificultad de obtener datos de observaciones, la mayoría de las investigaciones en este campo examinan el impacto hipotético de las diferentes configuraciones de las explotaciones a varias escalas. También se ha utilizado en estudios relacionados con el impacto que los parques eólicos tienen en el clima mundial. por otro lado, también existen varias publicaciones que utilizan el WRF para el parques offshore. Entre otras, se realizan simulaciones de alta resolución (333 m) para estimar el déficit total de energía en un área debido a los efectos de la estela de las turbinas del parque.

Los principales objetivos en esta investigación están centrados en el estudio de las interacciones entre las capas más bajas de la atmósfera con la superficie y con los parques eólicos. También se pretenden desarrollar diferentes herramientas de predicción a diversas escalas temporales y espaciales mediante el WRF a alta resolución. Parte de estos estudios y desarrollos se realizarán a partir de datos del parque eólico de Coruxeiras, en el que, entre otras cosas, se pondrá a funcionar una herramienta de predicción operativa de viento y energía eólica. Durante todo un año se comprobará la eficacia del modelo WRF en la tarea de predecir de la producción energética de este parque eólico en terreno complejo. La disponibilidad de datos reales in situ de alta calidad permite una validación detallada de las simulaciones, en términos de predicción de potencia y del impacto de las estelas en las otras turbinas. Además, también se pretende analizar las diferencias entre las simulaciones a alta resolución con simulaciones de baja resolución para diferentes escalas temporales. De esta forma se podrá evaluar el potencial del método y la configuración de alta resolución. Es la primera vez que se realiza una evaluación exhaustiva durante un período de tiempo tan largo y de forma tan detallada.

Como se ha introducido, la principal herramienta empleada es el modelo WRF. Se trata de un sistema de predicción numérica a meso y microescala diseñado tanto para la investigación atmosférica como para predicción operativa. Es un modelo regional en el cual las condiciones iniciales y de contorno se definidas con un modelo global. Para lograr una alta resolución, en general, se utiliza una configuración de dominios anidados en el que se establecen dominios ’hijo’ sucesivos con una resolución cada vez mayor dentro de dominios ’padre’ de menor resolución. El domino padre correspondiente proporciona las condiciones de contorno a la malla anidada a lo largo del tiempo de simulación. Con este procedimiento, es posible realizar simulaciones de alta resolución a partir de datos de modelos globales. El WRF incluye parametrizaciones para procesos atmosféricos que ocurren a escalas espaciales no resueltas por el modelo como la microfísica de las nubes, convección de cúmulos, capa límite planetaria y turbulencia superficial y radiación.

En algunas de las partes de la investigación se utilizan simulaciones WRF-LES. La calidad de los resultados obtenidos de las simulaciones WRF de alta resolución depende en gran medida de la interpretación de los resultados que el modelo hace de los remolinos a gran escala dentro de la capa de mezcla (PBL) y de cómo trata los procesos subgrid scale (SGS). Mediante múltiples dominios anidados es posible resolver la fenomenología a escala turbulenta e incluir el efecto mesoescala en el dominio de mayor resolución. Pare poder poner este concepto en la práctica, en muchos casos, es necesario alcanzar niveles muy altos de resolución (<100m) mediante LES. Este tipo de simulaciones pueden ser una herramienta precisa que proporciona información sobre procesos turbulentos en una amplia gama de condiciones de estabilidad atmosférica, tanto en regiones llanas como en terreno complejo. Para suministrar condiciones iniciales y de contorno a nuestras simulaciones se utilizarán pricipalmente las salidas de modelo de predicción global GFS del National Center for Environmental Prediction (NCEP). Es necesario disponer de los recursos de cálculo computacional adecuados para realizar simulaciones con este modelo numérico. Para ello se dispone de la infraestructura del CESGA (Centro Tecnológico de Supercomputación de Galicia). En sus servidores del cálculo se compila y ejecuta el WRF con diversas configuraciones y se almacenan los resultados obtenidos. Para post-procesar las salidas del modelo, analizar y visualizar resultados se utilizan diferentes lenguajes de programación como Python o Bash. A mayores de esto, también se emplean otras herramientas de software específicas en el campo de la modelización meteorológica como CDO (Climate Data Operators), NCL (Ncar Command Language) or GDAL (Geospatial Data Abstraction Library).

Motivación y resumen de capítulos

En esta tesis se pretende lograr una cuantificación y comprensión detallada de los principales interacciones entre la capa límite del planeta atmosférico y el terreno, centrándose en la comportamiento de los flujos de viento a diferentes escalas. De esta manera pretendemos mejorar las herramientas, en el marco de modelado numérico, para el análisis de dichos mecanismos, contribuyendo a la optimización del uso del recurso eólico. Para ello, utilizamos el WRF (Weather Research and Forecasting) como herramienta principal. En la mayor parte de la investigación, lo configuramos con alta resolución, llegando incluso a la microescala a través de LES (Large Eddy Simulations). De esta manera, pretendemos proporcionar información precisa de los campos eólicos y de los diferentes procesos turbulentos en un amplio rango de condiciones de estabilidad atmosférica y áreas del planeta, tanto en terrenos planos como complejos. En la primera parte de la tesis, compuesta por los dos primeros capítulos, presentamos un amplio estudio sobre la previsión del recurso eólico para un parque eólico onshore. El primer capítulo se centra en el caso de la previsión y validación de la producción eólica para un parque eólico real onshore utilizando simulaciones de modelos WRF de alta resolución horizontal y vertical. El parque eólico está situado en Galicia, en el noroeste de España, en una región de terreno complejo y con alto recurso eólico. Utilizando el esquema

Fitch, específico para parques eólicos, se simula un período de un año con una configuración de previsión diaria de funcionamiento. En el segundo capítulo, damos un paso adelante en el campo de la previsión a corto plazo combinando la predicción del del primer estudio con una herramienta estadística de post-proceso (filtro Kalman-Bayesian). Con esta técnica, llegamos a la escala temporal de nowcasting, con interesantes aplicaciones en la industria eólica.

La segunda parte, presentada en el capítulo tres, se centra en el efecto estela de los parques eólicos en su entorno. Introducimos el concepto Annual Wake, que es el recurso eólico medio anual perdido en la zona debido a la estela del parque eólico. Probamos esta herramienta en el mismo parque eólico de la primera parte y en otro situado al este de China.

La tercera parte aborda la cuestión del estudio de los vientos extremos. En concreto, se centra en la investigación de los diferentes fenómenos de las mountain lee waves resultantes de la compleja interacción entre las condiciones meteorológicas a gran escala y los forzamientos orográficos locales en un grupo de parques eólicos en México. Finalmente, en la cuarta y última parte, en el capítulo cinco, se analiza la microescala turbulenta en un área de parque eólico en el sur de China usando simulaciones WRF-LES.

A continuación se presenta un resumen de cada uno de los capítulos de la tesis.

Capítulo 2: Predicción de recurso eólico

Los modelos meteorológicos regionales se están convirtiendo en una herramienta cada vez más usada para la predicción del recurso eólico debido a su capacidad para simular la dinámica de los flujos de viento locales que afectan a la producción de parques eólicos. Este estudio se centra en la predicción y validación de la producción de un parque eólico real sobre terreno complejo mediante simulaciones del modelo WRF (Weather Research and Forecasting) a alta resolución. El parque eólico se encuentra en Galicia, en el noroeste de España, en una región compleja y con gran recurso eólico. Utilizando la parametrización Fitch, específica para parques eólicos, se simula un período de un año a partir sistema de predicción operativo diario. Se obtienen predicciones de producción energética y viento, y se comparan con datos reales obtenidos en cada turbina proporcionados por la empresa que explota el parque. Los resultados muestran que el WRF realiza una buena predicciones energía eólica para este tipo de parques eólicos, debido a su precisa representación del comportamiento de la capa límite planetaria de la región y al buen desempeño del esquema Fitch en estas condiciones. El mejor error medio anual (MAE) obtenido es de 1,87 m/s para la velocidad del viento y 14,75% para la energía eólica. Comparando experimentos con y sin el esquema de Fitch, estimamos las pérdidas del recurso eólico en la zona debido el efecto estela de los aerogeneradores. La estela media anual o la huella ambiental de la instalación se extiende varios kilómetros en la dirección suroeste-noreste de los vientos dominantes, con pérdidas de recursos del 0,5% incluso a 17 km de las turbinas.

Capítulo 3: Predicción de viento a corto plazo (nowcasting)

Los modelos meteorológicos regionales a microescala se han convertido en una herramienta fundamental para la predicción de la producción de parques eólicos debido a su capacidad para resolver la dinámica de los flujos locales. La alta demanda de herramientas de predicción fiables en la industria energética es la motivación para el desarrollo de un sistema integrado que combina el modelo atmosférico WRF con una optimización obtenida por el conjunción de un filtro Kalman y un modelo Bayesiano. Este estudio se centra en el desarrollo y validación de este sistema combinado en un parque eólico en Galicia (NW España). Se simula un período de un año a una resolución horizontal de 333 m, configuración de la predicción operativa diaria. El filtro Kalman-Bayesiano es probado tanto directamente en la velocidad del viento como en sus componentes U-V (zonal y meridional) en períodos de nowcasting de entre 10 minutos a 6 horas. Los resultados son prometedores, los principales índices de error estadístico mejoran significativamente en un horizonte de previsión de 6 horas y aún más en los casos con un horizonte más corto. El error medio anual (MAE) para el horizonte de previsión 1h es de 1,03 m/s para la velocidad del viento y 12,16^{o} para la dirección del viento. Además, el éxito de la utilización del sistema integrado en los diferentes casos analizados demuestra la utilidad potencial que esta herramienta puede tener para una variedad de aplicaciones en parques eólicos operativos y el mercado energético.

Capítulo 4: Estela anual

El efecto estela local en las condiciones de flujo alrededor de los parques eólicos afecta significativamente la producción de energía eólica. En este capítulo se realizan simulaciones con el modelo WRF utilizando el esquema de Fitch para un parque eólico en la provincia china de Jiangsu, frente al mar Amarillo. Se simula un período de un año con una resolución horizontal de 333 m, obtiendo las predicciones de producción energética y viento y se comparan con los datos reales proporcionados por la empresa desarrolladora del parque. Los resultados muestran que el WRF realiza buenas predicciones de energía eólica para este tipo de parques, debido a una buena representación del comportamiento de la capa límite planetaria de la región y el buen desempeño del esquema Fitch bajo estas condiciones. Se observan efectos de estela significativos a varios kilómetros a favor del viento desde el parque, especialmente en las direcciones predominantes del viento (sureste-este). Estos resultados muestran que este método puede proporcionar información valiosa para el análisis de posibles ubicaciones futuras de parques eólicos.

Capítulo 5: Estudio de eventos extremos

Los Tehuantepecers o Tehuanos son vientos extremos producidos en el Istmo de Tehuantepec, que soplan hacia el sur a través del paso de Chivela, la brecha montañosa a través del Istmo, desde el Golfo de México hasta el Océano Pacífico. Son el resultado de la compleja interacción entre las condiciones meteorológicas a gran escala y las forzamientos orográficos locales alrededor del paso de Chivela y ocurren principalmente en los meses de invierno, debido a las advecciones de aire que se producen tras los frentes fríos que llegan hasta el sur. Pueden generar eventos extremos localizados, como downslope windstorms y saltos hidráulicos, fuertes flujos turbulentos que tienen un efecto directo en el lado Pacífico del istmo y en el Golfo de Tehuantepec. Este estudio se centra en la investigación de estos fenómenos mediante simulaciones de modelos WRF (Weather Research and Forecasting) de alta resolución horizontal y vertical. En particular, empleamos una configuración de cuatro dominios anidados, con resolución horizontal de hasta 444 m en el dominio más interior y 70 niveles verticales híbridos-sigma, 8 de los cuales son que se encuentran dentro de los primeros 200 m sobre el nivel del suelo. Seleccionamos un período de 36 horas en diciembre de 2013, que es cual se observaron condiciones favorables para la fenomenología local estudiada. El experimento de alta resolución del WRF revela una clara estructura compleja en el fuerte flujo de viento del Tehuano. Dependiendo del número de Froude en lo alto de la barrera topográfica, las condiciones de tormentas de viento (flujo supercrítico) o los saltos hidráulicos (flujo crítico) se desarrollan simultáneamente en diferentes lugares al este del paso de Chivela con diferentes alturas de terreno. La comparación con las observaciones sugiere que el modelo representa con precisión el intenso viento de bajada espacialmente heterogéneo y la formación de mountain wave clouds durante varias horas, con bajos errores en la velocidad y viento, dirección del viento, y temperatura.

Capítulo 6: Análisis de fenómenos a microescala

El estudio de los fenómenos de flujo de viento a microescala ha sido siempre un punto de interés dentro de la industria eólica. Hay varios eventos eólicos bien conocidos relacionados con él que los diseñadores de turbinas y los gerentes de operaciones deben tener en cuenta, tales como rachas de viento altas, los cambios extremos de dirección, ráfagas de viento coherentes con cambios de dirección o el cizallamiento extremo del viento. WRF Large Eddy Simulations (LES) es una herramienta de modelización numérica que se está utilizando cada vez más en este campo. Basado en una simulación WRF de muy alta resolución y una desactivación del esquema de capa límite planetaria, esta configuración WRF puede ser utilizada para simular flujos de viento turbulentos en numerosas aplicaciones en el sector eólico. En este estudio, evaluamos el las simulaciones LES en un terreno complejo en el área de un parque eólico en el sur de China. Para ello, simulamos un periodo de 10 días dividido en ejecuciones diarias utilizando una configuración de acoplamiento mesoescala-microescala que termina en dos dominios LES y alcanza una resolución horizontal de 98 m en el más interior. Para resolver la inestabilidad de las simulaciones, aplicamos una técnica de alisamiento zonal que suaviza la orografía cerca de puntos numéricamente inestables. Los resultados obtenidos se validan utilizando datos observacionales de tres estaciones meteorológicas en diferentes puntos de la zona.